UNIVERSITY OF OKLAHOMA

GRADUATE COLLEGE

RETRIEVAL OF MOISTURE FROM GPS SLANT-PATH WATER VAPOR

OBSERVATIONS USING 3DVAR AND ITS IMPACT ON THE PREDICTION

OF CONVECTION INITIATION AND PRECIPITATION

A DISSERTATION

SUBMITTED TO THE GRADUATE FACULTY

in partial fulfillment of the requirement for the

degree of

Doctor of Philosophy

By

HAIXIA LIU
Norman, Oklahoma
2007

RETRIEVAL OF MOISTURE FROM GPS SLANT-PATH WATER VAPOR
OBSERVATIONS USING 3DVAR AND ITS IMPACT ON THE PREDICTION
OF CONVECTION INITIATION AND PRECIPITATION

A DISSERTATION APPROVED FOR THE
SCHOOL OF METEOROLOGY

BY

_____
Ming Xue, Committee Chair

_____
Frederick Carr

_____
Lance Leslie

_____
Keith Brewster

_____
Mark Yeary

ACKNOWLEDGEMENTS

supercomputer at OSCER at the University of Oklahoma. Some of the analyses were

performed on IBM supercomputers at NCEP. Most of the prediction experiments were

performed on the supercomputers at the Pittsburgh Supercomputing Center.

Table of Contents

List of Tables

List of Figures

Abstract

The accurate prediction of convection initiation and the subsequent precipitation in a cloud-resolving numerical model is highly dependent on the precise estimate of the three-dimensional moisture in the initial condition because water vapor is directly involved in the formation of clouds and precipitation. However, the water vapor is currently poorly characterized due to its high variability in space and time. A three-dimensional variational analysis system (3DVAR) is developed in this dissertation to retrieve the moisture field from simulated ground-based GPS slant-path integrated water vapor (*SWV*) data that are potentially available at high temporal and spatial resolutions.

The 3DVAR system developed in this study is based on a terrain-following coordinate. A non-negative water vapor weak constraint is included in the cost function. The background term and its associated background error covariance are considered in the system and the latter is modeled using explicit or implicit recursive spatial filters. Most importantly, a direct way to estimate a flow-dependent background error covariance based on the idea of Riishøjgaard is proposed for the moisture analysis. The explicit spatial filter first is implemented with both isotropic and anisotropic options. It is demonstrated that this system is robust on deriving mesoscale moisture structures from the GPS *SWV* and surface observations and the analysis is improved when the anisotropic background error covariance is used. Sensitivity experiments show that surface moisture data are important for the analysis near ground and a vertical filter is essential to obtain an accurate analysis near the surface. The positive impact of flow-dependent background error is enhanced when the density of GPS receiver network is lower.

The anisotropic explicit filter is computationally expensive in both CPU time and memory usage. Therefore the implicit recursive filter which is computationally much more efficient is implemented in our 3DVAR system, even though its implementation is significantly more complicated. A similar set of water vapor analysis experiments using the recursive filters is performed. The analyses thus obtained are generally comparable to or better than those obtained using the corresponding explicit filters. In addition, the sensitivity of the analyses to the spatial de-correlation scales of the background error is systematically examined.

A set of high-resolution numerical experiments is conducted using the Advanced Regional Prediction System (ARPS) for a case that occurred on 12 June, 2002 and involved multiple initiations of convection. The results are verified against the radar composite reflectivity in detail. It is shown that the model performs reasonably well on predicting the initiation timing and location and the subsequent storm evolution for up to 7 hours. Using the most realistic simulation of this case as the 'truth', simulated *SWV* data and surface moisture observations are generated to perform a set of Observing System Simulation Experiments (OSSEs) using our 3DVAR system with recursive filters. The preliminary results illustrate that convection initiation (CI) without strong low-level mesoscale forcing is highly sensitive to the moisture initial condition and the use of *SWV* and surface data improves the moisture analysis and thus the prediction of CI and precipitation. The enahnced moisture analysis obtained from the use of anisotropic background error further improves the precipitation forecast though it does not lead to positive impact on the prediction of exact timing and location of the CI due to its high sensitivity to very small-scale moisture structures.

Chapter 1
Introduction and Overview

1.1 Background and motivation

Water vapor is important for severe weather forecasting because moisture is directly related to the formation of clouds and precipitation. The latent heat of evaporation released when vapor condenses to form clouds influences the dynamics of the atmosphere. The condensation process modifies the effective static stability of the atmosphere and leads to precipitation formation. The prediction of convective precipitation is strongly dependent on the vertical distribution of buoyancy within clouds while the buoyancy profile is closely related to the amount of water vapor within the boundary layer. Moreover, predicting the convection initiation (CI) in cloud-resolving models can be highly dependent on very precise estimates of water vapor within and just above the boundary layer (Crook 1996). The water vapor mixing ratio can vary by several g kg^{-1} within the boundary layer due to boundary layer features such as the horizontal convective rolls (HCRs). A detailed knowledge on moisture within the boundary layer is valuable for the validation and understanding of the processes that occur within or related the boundary layer.

However, water vapor is one of the least understood and poorly characterized components of the atmosphere. The vertical water vapor distribution is poorly correlated with surface humidity measurements because surface measurements are strongly related to land-air interactions and do not accurately represent the entire

boundary layer. It is well known that water vapor has significant small-scale variations over time and space. Most of the past moisture observation instruments could not provide enough information for studying moisture variability, especially at the convective scale. Thus, an insufficient amount of work has been done to study small temporal or spatial scale variations of moisture in the atmosphere. In 2002, the International H_2O Project (IHOP_2002) was conducted and one of its goals was to improve our knowledge of the storm-scale moisture distribution. For example, Fabry (2006) analyzed refractivity data collected by radar and aircraft-based measurements during IHOP_2002 to statistically estimate the moisture variability in the boundary layer.

Knowledge of realistic spatial and temporal variations of water vapor can help improve severe storm forecasting. Park and Droegemeier (1999; 2000) demonstrate that moisture perturbations inserted in a modeled storm exert the largest influence on storm features such as vertical velocity and surface rainfall, and the accumulated rainfall showed the largest sensitivity to environmental moisture perturbations. Significant improvements in forecast skill for convective events can be obtained when horizontal variations and realistic mesoscale details in the water vapor mixing ratio are included together with available surface moisture (Koch et al. 1997; Parsons et al. 2000; Weckwerth 2000). The lack of precise and continuous water vapor data is one of the major error sources in short-term precipitation forecasting (Kuo et al. 1993; Kuo et al. 1996). Improved monitoring of water vapor and its assimilation into NWP models can lead to more accurate prediction of severe weather and precipitation.

Therefore, it is highly desirable to develop and deploy observing systems to measure atmospheric moisture and to effectively analyze such data to obtain its three dimensional structure and amount. Despite recent advances in remote sensing of wind and temperature, there remains a great need for cost-effective profiling of water vapor. Radiosondes provide rather accurate in-situ water vapor measurements but are too expensive to operate at high temporal and spatial resolutions. Water vapor radiometers measure water vapor with temporal resolution of about 10 min, but their cost prohibits the deployment of dense networks. Satellite-borne instruments have great potential to measure at high temporal and horizontal spatial resolutions, but current systems cannot provide accurate measurements at high enough vertical resolutions in the lower troposphere and the measurements can often be limited by extensive clouds.

The Global Positioning System (GPS) satellites provide a state-of-art technique that can estimate the atmospheric moisture at high temporal and spatial resolutions (Bevis et al. 1992). A radio signal, transmitted from a GPS satellite to a ground-based receiver or a space-based receiver installed on a low earth orbit satellite, is delayed when it goes through the atmosphere. A significant part of the delay is caused by the water vapor. Thus, the atmospheric moisture can be derived from the GPS delay observations. Precipitable water vapor (or *PW*, which is defined as the total integrated water vapor in a vertical column) estimates with millimeter accuracy can be achieved which can be superior to those from water vapor radiometers (Rocken et al. 1995; Duan et al. 1996). Braun et al. (2001) estimate that the accuracy of the integrated water vapor along the slant path between a GPS satellite and a ground-based receiver (called slant-path water vapor, *SWV*) is a few millimeters. One advantage of *SWV* measurement is

that *SWV* data, when existing in many paths, contain information on the spatial distribution of water vapor near a GPS ground-based receiver while *PW* contains the information only directly above the receiver station. In fact, *PW* data are derived from *SWV* data by assuming certain spatial and temporal homogeneity.

It is the motivation of this study to analyze 3D water vapor distribution from GPS *SWV* observations using the three-dimensional variational (3DVAR) method. The 3DVAR is a data assimilation method widely used at operational NWP centers because of its ability in dealing with indirect observations (Kalnay 2002) such as satellite and radar observations. Compared to four-dimensional variational (4DVAR) and ensemble Kalman filter (EnKF) schemes, 3DVAR is much more computationally efficient. A 3DVAR-based method is currently used operationally to initialize both global and regional prediction models at the U.S. National Center for Environment Prediction (NCEP) (Parrish et al. 1997; Wu et al. 2002). More recently, the 3DVAR method has been applied to the convective scale for the assimilation of Doppler radar data (e.g., Gao et al. 2004; Hu et al. 2006).

One of the goals of this study is to develop a specific 3DVAR procedure for retrieving/analyzing three-dimensional water vapor field from the GPS *SWV* observations, which are by themselves integrated quantities along the slant paths. In an effort to improve the quality of analysis using the 3DVAR method, flow-dependent background error structures are estimated and incorporated into our 3DVAR formulation. A reliable estimate of the degree and orientation of anisotropy in the moisture background error is likely to be more important for moisture analysis and quantitative precipitation forecasts (QPF) because of the high spatial variability in

moisture compared to other state variables. The 3DVAR scheme developed will first be tested using simulated *SWV* data and the analyzed water vapor field is compared against the 'truth' fields so as to evaluate the performance of our 3DVAR system as well as the impact of using flow-dependent background error. The analysis scheme is then used to produce analyses that serve as the moisture initial condition for a dryline convection initiation case. Again, rather successful simulation of a real case is obtained first which is used at the truth for observing system simulation experiments (OSSEs). The impact of the GPS *SWV* data on the convection initiation forecast is carefully examined.

1.2 Outline of dissertation

In Chapter 2, the standard 3DVAR analysis system is introduced. Some basic concepts and definitions are explained. Much attention is given to the estimation of background error covariance because it is one of the foci of this dissertation. The background error covariance controls the extent to which the observation information is spread in space. Since the dimensionality of the background error covariance matrix is extremely large for realistic atmospheric problems, we employ spatial filters to model its effect in the variational assimilation algorithm in order to save memory requirements. Our first implementation uses an explicit filter that is simple to implement but relatively computationally expensive. A computationally more efficient alternative is the implicit recursive filter which we implement after the positive impact of anisotropic background error is verified using the explicit filter. The implementation of a recursive filter in a 3DVAR system is discussed subsequently. In the second part of Chapter 2, the Global

Positioning System (GPS) as pertaining to the moisture observation is briefly described, together with its observations in various forms.

Based on the general 3DVAR framework introduced in Chapter 2, we propose in Chapter 3 a 3DVAR procedure specifically designed for retrieving 3D water vapor distribution from slant path water vapor data from a hypothetical ground-based GPS receiver network. This 3DVAR system is formulated in the Advanced Regional Prediction System (ARPS, Xue et al. 2000; Xue et al. 2003) terrain-following coordinates and the version described in Chapter 3 uses an explicit filter to model the background error covariance. A weak constraint of non-negative water vapor is included in the cost function to control the creation of negative water vapor near the tropospheric top in the analysis. A direct way to estimate flow-dependent background error structure based on the idea of Riishøjgaard (1998) is proposed. We examine the ability of this 3DVAR system in retrieving 3D water vapor distribution and the impact of flow-dependent background error covariance on the meso- and small-scale moisture structures which are important for severe weather prediction. Sensitivity experiments are performed to test several factors that affect the quality of analysis, including the influence of surface moisture observations and the vertical spatial filter on the analysis. Typical observation errors are also added to the *SWV* and regular surface observations to demonstrate the robustness of this 3DVAR analysis method in the presence of typical data errors. The effect of the density of ground-based GPS receiver stations on the analysis quality is also examined.

In Chapter 4, the computational efficiency of our 3DVAR system is improved through the use of implicit recursive filters in place of the explicit filters. The

background error covariance is estimated the same way as in Chapter 3. Compared to the explicit filter, the implementation of a recursive filter is much more complicated. The details on the implementation are provided. Two single observation tests are first conducted to verify the correctness of the implementation and illustrate the effects of isotropic and anisotropic recursive filters. A full set of water vapor retrieval experiments similar to those presented in Chapter 3 is then conducted and the results are compared to those obtained in Chapter 3 using explicit filters.

The second goal of this research is to investigate how the analyzed 3D water vapor field from GPS *SWV* data influences the prediction of convection initiation (CI) and the subsequent precipitation forecasts. We accomplish this based on observation system simulation experiments (OSSEs) for a squall line case from the IHOP_2002 field experiment. This case occurred on 12 June, 2002 and involved multiple initiations of convection on and near a dryline and a mesoscale convective system (MCS) outflow boundary. Boundary layer horizontal convective rolls also played important roles in the initiation of some of the convection. As a result, some of the storm initiation is highly sensitive to the fine scale structures of low level moisture. A set of high-resolution numerical experiments is conducted to obtain realistic simulations for this case. The simulation results are discussed in detail with emphasis on the timing and location of the initiation of various convective storms and subsequent evolution of precipitation. Several sensitivity experiments are also performed to better understand which factors are important to better forecast the convection initiation and precipitation involved in this case. These results are presented in Chapter 5.

A set of OSSEs is performed in Chapter 6, using the 3DVAR system with recursive filters developed in Chapter 4 and using the most realistic simulation obtained in Chapter 5 for the 12 June 2002 case as the 'truth'. These experiments examine the impact of simulated GPS SWV data on the prediction of CI and the subsequent precipitation in this case. Preliminary results demonstrate that the CI without strong surface forcing is very sensitive to the small-scale moisture structure in the low level atmosphere. The use of the SWV data in combination with surface moisture observations at the GPS receiver stations can noticeably improve the moisture analysis and consequently result in better prediction of CI and precipitation. The use of anisotropic background error covariance in the 3DVAR system further improves the moisture analysis at moderate scales, but does not lead to positive impact on the prediction of the exact timing and location of the CI that occurred in the absence of any significant mesoscale forcing. It is suggested that the very small-scale moisture structures on the scale of about 10 km has much influence on the exact timing and location of the CI in this case and such structures cannot be accurately analyzed solely using the 60 km receiver network resolution assumed in this study.

Chapter 7 provides an overall summary on the results of this dissertation and suggests some topics for future research.

Chapter 2
3DVAR Analysis System and GPS Measurements

In this chapter, the three-dimensional variational (3DVAR) formulation as a general data assimilation method is introduced. It is followed by a discussion on the estimation of background error covariance and on the use of explicit or recursive filters to model the covariance. The second part of this chapter describes the Global Positioning System (GPS) and its direct and derived observations for water vapor.

2.1 3DVAR formulations and use of spatial filters

2.1.1 Concept of 3DVAR

A 3DVAR analysis problem is defined as finding the optimal analysis vector $\mathbf{x}_a$ that minimizes a (scalar) cost function J which is defined as the distance between the analysis $\mathbf{x}$ (which is often the control variable that is adjusted for the cost function to be minimized) and the background vector $\mathbf{x}_b$ weighted by the inverse of the background error covariance $\mathbf{B}$, plus the distance between the analysis projected to the observation space and the observation vector $\mathbf{y}_o$ weighted by the inverse of the observation error covariance $\mathbf{R}$. The cost function J is defined according to the formula,

$$J(\mathbf{x}) = \frac{1}{2}(\mathbf{x} - \mathbf{x}_b)^{\mathrm{T}} \mathbf{B}^{-1}(\mathbf{x} - \mathbf{x}_b) + \frac{1}{2}(\mathbf{y}_o - H(\mathbf{x}))^{\mathrm{T}} \mathbf{R}^{-1}(\mathbf{y}_o - H(\mathbf{x})). \qquad (2.1)$$

The notations of Ide et al. (1997) are used throughout this dissertation. In this equation, H is the nonlinear observation operator that transforms the model variables $\mathbf{x}$ to the observation space. If the dimensions of the control vector $\mathbf{x}$ and the observation vector $\mathbf{y}_o$ are m and n respectively, then the operator H is an m by n matrix and can be linearized according to

$$H(\mathbf{x}) = H(\mathbf{x}_b + \delta\mathbf{x}) = H(\mathbf{x}_b) + \mathbf{H}\delta\mathbf{x}, \tag{2.2}$$

where $\mathbf{H}$, a m by n matrix, is the linearized tangent of H with elements $h_{i,j} = \partial H_i / \partial x_j$.

Substituting Eq. (2.2) into Eq. (2.1) gives,

$$J(\mathbf{x}) = \frac{1}{2}(\mathbf{x} - \mathbf{x}_b)^{\mathrm{T}} \mathbf{B}^{-1}(\mathbf{x} - \mathbf{x}_b) + \frac{1}{2}(\mathbf{y}_o - H(\mathbf{x}_b) - \mathbf{H}\delta\mathbf{x})^{\mathrm{T}} \mathbf{R}^{-1}(\mathbf{y}_o - H(\mathbf{x}_b) - \mathbf{H}\delta\mathbf{x}). \tag{2.3}$$

Define vector $\mathbf{d}$ as the observation innovation as follows,

$$\mathbf{d} = \mathbf{y}_o - H(\mathbf{x}_b), \tag{2.4}$$

we then obtain after substituting $\delta\mathbf{x} = \mathbf{x} - \mathbf{x}_b$ and Eq. (2.4) into Eq. (2.3),

$$J(\delta\mathbf{x}) = \frac{1}{2}\delta\mathbf{x}^{\mathrm{T}} \mathbf{B}^{-1}\delta\mathbf{x} + \frac{1}{2}(\mathbf{d} - \mathbf{H}\delta\mathbf{x})^{\mathrm{T}} \mathbf{R}^{-1}(\mathbf{d} - \mathbf{H}\delta\mathbf{x}). \tag{2.5}$$

This equation is called the incremental form cost function since it is in terms of the analysis increment, $\delta\mathbf{x}$. We take the derivative of Eq. (2.5) with respect to the new control variable $\delta\mathbf{x}$ and end up with

$$\nabla J(\delta\mathbf{x}) = (\mathbf{B}^{-1} + \mathbf{H}^{\mathrm{T}}\mathbf{R}^{-1}\mathbf{H})\delta\mathbf{x} - \mathbf{H}^{\mathrm{T}}\mathbf{R}^{-1}\mathbf{d}. \tag{2.6}$$

The optimal solution that minimizes the cost function is obtained by requiring that $\nabla J(\delta\mathbf{x}) = 0$. We therefore have,

$$\delta\mathbf{x} = (\mathbf{B}^{-1} + \mathbf{H}^{\mathrm{T}}\mathbf{R}^{-1}\mathbf{H})^{-1} \mathbf{H}^{\mathrm{T}}\mathbf{R}^{-1}\mathbf{d}. \tag{2.7}$$

Thus the optimal analysis is,

$$\mathbf{x}_a = \mathbf{x}_b + \left(\mathbf{B}^{-1} + \mathbf{H}^\mathrm{T}\mathbf{R}^{-1}\mathbf{H}\right)^{-1} \mathbf{H}^\mathrm{T}\mathbf{R}^{-1}\mathbf{d}\,. \qquad (2.8)$$

Equation (2.8) gives the analytical form of the optimal analysis. However, the solution in practice is not obtained by directly solving the above equation but by an iterative minimization algorithm such as the conjugate gradient or quasi-Newton method. With such a method, a first-guess (usually the analysis background) is chosen to start calculating the cost function according to Eq. (2.1) or Eq. (2.5) in incremental form. The gradient of the cost function is then computed with respect to control variable $\mathbf{x}$ in Eq. (2.1) or $\delta\mathbf{x}$ in Eq. (2.5) and the values of the gradient are passed into the optimization subroutine (e.g., in the conjugate gradient method), which determines the amount of adjustment needed to $\mathbf{x}$ so that the cost function is reduced. The equation for this adjustment is,

$$\mathbf{x}^{n+1} = \mathbf{x}^n + \alpha f\left(\nabla J\right)\,. \qquad (2.9)$$

In this equation, n is the number of iterations, α is the optimal step factor, and $f\left(\nabla J\right)$ is the optimal descent direction related to the gradient of the cost function. A subsequent step is to check if the norm of the gradient or the cost function itself satisfies a prescribed tolerance. If it does not, then the cost function is recalculated with the updated $\mathbf{x}^{n+1}$, and the above steps are repeated until convergence is reached. The solution obtained at convergence is the optimal analysis that minimizes the cost function.

2.1.2 Error covariance

An accurate specification of the background and observation error covariances is crucial to a successful optimal analysis. The diagonal elements in the covariance matrices, or the error variances of the background and observations, determine the relative weights given to the background and observations in the final analysis. Equally important is the spatial covariances of the background error because such error correlation controls the spatial spreading of observation information from the observation location to the analysis grid points that have error correlation with the observation locations and the pattern of the analysis increment is strongly influenced by the correlation structure. This will be demonstrated by the single observation experiments in Chapter 3 and 4. Meanwhile, the background error correlation plays a role of smoothing the analysis increment so that the analysis only contains the scales which are statistically compatible with the physical fields so as not to generate unphysical noise when the analysis is used to initialize a NWP model. In an analysis system that contains multiple analysis variables, there are usually cross-correlations among the analysis variables that reflect physical balance relations and such correlation information should also be included in the background error covariance matrix. For example, the large-scale atmosphere is usually hydrostatic and quasi-geostrophic. These balance properties allow the observations to be more effectively used. For example, the large scale wind observations can be used to update the geostrophic height field and vice versa.

The estimation of the background error covariance is the topic of many studies. The size of this covariance matrix for modern NWP models is huge, about 10^{14}

(Courtier 1997). Thus there is no way to practically determine or store this huge amount of information on current generation computers. Often a significant degree of approximation is involved in the estimation and use of this covariance matrix. There are five different approaches to estimating the background error covariances (Riishøjgaard 1998) that are in common use today.

The first one is the observational method (Hollingsworth and Lonnberg 1986) which is illustrated in Fig. 8 in Meteorological Training Course Lecture Series (Bouttier and Courtier 1999). This method relies on the use of background departures in an observing network that is dense and large enough to provide information on many scales and all the observations must be assumed to be uncorrelated and discrete. It is also assumed that there is no correlation between observations and background errors. The detailed principle of this method is described by Bouttier and Courtier (1999).

The second procedure is called the NMC method (Parrish and Derber 1992) which has been in use at most operational centers. This method approximates the background errors as the average differences between two short-range model forecasts verifying at the same time according to,

$$\mathbf{B} \approx \alpha \mathrm{E}\left\{\left[\mathbf{X}_f\left(48hr\right) - \mathbf{X}_f\left(24hr\right)\right]\left[\mathbf{X}_f\left(48hr\right) - \mathbf{X}_f\left(24hr\right)\right]^{\mathbf{T}}\right\}. \qquad (2.10)$$

In this equation, E denotes the expected value, α is the percentage of this expectation considered to be the background error and subscript f means forecast. Strictly speaking, the background error covariance estimated from the NMC method is the covariance of the model-forecast differences rather than the real forecast errors (if the forecast is used as the analysis background, then the forecast errors are the background errors). Nevertheless, it has been shown to produce reasonable results. The problem, however,

is this estimate of background errors is at best seasonally dependent because the NMC method is based on many forecasts over, e.g., 1 to 2 months. For mesoscale and smaller scale convective systems that are spatially and temporally intermittent, a truly flow dependent background error covariance is essential. The advantages to using an anisotropic covariance in a variational analysis scheme are discussed in Otte et al. (2001).

The third approach to estimating flow-dependent forecast error covariance is known as the ensemble Kalman filter (EnKF) method (Evensen 1994). In this method, an ensemble of forecasts is produced and the forecast error covariance is directly calculated from this ensemble of forecasts. This method has gained much popularity in recent years and is being used in an increasing number of data assimilation studies. The EnKF method does tend to have systematically underestimated forecast error covariance due to the sampling errors for the typically small ensemble sizes employed and due to not effectively taking into account model errors, which leads to too small an ensemble spread that can cause filter divergence or the rejection of observational data by the filter.

The fourth method is represented by the traditional Kalman filter and its various generalizations (Lewis et al. 2006). With this method, a prognostic equation for the time evolution of forecast error covariance is solved explicitly. The extended Kalman filter (EKF) is the extension of the Kalman filter applied to non-linear problems. But the extremely high computational cost of the traditional Kalman filter precludes its use in practical real-time NWP systems. It shares the problem of filter divergence with the EnKF method when the model error is not properly accounted for.

The last practical method is to derive the flow-dependent background error correlation directly from the expected error field. Previous studies have proposed anisotropic correlation functions based on certain physical fields that carry error structure information (Benjamin and Seaman 1985; Benjamin et al. 1991; Riishøjgaard 1998). Among them, Riishøjgaard (1998) proposed an approach to specifying background error covariance for a 2-dimensional problem as follows,

$$B_{ij} = \sigma_i \sigma_j \left[1 + \frac{1}{2} \left(\frac{r_{ij}}{L} \right)^2 \right]^{-1} \exp \left[-\left(\frac{x_i - x_j}{X} \right)^2 \right], \tag{2.11}$$

where σ_i and σ_j are the forecast error standard deviations at points i and j, respectively, r_{ij} is the distance between points i and j, L is the length scale as defined in Daley (1991) which controls the horizontal extent of the correlation, x is the analyzed physical field and X is a length scale in the space of the physical field x and controls the degree of anisotropy of the covariance. L and X can be determined based on observation innovations or from the NMC method. This method to specify a flow-dependent background error covariance is easy to implement and inexpensive to evaluate.

Because we desire to have flow-dependent background error that can be applied at the mesoscale within a 3DVAR framework for water vapor analysis, the fifth approach appears to be most appropriate for our purpose.

2.1.3 Modeling of background error covariance using numerical filters

Two important issues need to be addressed with the 3DVAR analysis. One is the desire to have flow-dependent background error covariance as discussed earlier. The

other is related to the computational implementation and efficiency. Even though computing power is increasing rapidly, we still need to give consideration to the computational cost in meteorological applications, especially for real-time NWP. The dimension of the background error covariance matrix **B** is about 10^7 x 10^7 for realistic atmospheric problems (Courtier 1997). Neither storing **B** nor solving for its inverse required by the variational analysis is possible for operational implementations. Special considerations are required to avoid storing and inverting the full matrix. The background error covariance in the variational analysis effectively plays the role of a filter and it is possible to replace the operations involving the matrix by employing a spatial filter that acts on the analysis increments (Lorenc 1992).

2.1.3.1 Use of explicit spatial filter to model error covariance

Huang (2000) modified the standard 3DVAR scheme, Eq. (2.1), through a simple variable transform to avoid the inversion of the background error covariance matrix **B**. A new control variable is defined as,

$$\mathbf{v} = \mathbf{B}^{-1}(\mathbf{x} - \mathbf{x_b}).$$
(2.12)

The cost function (2.1) is then rewritten as,

$$J(\mathbf{v}) = \frac{1}{2}\mathbf{v}^{\mathrm{T}}\mathbf{B}^{\mathrm{T}}\mathbf{v} + \frac{1}{2}(\mathbf{y}_o - H(\mathbf{Bv} + \mathbf{x}_b))^{\mathrm{T}} \mathbf{R}^{-1}(\mathbf{y}_o - H(\mathbf{Bv} + \mathbf{x}_b)).$$
(2.13)

The gradient of the cost function can be derived as a function of new control variable **v,**

$$\nabla_{\mathbf{v}} J = \mathbf{B}^{\mathrm{T}}\left\{\mathbf{v} + \mathbf{H}^{\mathrm{T}}\mathbf{R}^{-1}\left[H(\mathbf{Bv} + \mathbf{x}_b) - \mathbf{y}_o\right]\right\}.$$
(2.14)

Again, here **H** is the linearized tangent perturbation of *H*.

Huang then used an explicit spatial filter to replace **B** and obtained,

$$J(\mathbf{v}) = \frac{1}{2}\mathbf{v}^{\mathrm{T}}\mathcal{G}\mathbf{v} + \frac{1}{2}\left(\mathbf{y}_o - H\left(\mathcal{G}\mathbf{v} + \mathbf{x}_b\right)\right)^{\mathrm{T}}\mathbf{R}^{-1}\left(\mathbf{y}_o - H\left(\mathcal{G}\mathbf{v} + \mathbf{x}_b\right)\right), \tag{2.15}$$

and the gradient is then

$$\nabla_{\mathbf{v}}J = \mathcal{G}\left\{\mathbf{v} + \mathbf{H}^{\mathrm{T}}\mathbf{R}^{-1}\left[H\left(\mathcal{G}\mathbf{v} + \mathbf{x}_b\right) - \mathbf{y}_o\right]\right\}. \tag{2.16}$$

Here $\mathcal{G}$ is a spatial filter that should be designed based on the *prior* knowledge of **B**. Such a variational analysis scheme using a filter (VAF) does not explicitly compute and store the **B**. Given the formulation of the cost function and its gradient in Eq. (2.15) and (2.16) and assuming the initial guess of the control variable $\mathbf{v} = 0$ (which is same as using $\mathbf{x_b}$ as the first guess of $\mathbf{x}$), the optimal solution is easy to obtain using a minimization algorithm, such as the conjugate gradient algorithm.

For a 2-dimensional univariate analysis problem, assuming a homogeneous and isotropic background error covariance, the $\mathcal{G}$ is,

$$\mathcal{G} = \sigma_b^2 \exp\left(-\frac{r_{ij}^2}{L_r^2}\right) \tag{2.17}$$

which represents the covariance between grid points i and j. Here σ_b^2 is the variance of background error, r_{ij} is the distance between these two points and L_r is the decorrelation length scale. This gives a Gaussian filter which is usually truncated in its spatial span to reduce memory and computational cost, but the truncation can violate the positive definiteness of the covariance matrix. The Lanczos window (see, e.g., Duchon 1979) can be applied to alleviate to some extent the Gibbs problem related to a sharp cutoff window, as proposed by Huang (2000). For practical operations, the effect of **B** operating on a control variable is realized by computing the truncated covariance based on Eq. (2.17) and applying it to the control variable at every grid point. Thus, the

memory usage is much less than directly applying the full matrix **B** on the control variable. If the background error at every grid point is correlated with all other grid points, i.e., if no truncation is done, then the analysis from the VAF method should be exactly the same as that from the standard 3DVAR method using the B calculated from (2.17).

When the flow-dependent error covariance is calculated from an equation such as Eq. (2.11), the use of an explicit filter is straightforward. In our implementation, the covariances surrounding a particular grid point are first computed according to Eq. (2.11) and truncated using the Lanczos window to within a cutoff radius and then applied at this grid point. This should be done point by point to accomplish the role of **B**. Because the filter coefficients change from point to point, and the filter needs to be applied once in each minimization iterative, the computational cost can be saved by calculating the coefficients once and storing them in the memory. Doing so does however require a large amount of memory because each filter can easily require thousands of floating point words in memory storage, assuming the filter spans more than 10 grid points in each of the three dimensions; as a result the total storage requirement by the filters is this number multiplied by the number of grid points. Further, applying a three dimensional filter at each grid point is also computationally expensive; it involves 6-level loops! Still, because of its simplicity in implementation, it is chosen for the GPS *SWV* analysis as our first attempt. The more computationally efficient though implementation-wise much more complex recursive filter is the alternative, which is discussed next.

2.1.3.2 Use of recursive spatial filter to model error covariance

A computationally more efficient alternative to the explicit filter is the implicit recursive filter, and it has been demonstrated that a simple isotropic recursive filter with multiple iterations asymptotically approaches an explicit Gaussian filter as the iterations tend to infinity and can be used to model the effect of background error covariance (Lorenc 1992; Hayden and Purser 1995). Purser et al. (2003a) further illustrated that a high-order (e.g., 4th-order) isotropic recursive filter with only one pass can closely approximate a Gaussian filter. Thus the use of a recursive filter to model error covariance is feasible and efficient and well suited for real-time applications. For this reason, recursive filters, with both isotropic and anisotropic options, are used in a number of operational 3DVAR systems, including those at NCEP, for both global and regional analyses (Wu et al. 2002; Purser et al. 2003a, b; Purser 2005). Here, we point out that the flow-dependent error covariance is typically anisotropic in spatial directions while the flow-independent one is often assumed isotropic. In any case, an isotropic filter can only model flow-independent covariances. In this study, we will use the words of flow-dependent (flow-independent) and anisotropic (isotropic) interchangeably.

2.1.3.2.1 Variable transform

To avoid the inversion of **B** and also to improve the conditioning of the cost function to speed up the convergence of the minimization algorithm, a new control variable, **z**, is defined in our 3DVAR system using recursive filters,

$$\mathbf{z} = \mathbf{D}^{-1}\delta\mathbf{x}, \tag{2.18}$$

in which $\delta\mathbf{x} \equiv \mathbf{x} - \mathbf{x}_b$ is the increment of **x**, and **D** is defined as

$$\mathbf{DD}^{\mathrm{T}} = \mathbf{B}. \tag{2.19}$$

Thus, matrix $\mathbf{D}$ has the same eigenvectors as matrix $\mathbf{B}$ and its eigenvalues are the same as the square root of the eigenvalues of $\mathbf{B}$. The cost function J in Eq. (2.1) can then be rewritten as,

$$J(\mathbf{z}) = \frac{1}{2}\mathbf{z}^{\mathrm{T}}\mathbf{z} + \frac{1}{2}\left(\mathbf{y}_o - H\left(\mathbf{Dz} + \mathbf{x}_b\right)\right)^{\mathrm{T}}\mathbf{R}^{-1}\left(\mathbf{y}_o - H\left(\mathbf{Dz} + \mathbf{x}_b\right)\right), \tag{2.20}$$

and its gradient is

$$\nabla_{\mathbf{z}}J = \mathbf{z} + \mathbf{D}^{\mathrm{T}}\mathbf{H}^{\mathrm{T}}\mathbf{R}^{-1}\left(\mathbf{HDz} - \mathbf{d}\right), \tag{2.21}$$

where $\mathbf{d}$ and $\mathbf{H}$ are defined as in Eq. (2.4) and Eq. (2.2).

The task of applying operator $\mathbf{D}$ in Eqs. (2.20) and (2.21) can be achieved by the use of a recursive filter. Purser et al. (2003a, b) describe the construction and application of numerical recursive filters for synthesizing the background error covariances for variational analysis. Those two papers, respectively, deal with spatially homogeneous and isotropic, and spatially inhomogeneous and anisotropic covariances with recursive filters. The basic theory of recursive filter is introduced next in one dimension to illustrate the implementation of recursive filters in 3DVAR.

2.1.3.2.2 One-dimensional recursive filter

The general n^{th}-order one-dimensional (1D) recursive filter has two steps. First the advancing step:

$$q_i = \beta p_i + \sum_{j=1}^{n}\alpha_j q_{i-j}, \tag{2.22}$$

where p is the input and q is the output of the advancing step and n is the order of the recursive filter. Here, i is the grid point index and must be treated in increasing order so

that the quantities on the right hand side of the equation are already known. The advancing step is followed by the backing step:

$$s_i = \beta q_i + \sum_{j=1}^{n} \alpha_j s_{i+j} \qquad (2.23)$$

where s is the final output from the recursive filter and index i here must be treated in decreasing order. Parameters α_j and β are the filter coefficients and they have a relationship as shown

$$\beta + \sum_{j=1}^{n} \alpha_j = 1, \qquad (2.24)$$

in order that the homogeneous forms of these filters conserve the quantity being filtered.

We note here that when the above recursive filter is applied to a limited area domain, as in our case, special boundary treatment is needed which is discussed by Purser et al. (2003a) in their appendices. The recursive filter operations can be easily performed in the advancing step according to Eq. (2.22) and the backing step according to Eq. (2.23) once the filter coefficients (α_j and β) are determined. A fourth-order recursive filter can effectively model the explicit Gaussian filter with a single pass (Purser et al. 2003a). Given general 1D filter equations, a 3D filter can be created by the applications of multiple one-dimensional filters in each direction.

2.1.3.2.3 'Aspect tensor' and 'hexad algorithm'

For a 3D problem, if the background error correlation is isotropic, one simply applies three one-dimensional filters, one in each coordinate direction. But if the error correlation is anisotropic, for instance, as given by Eq. (2.11), the background error pattern can be stretched or flattened in directions oblique to the alignment of the grid

coordinates. The implementation of the recursive filter for such anisotropic cases is much more complicated. The effect of error correlation in Eq. (2.11) can be constructed by applying at each grid point six recursive filters along six directions (including the diagonal directions) corresponding, in general, to a special configuration (a "hexad") of oblique lines of the grid.

This configuration of six filtering directions and the corresponding six scalar smoothing weights along these lines are determined from the 'aspect tensor' by a rapid iterative technique, the so-called 'hexad algorithm', as described briefly in Purser et al. (2003b) and in a much greater technical detail in Purser (2005). The 'aspect tensor' is defined to be the normalized centered second-moment of the response of the filter representing the desired covariance locally. It therefore serves as a convenient way of characterizing the local spatial structure of the covariance. The term goes beyond the concept of the 'aspect ratio', which only describes the ratio of vertical and horizontal scales in the simplest horizontally-isotropic case, because the tensorial character expresses not just the absolute scale, but the dominant shape components.

The most important point to note about the hexad algorithm is that the generic 'hexad' of lines is not any arbitrary set of six generalized grid lines; the rules for the construction of a legal hexad require that the smallest discrete steps, or 'generators', of the first three of a hexad's directions, expressed in grid units as integer 3-vectors, form a parallelepiped of unit volume. Furthermore, the remaining three lines' generators consist of the three distinct possible differences among the first three generators. By these rules, the six generators of a hexad, together with their negatives, collectively define the 12 vertices of a distorted 'cuboctahedron' embedded within the lattice of local grid

displacements. As is shown rigorously in Purser (2005), these constitutive rules defining a legal hexad, together with the assumption that the centered second moments of a sequence of filters combine additively, and the further reasonable stipulation that the hexad weights on which the aspect tensor is projected are each nonnegative, generally ensures a unique choice of a hexad of filtering directions and weights, apart from the vacuous ambiguity of directions in special transitional cases where one or more hexad weights vanish. (A negative weight would imply a negative amount of diffusion for a Gaussian smoother, which is physically meaningless, but a vanishing hexad weight simply implies the acceptable limiting case of no smoothing in that direction.).

The practical operation of finding the appropriate hexad involves a simple convergent iteration and works as follows. The algorithm starts with a structurally legal ('feasible') hexad (not necessarily the correct one, though) and carries out the appropriate linear projection of the intended aspect tensor's six independent components into the hexad's set of six directional smoothing weights, regardless of whether or not these smoothing weights are all positive quantities. If they are all positive (or non-negative, at least), then the problem is already solved. More commonly, one or a few of the weights will be negative, and another putative feasible hexad needs to be selected. Fortunately, there exists a systematic way of doing this, which makes the convergence of the algorithm very fast: the negative weight of largest absolute magnitude is identified and its associated generalized grid line is excluded from the hexad. Owing to the special definition of a feasible hexad, there is always one, but only one, hexad to choose from that shares the other five lines but replaces the offending one. Moreover, in

a well-defined sense, the new alternative hexad is always closer to the solution than the one it replaces. The process is repeated and terminated once a set of six non-negative smoothing weights is found. These iterations can formally be interpreted as a special case of the Simplex Algorithm of linear programming (Dantzig 1963).

2.2 The Global Positioning System and its observations

2.2.1 The Global Positioning System (GPS)

The GPS system consists of three components: a space segment, a control segment and a user segment. The space segment is a satellite constellation originally designed to include 24 satellites distributed in 6 orbital planes with four satellites in each plane (Fig. 2.1) but now it consists of 28 satellites in the 6 orbital planes. The control segment is a network of monitoring and tracking of the satellites. The Master Control facility is located at the Schriever Air Force Base in Colorado. These stations measure signals from the satellites which are incorporated into orbital models for each satellite. The models calculate precise orbital data (ephemeris) and satellite clock corrections for each satellite. The Master Control station uploads ephemeris and clock data to the satellites. The satellites then send subsets of the orbital ephemeris data to GPS receivers over radio signals.

The GPS transmits microwave signals at two L-band frequencies, generally referred as the L1 (1575.2 MHZ or about 19 cm) and L2 (1227.6 MHZ or about 24 cm) carrier frequencies. The choice of L-band frequencies allows GPS to work well under all weather conditions, i.e., there is little attenuation. But the signal is delayed and bent when it goes through the atmosphere. We can derive the delay and bending due to

atmospheric effects by analyzing the GPS data. This is the basis of atmospheric GPS

measurement. There are two kinds of GPS receiver systems: ground-based and space-
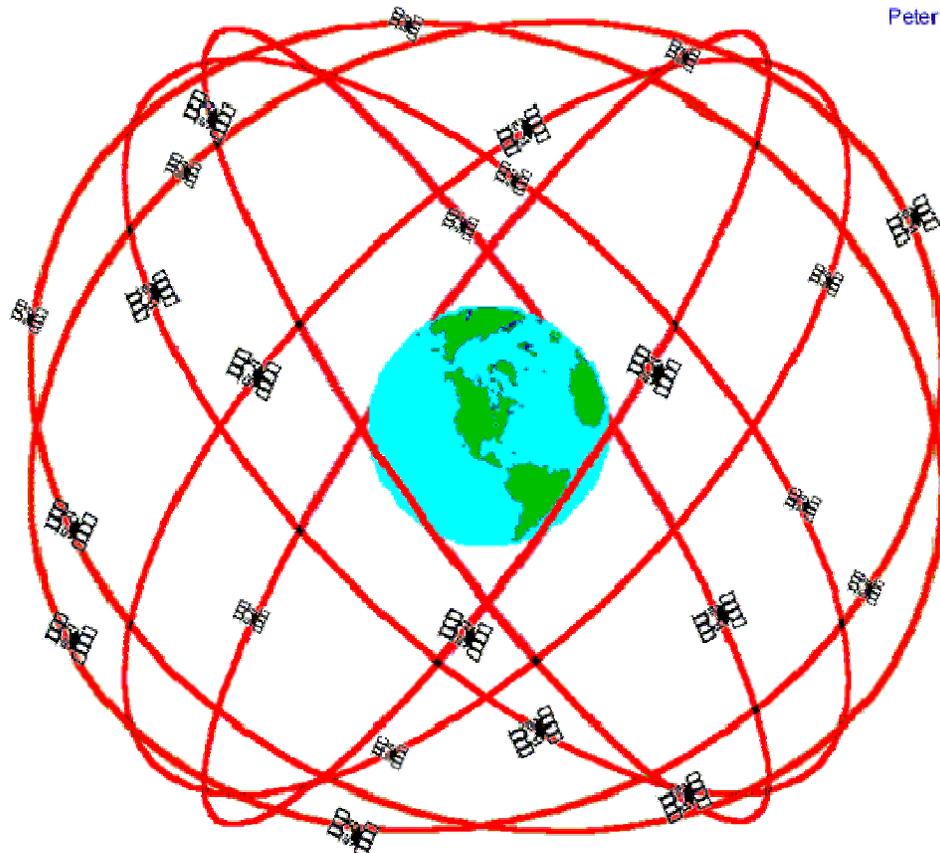
GPS Nominal Constellation
24 Satellites in 6 Orbital Planes
4 Satellites in each Plane
20,200 km Altitudes, 55 Degree Inclination

Fig. 2.1 GPS satellite constellation (Peter Dana, from the webpage
http://www.colorado.edu/geography/gcraft/notes/gps/gps_f.html)

based receivers. Ground-based receivers are much cheaper and networks can be easily

installed. The space-based receivers are installed on the Low Earth Orbit satellites

(LEO), so they are relatively expensive. However, the space-based receivers can

provide more observational variables, including the pressure, temperature, refractivity, ionospheric electron density etc. Very recently, the Constellation Observing System for Meteorology Ionosphere and Climate (COSMIC) constellation consisting of 6 satellites was launched successively and data have begun to be received. In addition, there are currently about 400 ground-based GPS receivers distributed around the USA (Fig. 2.2). The ground-based observations can provide tropospheric moisture information, at high temporal and spatial resolutions that other instruments can not observe well.
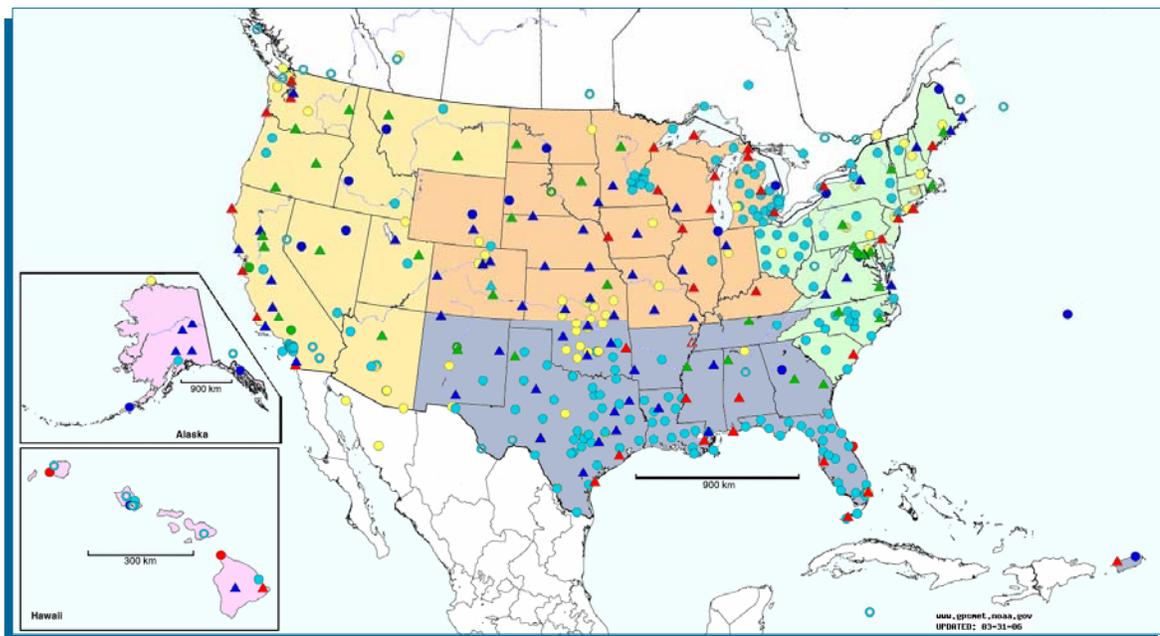
Fig. 2.2 ground-based GPS network which currently consists of 407 sites (from webpage http://www.gpsmet.noaa.gov/jsp/index.jsp).

2.2.2 GPS data from ground-based receivers

In this section, we introduce the observation variables from ground-based receivers that have been used in previous data assimilation studies. The microwave radio signals transmitted by GPS satellites are delayed by the atmosphere as they

propagate to the ground-based GPS receivers. The total delay L can be formulated by integrating the refractivity $N(s)$ along the slant path s between the GPS satellite and the ground-based receiver as shown in Eq. (2.25)

$$L = 10^{-6} \int_s N(s)\,ds = 10^{-6} \int_s \left(77.6\frac{P}{T} + 3.73 \times 10^{-5} \frac{P_w}{T^2} - 4.03 \times 10^7 \frac{n_e}{f^2} \right) ds, \qquad (2.25)$$

where T is the temperature in K, P and P_w are the total and water vapor pressure in hPa, respectively, n_e is the free electron density in m^{-3} and f is the GPS signal frequency in Hz. Above 90 km, the pressure and water vapor terms are negligible, so the delay is mainly caused by the charged field of free electrons. This delay is called slant ionospheric delay in units of length (the third term in the right hand side of Eq. (2.25)) and can be calculated to millimeter accuracy with the use of a linear combination of measurements by a dual-frequency GPS receiver. Two other terms on the right hand side of Eq. (2.25) are responsible for the delay when the signal goes through the neutral troposphere. The delay caused by water vapor is called slant wet delay (SWD, the second term in the integral). The first term is called slant hydrostatic delay (SHD) or dry delay to distinguish it from the wet delay. The sum of the wet and hydrostatic delays is the slant total delay (STD = SHD + SWD). The zenith delay is defined as the slant delay scaled to its equivalent delay if the satellite was at zenith direction as shown below,

$$ZTD = ZHD + ZWD = \frac{SHD}{m_h(\theta)} + \frac{SWD}{m_w(\theta)}. \qquad (2.26)$$

In this equation, θ is the elevation angle of the GPS satellite to a ground-based receiver and the terms $m_h(\theta)$ and $m_w(\theta)$ are the mapping functions of the hydrostatic and wet delays with respect to the zenith direction (Davis et al. 1985; Niell 1996). ZTD, ZHD and ZWD are respectively the zenith total, hydrostatic and wet delay. The ZHD can be

obtained with good knowledge of surface pressure (Davis et al. 1985) so that *SHD* can be derived from *ZHD* with the use of mapping function $m_h(\theta)$. The *SHD* can also be calculated by directly integrating the hydrostatic term in the Eq. (2.25) with the pressure and temperature estimated from a numerical model. Therefore, the *SWD* is determined after subtracting the ionospheric delay and the *SHD* from the GPS measured geometric delay. Then all *SWD*s can be projected to the zenith direction and averaged over a period of time (e.g., 30 minutes) under the assumption that the atmosphere is azimuthally homogeneous and isotropic to obtain the *ZWD*. Further, the precipitable water (*PW*, defined as the vertically integrated water vapor in an atmospheric column in units of length) can be calculated from *ZWD* (Bevis et al. 1994; Duan et al. 1996) through this equation,

$$PW = \Pi \bullet ZWD = \frac{1}{0.373\rho R_v} T_m \bullet ZWD, \tag{2.27}$$

where Π is a dimensionless conversion parameter which is generally near 0.15, i.e., 1 mm *PW* corresponds to 6.5 mm *ZWD*. ρ is the air density and R_v the gas constant for water vapor. T_m is known as the weighted mean temperature of the atmosphere and has a relationship with the surface temperature T_s given by,

$$T_m = 70.2 + 0.72 \times T_s. \tag{2.28}$$

In above equation, the temperatures are in kelvins. This approximated relationship is with an rms relative error of less than 2% (Bevis et al. 1992). Similarly, the slant-path integrated water vapor (*SWV*) is nearly proportional to the *SWD* according to

$$SWV = \Pi \bullet SWD. \tag{2.29}$$

The methods described above provide reasonably accurate *PW* and *SWV* observations. Comparisons between GPS and microwave water vapor radiometers (MWRs) indicate an agreement to about 5% which represents approximately 1.5 mm root mean square (RMS) error for receiver stations in middle-latitudes where *PW* averages around 30 mm and varies from 10 to 50 mm (Rocken et al. 1995). Comparisons of GPS *PW* to the data from radiosondes also show its accuracy to be about 1.5 mm. Compared to the *PW* observations, the *SWV* data provide the opportunity to characterize the atmospheric moisture field in a more detailed and precise manner through analyzing the data along the slant paths.

2.2.3 Advantages of GPS measurements

There are many merits of GPS measurements. First of all, they can continuously provide moisture observations under all weather conditions. Secondly, GPS measurements require no external calibration. GPS observations have the property of high temporal resolution and the potential of high spatial resolution as well. The measurement accuracy of the integrated precipitable water is comparable to that made by the radiosonde, but the GPS observation is a completely independent measurement system. All of these advantages make GPS a valuable system for environmental modeling, regional weather forecasting and for the verification of both models and other sources of observations.

Chapter 3
Retrieval of Moisture from Slant-path Water Vapor Observations of a Hypothetical GPS Network using a 3DVAR with Anisotropic Background Error[1]

3.1 Introduction

As mentioned in Chapter 1, accurately characterizing the three-dimensional (3D) distribution of water vapor in the atmosphere is very important for the understanding and prediction of mesoscale and storm-scale weather, especially with regard to quantitative precipitation forecast (QPF, Emanuel et al. 1995). QPF skills have been improving rather slowly owing to the high spatial and temporal variability of water vapor. Thus, high-resolution observations of 3D water vapor have the potential to significantly improve the prediction of precipitation and severe weather. In recent years, space- and ground-based GPS receivers have seen significant development and can potentially provide water vapor measurements with high resolution under virtually all weather conditions (Businger et al. 1996; Ware et al. 2000; Wolfe and Gutman 2000; Bengtsson et al. 2003).

---

[1] This chapter is an extended version of our published paper: Liu, H. and M. Xue, 2006: Retrieval of moisture from slant-path water vapor observations of a hypothetical GPS network using a three-dimensional variational scheme with anisotropic background error. *Mon. Wea. Rev.*, **134,** 933–949.

Most of the past data assimilation or data impact studies related to ground-based GPS water vapor observations deal with the precipitable water (*PW*) or zenith wet delay (*ZWD*) data. (e.g., Kuo et al. 1993; Kuo et al. 1996; Guo et al. 2000; Falvey and Beavan 2002). As described in section 2.2.2, *ZWD* is a derived product that is obtained by projecting *SWD* observations onto the zenith then averaging all observations over a certain time period under the assumption of azimuthal isotropy and horizontal homogeneity (Rocken et al. 1993). Further, *PW* is derived from *ZWD* in a similar way as *SWV* is from *SWD*, i.e., it is linearly related to *ZWD* (see Eq. (2.27)). A more recent study of Cucurull et al. (2004), using a 3DVAR scheme, directly assimilates zenith total delay (*ZTD*) which is also a derived product similar to *ZWD*, except it is for the total delay. Simulated and real *ZTD* data were assimilated via a four-dimensional variational (4DVAR) scheme into a mesoscale model by De Pondeca and Zou (2001a; 2001b), respectively. These studies have all found a positive impact of assimilating the GPS data on precipitation forecasts, though in some cases, the impact is small.

There exists a significant loss of information in *ZWD* or *ZTD* data, however, compared to the original slant-path data due to the spatial and temporal averaging involved in their derivation. It should, therefore, be beneficial to use the slant path total or wet delay or slant-path water vapor data directly. We do point out here that since the slant-path measurement represents an integrated quantity of water vapor along each ray path, it, as in the case of *PW* and *ZWD*, does not provide information on the vertical distribution of water vapor. It is hypothesized here that in the case of slant-path data (in contrast to *PW* and *ZWD* data), the multiple overlapping ray paths, forming a 'net' covering the atmosphere, are helpful in recovering the 3D structure of moisture. In the

case of variational analysis, the inclusion of the analysis background, a good knowledge of the background error structure as well as the effective utilization of such knowledge, should all be helpful. It is the goal of this study to test these hypotheses.

Currently, over the United States, there are approximately 400 surface GPS sites for which precipitable water observations are available in near real time. These sites include those from the NOAA Forecast Systems Laboratory (FSL) network (now Global Systems Division, GSD) and the SuomiNet (Ware et al. 2000). Currently slant-path GPS data are available only from SuomiNet sites and selected GSD sites. The potential availability of much more slant path data and their decent accuracy have prompted interests in analyzing and assimilating such data directly into numerical models. A limited number of studies have been done of these data, including MacDonald et al. (2002) and Ha et al. (2003), both of which utilize simulated data from a hypothetical GPS network. This was done partly because actual slant-path data are very limited and their spatial coverage and resolution remain poor.

In MacDonald et al. (2002), a 3D variational method is used to analyze *SWV* data collected by a hypothetical high-resolution network of ground-based GPS receivers. It is shown that the 3D moisture field can be recovered from the *SWV* data in combination with the surface moisture observations taken at the same sites as the receivers. Water vapor soundings from a low-density network are also used to aid their analysis. Ha et al. (2003) showed, using a 4DVAR system, that the direct assimilation of simulated *SWD* is superior to assimilating the derived *PW* data in terms of both recovering water vapor information and improving short-range precipitation forecasting.

In this study, we focus on the analysis of *SWV* data (instead of *PW* data) and choose to develop and use for the analysis a more complete 3DVAR system that employs an anisotropic spatial filter for modeling the flow- or field-dependent background error covariances. As an initial study, we perform our analysis of water vapor in a univariate 3DVAR system where we focus most of our attention on the impact of flow-dependent background error covariances on the quality of analysis. The flow-dependent background error is modeled using an anisotropic spatial filter. The use of anisotropic spatial filter is a unique aspect of this study. To our knowledge, it has never been applied specifically to the analysis of GPS data. Since the GPS data are not point measurements of the analysis variables themselves, but rather integrated quantities, the variational approach is a natural choice.

As in MacDonald et al. (2002) and Ha et al. (2003), we also use simulated data to test our analysis system. The use of simulated data from a hypothetical receiver network gives us flexibility and complete control over the network design, data resolution and quality. Further, the knowledge of the truth allows us to unambiguously assess the quality of analysis. The roles of observation system simulation experiments (OSSE) in the design, development and evaluation of future observing systems are discussed in detail by Lord et al. (1997) and also by Atlas (1997). Another reason for using simulated data is that a high-density GPS receiver network with large spatial coverage is not yet available, at least not over the United States. Ultimately, however, the goal of improving the moisture analysis is to improve NWP, especially the prediction of precipitation. The impact of simulated and real GPS slant-path data

analyzed through our 3DVAR procedure on short-range precipitation forecast will be the subject of future studies.

This chapter is organized as follows: section 3.2 introduces our 3DVAR analysis system and section 3.3 describes the generation of simulated GPS *SWV* data from a mesoscale model forecast. Results from analysis experiments are presented in section 3.4. Further discussion of the effectiveness of our scheme is given in section 3.5 through sensitivity experiments. Summary and conclusions are given in section 3.6, together with a plan for future work.

3.2 3DVAR analysis system with explicit Gaussian filter

In this work, we follow the standard practice of 3DVAR data assimilation for NWP (Lorenc 1981; Daley 1991), also described in section 2.1, by including the analysis background. Thus, the cost function includes both background and observation terms. For moisture analysis, a weak non-negative-moisture constraint is also included in this cost function. The use of a background makes the problem over-determined and makes the analysis feasible for realistic numbers of GPS satellites and ground-based receivers, because the number of control variables, which is the number of grid point values of moisture in our case, is much greater than the number of (*SWV* plus surface) observations at any instance. Because the GPS network does not directly observe point values of water vapor, the analysis involves 'retrieving' or 'recovering' the 3D distribution from the integral observations. We therefore often refer to the analysis process as 'retrieval'.

The previous 3DVAR work of MacDonald *et al*. (2002) differs from this study by lumping together all GPS data in the analysis domain during a one hour interval and treating them as observations at the analysis time so that the number of observations is significantly increased. Because their 3DVAR system does not include a background constraint, noise problems were encountered during their initial analyses. They obtained reasonable analyses by employing a multi-grid procedure, in which the analyses were performed on two grids of different resolutions repeatedly, while the solutions were transferred back and forth between the grids many times. While such a procedure seems to work, the amount of implicit smoothing imposed upon the analysis by such a procedure is difficult to assess, especially in terms of the physically meaningful background error correlations.

In this work, the spread of observation increments in space is controlled by the background error covariances, which in some experiments are spatially inhomogeneous and flow-dependent. In addition, this 3DVAR system is formulated in a general terrain-following coordinate system; therefore, its analysis can be used to directly initialize a model formulated in the same coordinate system.

The initial cost function of our 3DVAR system is defined as,

$$J(x) = J_b(x) + J_{swv}(x) + J_{sfc}(x) + J_c(x), \tag{3.1}$$

where,

$$J_b(\mathbf{x}) = \frac{1}{2}(\mathbf{x} - \mathbf{x}_b)^T \mathbf{B}^{-1}(\mathbf{x} - \mathbf{x}_b), \tag{3.1a}$$

$$J_{swv}(\mathbf{x}) = \frac{1}{2}\left[H_{swv}(\mathbf{x}) - \mathbf{SWV}\right]^T \mathbf{R}_{swv}^{-1}\left[H_{swv}(\mathbf{x}) - \mathbf{SWV}\right], \tag{3.1b}$$

$$J_{sfc}(\mathbf{x}) = \frac{1}{2}\left[H_{sfc}(\mathbf{x}) - \mathbf{q}_{v_{sfc}}\right]^T \mathbf{R}_{sfc}^{-1}\left[H_{sfc}(\mathbf{x}) - \mathbf{q}_{v_{sfc}}\right], \tag{3.1c}$$

$$J_c(\mathbf{x}) = \frac{1}{2}\left(\frac{\mathbf{x}-|\mathbf{x}|}{2}\right)^T W_c \left(\frac{\mathbf{x}-|\mathbf{x}|}{2}\right). \tag{3.1d}$$

The cost function J given in Eq. (3.1) is composed of four terms. The first is the background term, defined in (3.1a), which measures the departure of the control variable from the background. The second term defined in (3.1b) is the observational terms for GPS SWV observations and it, J_{swv}, represents the departure of the analyzed from the observed SWV measured by the ground-based GPS receivers. Since the ground-based GPS receiver sites are commonly equipped with regular meteorological sensors, regular surface water vapor observations can be made together with SWV observations. Therefore, J_{sfc} is included in the cost function to better analyze moisture structure near the surface. Similar to second term, the third term defined in (3.1c) is called surface moisture observation term representing the difference of analysis and observation at observation station. The physical requirement that water vapor is nonnegative is expressed in the last term, (3.1d), as a weak constraint. The operational NCEP global spectral statistical interpolation (SSI) analysis (Parrish and Derber 1992) also uses a weak constraint, but on relative humidity being positive and not supersaturated. Being a weak constraint, it does not strictly enforce the positivity of the analyzed water vapor field, however. A final correction can be applied to make the analysis stable in NWP equations by changing negative water vapor values to be very small. The definitions of the variables in the equations are given as follows.

$\mathbf{x}$ is the analysis or control variable vector, which in our case is the 3D specific humidity field.

$\mathbf{x}_b$ is the analysis background or first guess, of specific humidity in this case.

$\mathbf{q}_{v_{sfc}}$ is the surface observation vector of specific humidity.

B is the background error covariance matrix. This study focuses on the effect of **B** in isotropic and anisotropic forms on the analysis. Assuming the background error variances are homogeneous, i.e., equal to a constant in the analysis domain, then **B** is the product of this constant and background error correlation matrix.

SWV is a vector containing *SWV* observations.

H_{swv} is the forward observation operator which calculates integrated *SWV* observations between GPS satellites to ground-based receivers from water vapor values at grid points (see Eq. (3.5)).

H_{sfc} is the forward observation operator for surface observations of specific humidity which is the horizontal interpolation at the surface in this study.

$\mathbf{R}_{swv}$ and $\mathbf{R}_{sfc}$ are, respectively, the observation error covariances for *SWV* and surface moisture observations. The observation errors are usually assumed to be diagonal under the assumption that observation errors are not correlated (some of the actually correlated errors can usually be effectively removed through bias correction procedures, see e.g., Harris and Kelly 2001). Further, the diagonal elements of $\mathbf{R}_{swv}$ ($\mathbf{R}_{sfc}$) are the *SWV* (surface moisture) observation error variances which are assumed here to be independent of stations, so $\mathbf{R}_{swv}$ ($\mathbf{R}_{sfc}$) can be simplified as a constant error variance multiplying an identity matrix, i.e., $\mathbf{R}_{swv} = \sigma^2_{swv}\mathbf{I}$ and $\mathbf{R}_{sfc} = \sigma^2_{sfc}\mathbf{I}$. The magnitude of error variances, compared to the background error variances, determines the relative weight of observations and background for the analysis.

W_c is the weighting coefficient for nonnegative-water-vapor weak constraint.

Given that $\mathbf{R}_{swv} = \sigma_{swv}^2 \mathbf{I}$ and $\mathbf{R}_{sfc} = \sigma_{sfc}^2 \mathbf{I}$, the $\mathbf{R}_{swv}^{-1}$ and $\mathbf{R}_{sfc}^{-1}$ in Eqs. (3.1b) and

(3.1c) can be replaced by σ_{svw}^{-2} and σ_{sfc}^{-2}, respectively, or by $W_{swv} = \sigma_{swv}^{-2}$ and $W_{sfc} = \sigma_{sfc}^{-2}$,

which we call the weighting coefficients for the *SWV* and surface observation terms.

Similarly, as will be discussed later, the background term in Eq. (3.1a) will be

proportional to a weighting coefficient, W_b, that is equal to the inverse of the

background error variance, i.e., $W_b = \sigma_b^{-2}$.

In this study, except for one experiment, the simulated data are assumed error-

free, i.e., no error is added to the simulated observations. This is done because we are

interested in determining how well, under an idealized error-free condition, a 3DVAR

procedure as developed here can retrieve the 3D structure of the moisture field from the

slant-path water vapor data, which are integrated quantities along the slant paths rather

than local observations. The answer to this question was not obvious.

Theoretically, the weighting coefficients of the observation terms should be

infinitely large when the observations are error-free, which means the elimination of

background term in the cost function because of the relative magnitudes of the terms.

Without the background term, our analysis problem is under-determined. To retain the

effect of the background term, in particular, the structure information contained in the

background error covariance, we choose relative weights of 1, 100, 500 and 50 for the

four terms in the cost function. The much higher weights given to the observation terms

reflect the much higher accuracy of the observations as compared to the background,

and the differences in the weights are sufficiently large to ensure a close fit of the

analysis to the observations. Here the surface observations are given more weight

because they tend to be more accurate. Finally, we point out that it is the spatial

structure of the background error correlation that determines the spatial spread of the observation information (see, e.g., Kalnay 2002); the small weight of the background term does not diminish this role.

As discussed in section 2.1.3.1, because the dimensionality of **B** is very large for typical meteorological problems, the direct inversion of **B** as required in Eq. (3.1a) is never attempted. A variable transform is given same as in Eq. (2.12) and the weighting coefficients W_{swv} and W_{sfc} are utilized in the Eqs. (3.1b) and (3.1c), then the cost function in Eq. (3.1) is redefined as,

$$
\begin{aligned}
J(\mathbf{v}) = &\frac{1}{2}\mathbf{v}^{\mathrm{T}}\mathbf{B}^{\mathrm{T}}\mathbf{v} + \frac{1}{2}\Big[H_{swv}\big(\mathbf{Bv}+\mathbf{x}^{b}\big) - \mathbf{SWV} \Big]^{\mathrm{T}} W_{swv}\Big[H_{swv}\big(\mathbf{Bv}+\mathbf{x}^{b}\big) - \mathbf{SWV} \Big] \\
&+ \frac{1}{2}\Big[H_{sfc}\big(\mathbf{Bv}+\mathbf{x}^{b}\big) - \mathbf{q}_{v_{sfc}} \Big]^{T} W_{sfc}\Big[H_{sfc}\big(\mathbf{Bv}+\mathbf{x}^{b}\big) - \mathbf{q}_{v_{sfc}} \Big] \\
&+ \frac{1}{2}\left(\frac{\big(\mathbf{Bv}+\mathbf{x}^{b}\big) - \big|\mathbf{Bv}+\mathbf{x}^{b}\big|}{2} \right)^{\mathrm{T}} W_{c}\left(\frac{\big(\mathbf{Bv}+\mathbf{x}^{b}\big) - \big|\mathbf{Bv}+\mathbf{x}^{b}\big|}{2} \right).
\end{aligned}
\tag{3.2}
$$

This new form of cost function contains no inversion of **B**. Moreover, we will apply an explicit spatial filter to model the effect of the **B** matrix instead of calculating and storing the matrix directly. Such a new variational analysis scheme is simpler and more flexible in practical implementations.

Eq. (2.17) is used to represent **B** for a homogeneous and isotropic background error covariance. It gives a Gaussian filter which is simple and easy to implement. For easy comparison with the definition of anisotropic covariance later explained in Eq. (3.4), we rewrite the Eq. (2.17) here as,

$$
b_{ij} = \sigma_{b}^{2}\exp\left(-\frac{r_{ij}^{2}}{L_{r}^{2}} \right).
\tag{3.3}
$$

The use of isotropic background error covariances is based on the assumption that background errors at nearby points are similar (Riishøjgaard 1998). But actual background errors are usually flow-dependent and spatially anisotropic and the use of flow-dependent covariances in the analysis should improve the results, especially when data are sparse. Therefore, an anisotropic filter is considered for modeling the flow-dependent **B** matrix. The following expression can be used to model the anisotropic **B** matrix,

$$b_{ij} = \sigma_b^2 \exp\left[-\left(\frac{r_{ij}}{L_r}\right)^2 \right] \exp\left[-\left(\frac{f_i - f_j}{L_f}\right)^2 \right] \qquad (3.4)$$

where f is a field whose pattern represents that of the background water vapor error which we will call the error field. In this study, f is either the true error of the background water vapor or an estimate of background error. L_f is the length scale in background error field space, in contrast to the length scale L_r in physical space. It is in units of g kg^{-1} for our moisture retrieval experiments and determined by the de-correlation scale of background error in terms of the spatial gradient of f. It controls the degree of the anisotropy. The new background error covariance between any two points defined by Eq. (3.4) will follow the shape of the error field and fall off rapidly in the direction of strongest gradient, while the isotropic component of covariance will dominate in directions where the error changes slowly. Eq. (3.4) shows that, as L_f goes to infinity, the anisotropic covariance reduces to the isotropic form in Eq. (3.3).

The isotropic and anisotropic filters will be used separately to model the behavior of the background error covariances, and their results will be compared.

3.3 Hypothetical GPS network and the generation of *SWV* data

For the reasons stated in the introduction to this chapter, simulated data are used to conduct retrieval experiments with our analysis system. The model used to produce the 'truth' field is the Advanced Regional Prediction System (ARPS, Xue et al. 2000; 2001; 2003) which is a nonhydrostatic atmospheric model formulated in a generalized terrain-following coordinate. High-resolution observations from hypothetical GPS networks are created from a forecast field for a dryline case that occurred on June 19, 2002 over the Southern Great Plains of the United States during the CAPS real-time forecast period (Xue et al. 2002) for IHOP_2002 (Weckwerth et al. 2004). The ARPS model is initialized using analysis of the ARPS Data Analysis System (ADAS, Brewster 1996, 2002) at 1200 UTC June 19, 2002, and is integrated for 8 hours. The computational domain has a horizontal grid spacing of 9 km and 40 layers in the vertical. The vertical grid is stretched from a minimum grid spacing of 100 meters near the surface. Considering that in the near future, the mean spacing of network of GPS ground receivers will probably not be much less than a hundred kilometers, the scale of water vapor distribution we can obtain will probably be no finer than the mesoscale. The 9-km 8-hour forecast field is therefore thinned by sampling or picking specific humidity values every 4 grid points, yielding a resolution of 36 km and a horizontal grid size of 46×41. This gridded field is defined as the truth of the atmospheric moisture and is sampled, using Eq. (3.5) given in the following, to generate the hypothetical GPS

SWV observations. The specific humidity field from the truth, on the grid of 36 km resolution, is presented in Fig. 3.1.
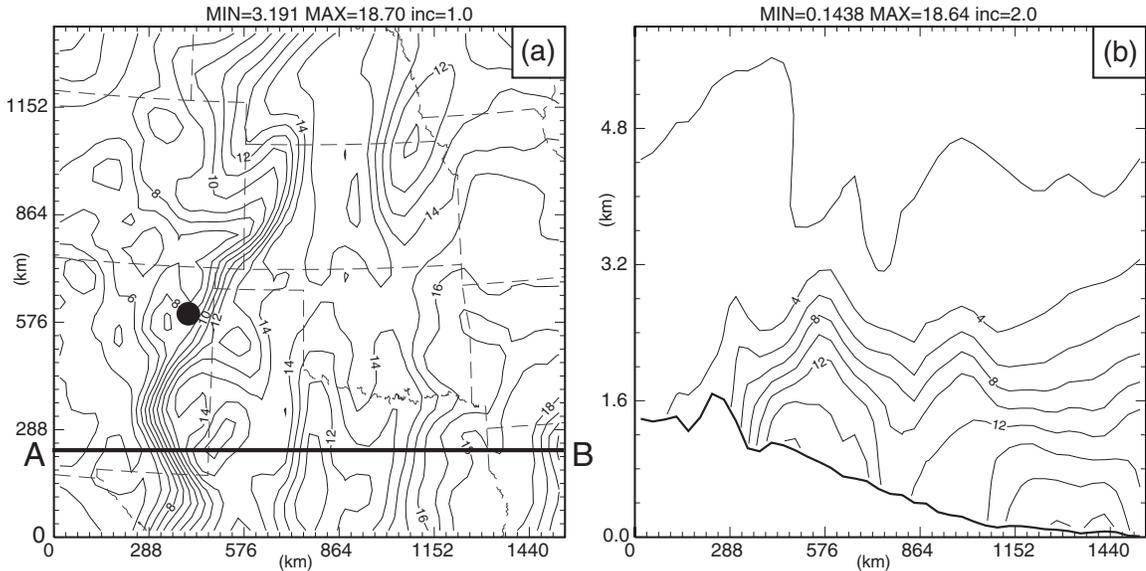
Fig. 3.1 Specific humidity field (g kg-1) from an ARPS truth simulation for the IHOP case of 2000UTC 19 Jun 2002: (a) at the surface and (b) in the east-west vertical cross-section at y = 234 km (along thick line A-B). A roughly north-south zone of strong horizontal moisture gradient is located in western Kansas, the Oklahoma panhandle and eastern New Mexico, representing the dryline. In vertical cross-section, a boundary between the dry and moist air is oriented nearly vertically in the lowest 1.5 km then turns horizontal to the east.

A roughly north-south zone of strong horizontal moisture gradient is located in western Kansas, the Oklahoma panhandle and eastern New Mexico, corresponding to a dryline located in this region (Fig. 3.1a). The east-west vertical slice through $y = 234$ km (Fig. 3.1b) shows that a vertically oriented boundary between dry and moist air is found in the lowest 1.5 km at about $x = 360$ km and becomes nearly horizontal to the east. The upward bulging moisture tongue near $x = 576$ km reflects upward motion there. To the west of the dryline, the atmosphere is well-mixed up to 500 hPa. Such a strong gradient as well as the variations in the strong gradient of water vapor may not be

properly captured by ordinary moisture observation networks, especially at levels away from the ground surface.

From the data set, the slant-path water vapor is simulated by the hypothetical GPS network using the formula

$$SWV_{ij} = \int_{i^{th}\,receiver}^{j^{th}\,satellite} q_v\,ds, \tag{3.5}$$

where SWV_{ij} is the integrated water vapor along the slant path between the ith ground-
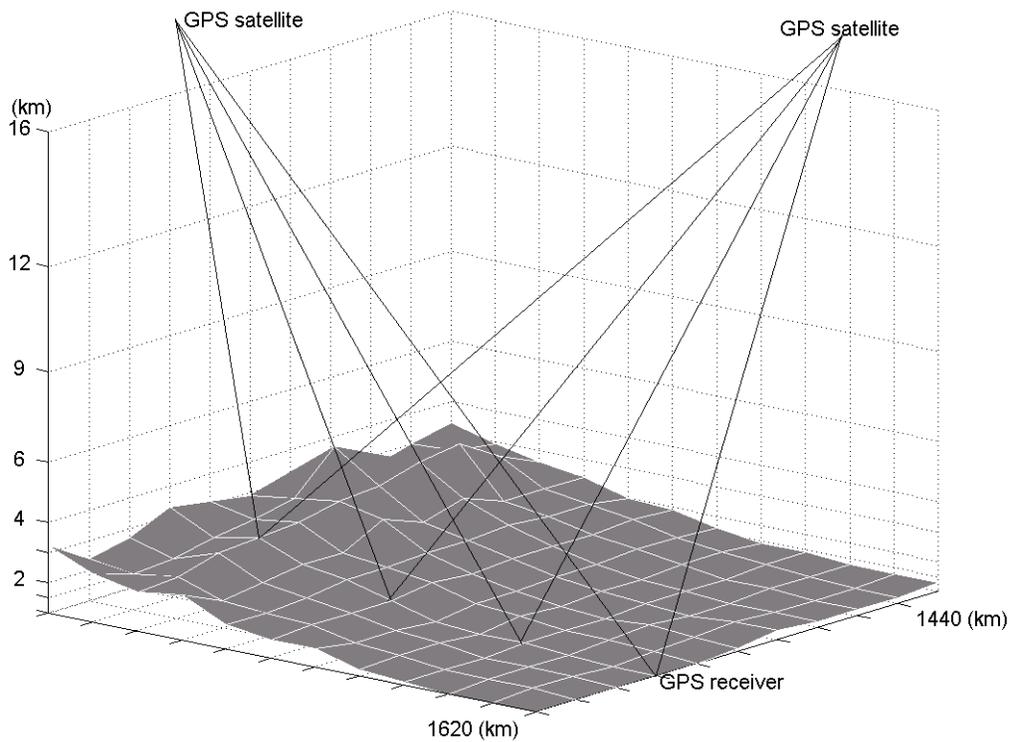
Fig. 3.2 A schematic of a ground-based GPS observation network whose data are analyzed using 3DVAR. Shaded surface represents terrain. Dark solid lines are slant paths between ground-based GPS receivers and GPS satellites. Dotted lines give a sense of the vertically stretched grid although the actual grid levels are in a terrain-following coordinate.

based receiver and the jth GPS satellite, and q_v is the specific humidity along the path elements. The value of q_v is given by a tri-linear interpolation from the eight grid points surrounding the center of the path element. No error is added to the collected *SWV* observations except in one sensitivity experiment. The hypothetical GPS network is composed of nine irregularly distributed satellites simultaneously in view, and of 132 ground-based receivers evenly distributed in the analysis domain. There is one GPS receiver station every 4 grid intervals at the surface, i.e., the horizontal spacing of receivers is 144 km. The total number of slant paths is the number of satlittes times the number of the receivers (9 × 132). Both the simulation of observational data and the data analysis are performed on the 36-km grid in ARPS terrain-following coordinate. A schematic is given in Fig. 3.2 to illustrate the GPS observation network. Surface moisture observations are available at the GPS receiver sites.

3.4 Retrieval experiments and results

3.4.1 Single surface observation tests

In order to validate our newly developed system and, more importantly, to understand the behavior of the isotropic and anisotropic spatial filters, we first perform two idealized experiments in which only a single surface moisture observation is analyzed in the whole analysis domain. The isotropic and anisotropic filters, based on Eqs. (3.3) and (3.4), respectively, are used to model the background error covariances. The single specific humidity observation with a value of 8.29 g kg^{-1} is located at the grid point marked by a black dot in Fig. 3.1, which also shows the true field at the surface used in this set of experiments. No *SWV* observation is involved so that the second term

in the cost function in Eq. (3.2) vanishes. For simplicity, only a two-dimensional horizontal filter is used so that the analyses at different levels are decoupled and the overall analysis is essentially two dimensional. In the case of an isotropic filter, a horizontal length scale of 4 grid intervals (L_r = 144 km) is used. In the anisotropic filter case, L_r has a length of 6 grid intervals (L_r = 216 km) and the length scale in error field space, L_f, is 2.0 g kg^{-1}. The larger value of L_r is used in the anisotropic filter case so that the combined effective de-correlation length scale is of sufficient length in the direction of error-field contours.

For the single observation tests, the background value is assumed constant on each model level and is equal to 12.71 g kg^{-1} at the surface. In this case, the true error field, equaling to the true field minus the background, has the same pattern as the true field itself at each level. The true error field specifies f in Eq. (3.4) for this experiment. Again we assume that the observation is much more accurate than the background, and the relative weights, proportional to the inverse of error variances, of 1, 500 and 50 are given to the background, observation and the non-negative-constraint terms of the cost function, respectively. The resultant analysis should therefore be much closer to the observation than to the background. The analysis increment fields are shown in Fig. 3.3.

The observation increment at the point of observation is spread in space through the background error covariances. Consequently, the analysis with isotropic covariances gives an analysis increment of circular shape while that with anisotropic covariances shows an increment that is related to the error field (Fig. 3.3). Since the error field in this case has the same pattern as the true specific humidity field shown in Fig. 3.1a, the analysis increment in the anisotropic case (Fig. 3.3a) is oriented in the north-northeast

to south-southwest direction and is narrower in the east-west and broader in the north-south directions compared to the circular increment of isotropic analysis. The spatial scales of the increment fields roughly match the effective de-correlation scales used in the filters. The analysis increments at the observation location are about - 4.41 g kg^{-1} in both cases, giving a total analysis of 8.30 g kg^{-1} that is, as expected, very close to the observed value.
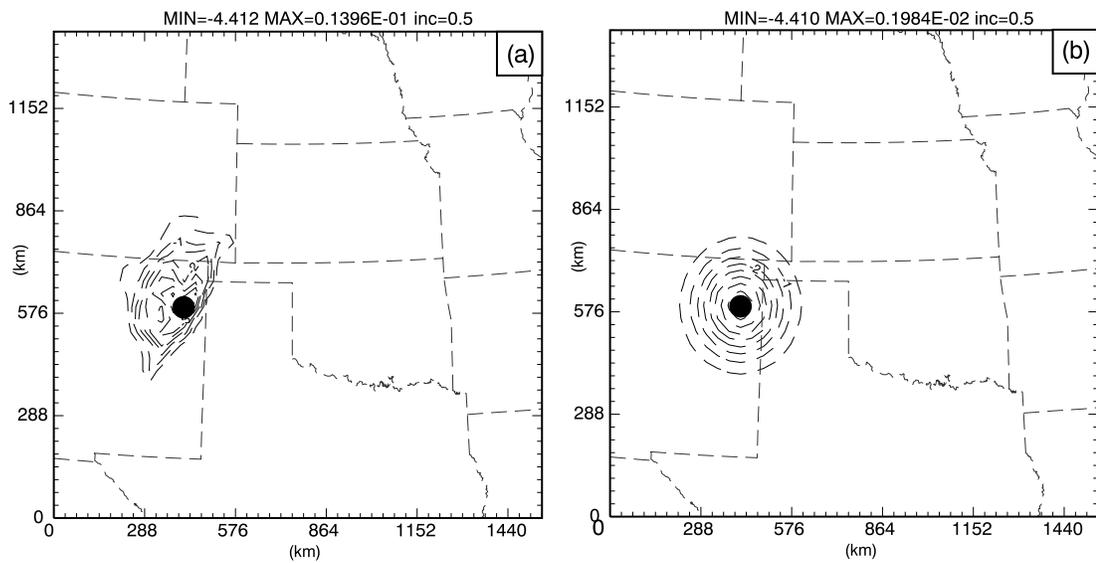
Fig. 3.3 Specific humidity increment field at the surface from single moisture observation tests, for 3DVAR analysis (a) with anisotropic flow-dependent background error covariance and (b) with isotropic covariance. The location of the single specific humidity observation at the surface is marked by the black dot. Contour interval is 0.5 g kg^{-1}.

These experiments confirm that our 3DVAR analysis system, using either isotropic or anisotropic filter, performs as expected. Hereafter in this chapter, we apply this system to the analysis of 3D moisture filed using GPS slant water vapor data as well as surface observations.

3.4.2 *SWV* retrieval experiments

A list of retrieval experiments analyzing the simulated GPS *SWV* and surface moisture observations is given in Table 3.1. The overall correlation coefficients between analysis increment for these experiments and the 'truth' increment (truth minus background) are also given in the table.
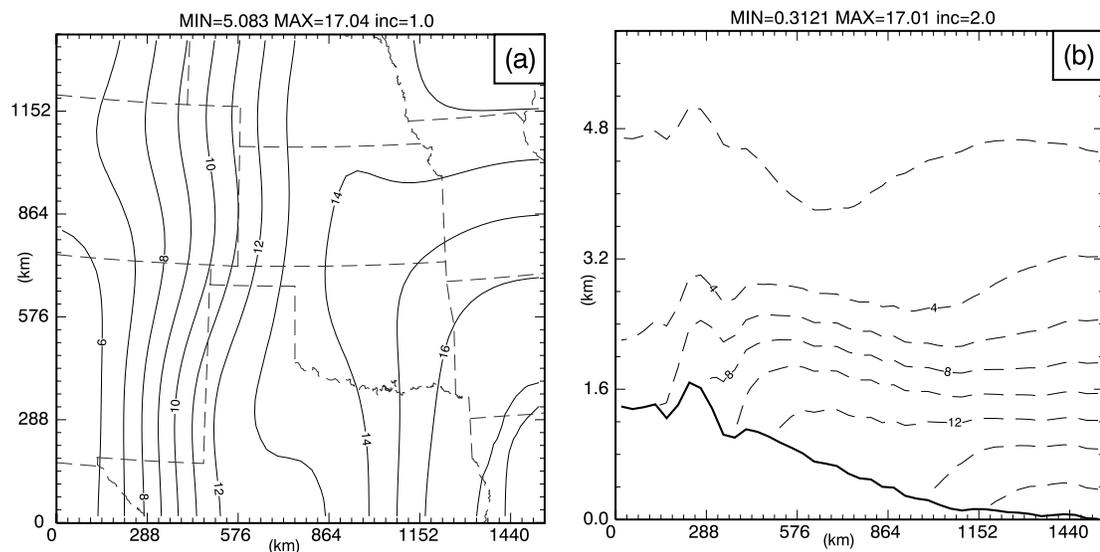
Fig. 3.4 Background specific humidity field in g kg^{-1}, obtained by smoothing 'nature' 50 times using a 9-point filter in the horizontal, (a) at the surface and (b) in the east-west vertical cross-section at y = 234 km.

First, a control experiment (CNTL) is performed. In this experiment, both *SWV* and regular surface observations at receiver sites are used. The analysis background is created by smoothing the truth 50 times, using a 2-D 9-point filter (with 1-2-1 weightings in each direction) on model levels. It can be seen from Fig. 3.4 that this background shows a general pattern of higher moisture to the east and lower values to the west but the detailed dryline structure is lost. Since both the truth and background are known, the background error can be calculated. It is therefore possible to model the

background error covariances by taking the known background error field as f in Eq. (3.4) and this is done for CNTL.

The length scale L_r used is equal to 4 grid intervals (L_r =144 km) in the horizontal and 4 layers in the vertical. L_f is given as 2.0 g kg^{-1}. Owing to the insignificant effect of filter on the far distance, cutoff radii are used and chosen to be 10 grid intervals in the horizontal and 6 layers in the vertical, respectively. The selection of filter scale depends, for one thing, on the density of ground-based GPS receivers. The relatively small filter scales and cutoff radii are chosen here so that gaps between receiver stations are filled without excessive smoothing to the analysis. The cost function defined by Eq. (3.2) is minimized with respect to the increment of specific humidity, using a conjugate gradient algorithm.

With the above parameter settings, the control experiment is conducted. Fig. 3.5 presents a vertical cross-section of retrieved moisture at $y = 234$ km from CNTL, as compared to the 'truth'. Only the domain below 6 km altitude is shown here since water vapor has very low values above 6 km. It is obvious that the retrieved moisture field matches the truth very well. The dryline near $x = 360$ km is accurately captured. There is a strong east-west moisture gradient at the low levels and the moisture isohumes are almost perpendicular to the ground near the dryline. Meanwhile, presumably due to upward motion near the dryline at near $x = 576$ km, there exists a moisture tongue at this location which is surrounded by two troughs to its east and west due to return flows. Fig. 3.6 shows the q_v increments at the surface. The retrieved increment matches almost exactly the increment of 'truth' (the difference between truth and background); their

shapes match very well and extrema locations coincide. The correlation coefficient between the two increment fields is 0.926 on the entire grid (Table 3.1).
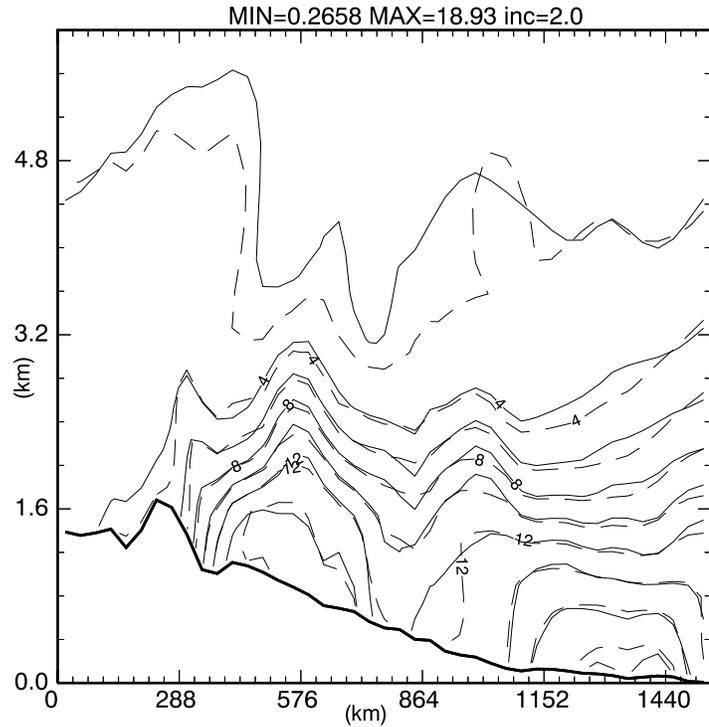
Fig. 3.5 East-west vertical cross-section of specific humidity field (g kg^{-1}) at y = 234 km. The solid lines are for 'nature' and the dashed lines are for CNTL.

To see the performance when an isotropic filter is used instead, another experiment is conducted, in which the background is based on the Smoothed 'truth' with No Flow-dependent background error (SNF, Table 3.1). The length scale for an isotropic filter should be smaller, so L_r is given a length of 3 grid intervals. SNF is otherwise the same as CNTL. Fig. 3.7 shows the vertical cross-section at y = 234 km and the analysis increment at the surface from SNF. The retrieved moisture field also exhibits a dryline around x=360 km, a moisture tongue due to updraft together with troughs on its sides due to downdrafts (Fig. 3.7a). The implied strengths of the updrafts

49
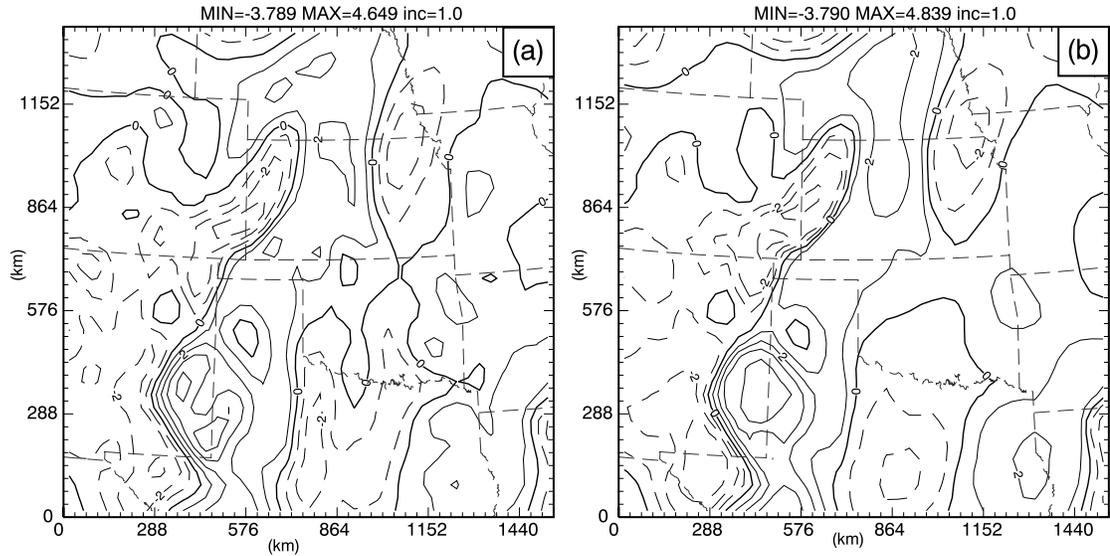
Fig. 3.6 Specific humidity increment field in g kg^{-1} at the surface (a) from 'nature' and (b) from CNTL. Dashed lines represent negative values and solid lines positive values.

and downdrafts as reflected by the isohume shapes are weaker than those in CNTL and the truth. Their locations near the ground are shifted eastwards relative to the 'truth'. The isohumes have shapes different from the 'truth' and are smoother than 'truth' (Fig. 3.7b). Overall, this analysis does not match the 'truth' as well as the analysis of CNTL. The overall correlation coefficient of the increment fields is reduced to 0.83 from the 0.926 of CNTL (Table 3.1).

Experiment CNTL has a flow-dependent background error covariances based on known background error while experiment SNF assumes isotropic covariances. Their comparison illustrates the importance of background error covariances. The problem is, however, that the background error covariances are never known exactly. In order to improve analyses in actual NWP, it is necessary to seek feasible methods for representing the background error covariances as accurately as possible. Using an isotropic filter, we can obtain an analysis (the result of SNF) that is much closer to the
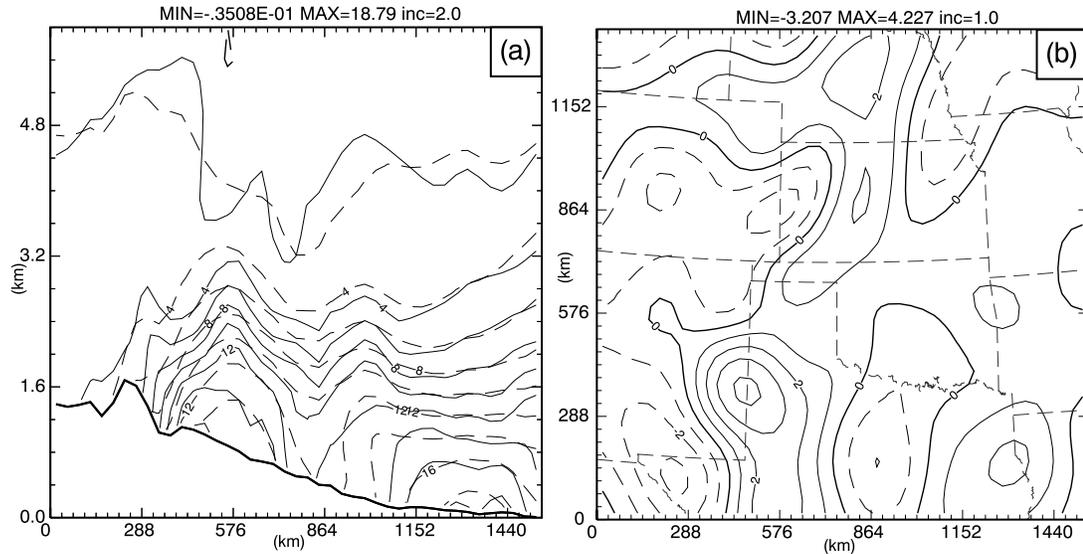
Fig. 3.7 (a) East-west vertical cross-section of specific humidity field (g kg^{-1}) at y = 234 km where solid lines are for 'nature' and dashed lines for experiment SNF. (b) Analysis increment of specific humidity (g kg^{-1}) at the surface from experiment SNF, where dashed lines are for negative values and solid line for positive values.

'truth' than the initial background field. As a result, the background error may be estimated by subtracting the background from the isotropic analysis, which we call the updated (from that based on initial background) background error. Based on this consideration, the experiment with Smoothed 'truth' as the background and the Updated Flow-dependent background error covariances (SUF) is performed (see Table 3.1), which does a second analysis starting from the same background but using an anisotropic filter based on the error field calculated as the difference between the output of SNF and the background. This analysis matches the 'truth' much better than that of SNF as shown in Fig. 3.8, and the improvement is also, though to a lesser extent, reflected in the overall correlation coefficient (0.832 versus 0.830, Table 3.1). In the vertical cross-section (Fig. 3.8a), the isohumes for specific humidity values of 4, 6 and 8 g kg^{-1} follow the 'truth' much better than those in Fig. 3.7a. The fine-scale moisture

bulge near $x = 360$ km is also well recovered. Meanwhile, the maximum value of 18.65 g kg^{-1} from SUF is closer to the true value of 18.64 g kg^{-1} than the 18.79 g kg^{-1} of SNF. The surface increment field (Fig. 3.8b) contains a lot more finer-scale structures that are consistent with the pattern of 'truth' increment field.
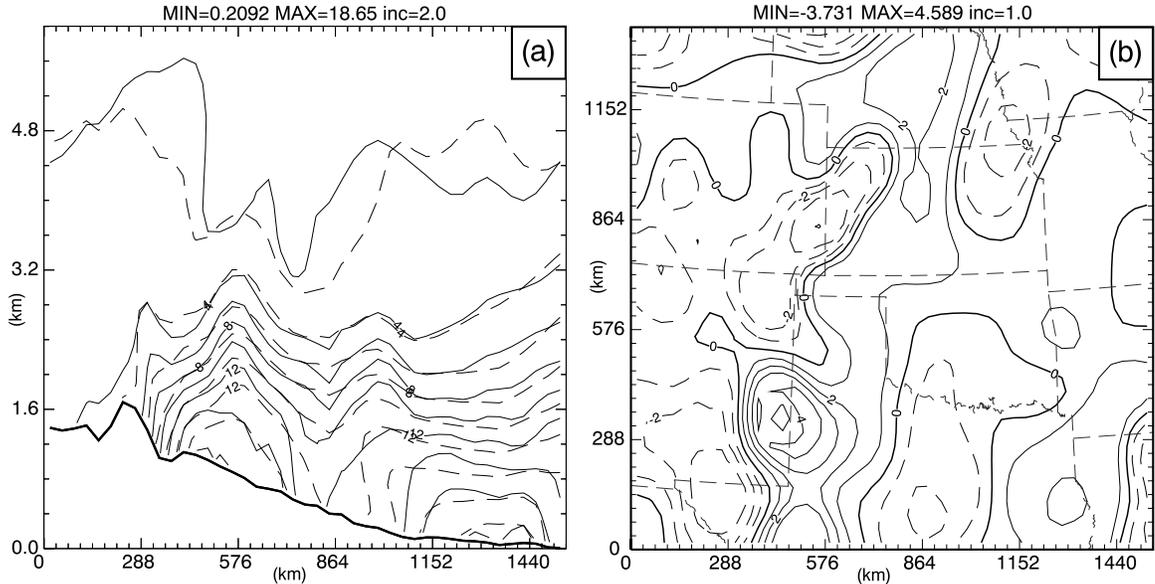
Fig. 3.8 Same as in Fig. 7 but for experiment SUF.

These three experiments clearly demonstrate that the 3DVAR system with flow-dependent background error covariances realized through an anisotropic spatial filer provides better analysis than that with isotropic covariances. This is true even when the background error is estimated using a first-pass analysis that utilizes isotropic error covariances.

3.4.3 Retrievals with a vertically logarithmic background

The background in the above three experiments was constructed by smoothing the 'truth'. This background, shown in Fig. 3.4, still contains structures of moisture at

the larger scales and some information on the vertical moisture distribution. To understand how much the analysis depends on the structure information present in the background, we conduct another two experiments in which the background is specified using a logarithmic vertical profile. This profile decreases from a value of 12 g kg^{-1} at the surface to zero at 17 km, the top of the analysis domain. This profile is used to specify the background q_v values on each terrain-following grid level, so that the background is uniform along the model levels. Such a background is artificial and supplies no realistic information on the structure of moisture, therefore a successful analysis has to extract all structure information from the observations with the help of background error covariances. For these tests, the weight of background term is reduced from 1.0 to 0.2 because of the reduced accuracy of the background.

One experiment using the isotropic filter [i.e., the logarithmic background with no-flow-dependent B (LNF)] and another using the anisotropic filter [i.e., the logarithmic background and truth-based flow-dependent B (LTF)], which is based on the true error field, are performed. The vertical cross-sections of retrieved moisture field for these two experiments are presented in Fig. 3.9 and Fig. 3.10, respectively. For the isotropic filter case (Fig. 3.9), the dryline is weaker and the boundary separating the moist and dry air shows a significant slope at the low levels. The structure is, incorrectly, more symmetric in the east-west direction in accord with the isotropy and the moist bulge near $x = 288$ km is completely missed in the analysis (Fig. 3.9). However, the vertical structure of the analysis using flow-dependent background error is much better than that using isotropic error, as expected. For the anisotropic case, the isohumes generally follow the 'true' isohumes except near the boundaries. The dryline

Experiment	background	Flow-dependent background error?	Obs used	Obs error	Obs resolution	Filter	Correlation coefficient
CNTL or STF	smoothed truth	Yes, based on true background error	*SWV*+sfc	no	1 obs / 4 grid intervals	3D	0.926
SNF	smoothed truth	No	*SWV*+sfc	no	same as above	3D	0.830
SUF	smoothed truth	Yes, on updated analysis	*SWV*+sfc	no	same as above	3D	0.832
LTF	logarithmic	Yes, on true background error	*SWV*+sfc	no	same as above	3D	0.827
LNF	logarithmic	No	*SWV*+sfc	no	same as above	3D	0.821
STFNSFC	smoothed truth	Yes, on true background error	*SWV*	no	same as above	3D	0.894
SNFNSFC	smoothed truth	No	*SWV*	no	same as above	3D	0.668
STFNVF	smoothed truth	Yes, on true background error	*SWV*+sfc	no	same as above	2D	0.801
STF_ER	smoothed truth	Yes, on true background error	*SWV*+sfc	yes	same as above	3D	0.790
SNF_LR	smoothed truth	No	*SWV*+sfc	no	1 obs / 8 grid intervals	3D	0.679
STF_LR	smoothed truth	Yes, on true background error	*SWV*+sfc	no	1 obs / 8 grid intervals	3D	0.870

Table 3.1 List of moisture retrieval experiments. In the table, *SWV* denotes the GPS slant-path water vapor observation data and 'sfc' is for the surface moisture observation data.

is reflected by the almost vertically oriented boundary between the dry and moist air in the lowest 1.5 km. But there are more errors near the east and west boundaries in Fig. 3.10 (for LTF) than in Fig. 3.5 (for CNTL). This can be explained by the fact that, with the logarithmic background, the recovery of 3D moisture structure depends more on the GPS slant-path water vapor observations but there are fewer slant paths near the boundaries because there is no path coming in from outside the boundary (this problem will not exist for global analyses).
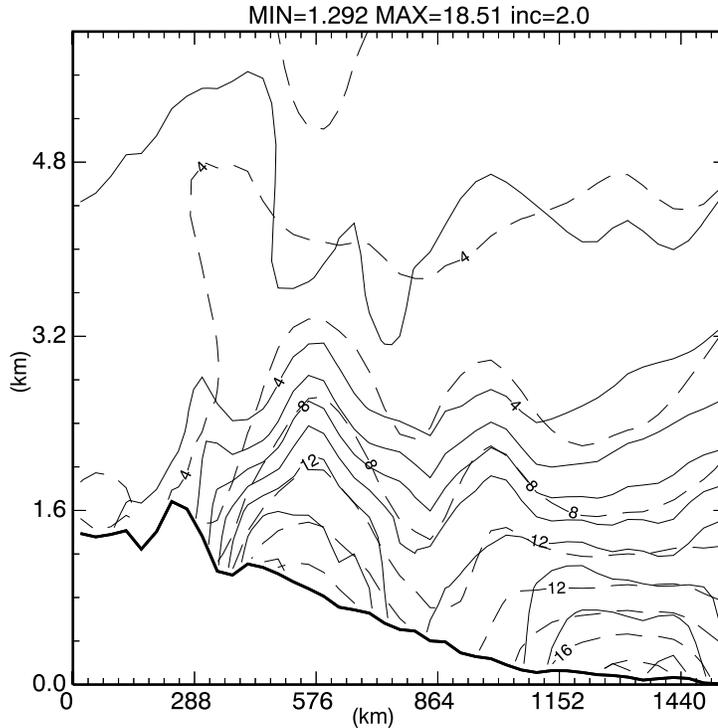
Fig. 3.9 Same as in Fig. 3.5 but dashed lines are from experiment LNF.

As we have previously explained, the inclusion of the background term in the 3DVAR analysis eliminates the under-determinedness problem. It has been found that even with a background that is worse than the logarithmic one tested above, such as the case of a constant value applied to 3D, a convergent 3DVAR analysis is still feasible although the analysis is poorer (results not shown). On the contrary, the minimization fails (an unphysical analysis was produced before any convergence could be reached) when the background term is excluded and when no additional smoothing constraint is applied.

The above experiments show that our 3DVAR system is capable of recovering the 3D moisture structure from ground-based GPS slant-path water vapor and surface moisture observations even when an artificial analysis background is used. When flow-

dependent background error information is known and properly used, the analysis is improved.
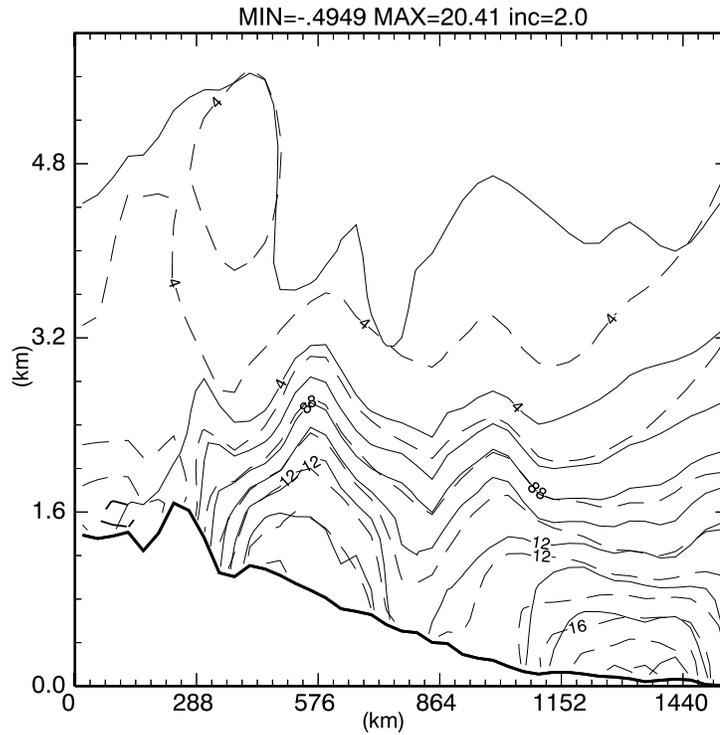
Fig. 3.10 Same as in Fig. 3.5 but dashed lines are from experiment LTF.

3.5 Sensitivity experiments

In this section, sensitivity experiments are performed to test several factors that can affect the quality of moisture analysis.

3.5.1 Impact of surface moisture observations

A sensitivity experiment with smoothed background and truth-based flow-dependent error covariances, as in CNTL, plus no surface observations (STFNSFC), is conducted which is the same as CNTL except that surface observations are excluded.

This is to test the effect of surface moisture observations on the retrieval. The overall correlation coefficient between the increment fields of this retrieval and that of 'truth' is now 0.894, a quite significant decrease from the 0.926 of CNTL (Table 3.1).
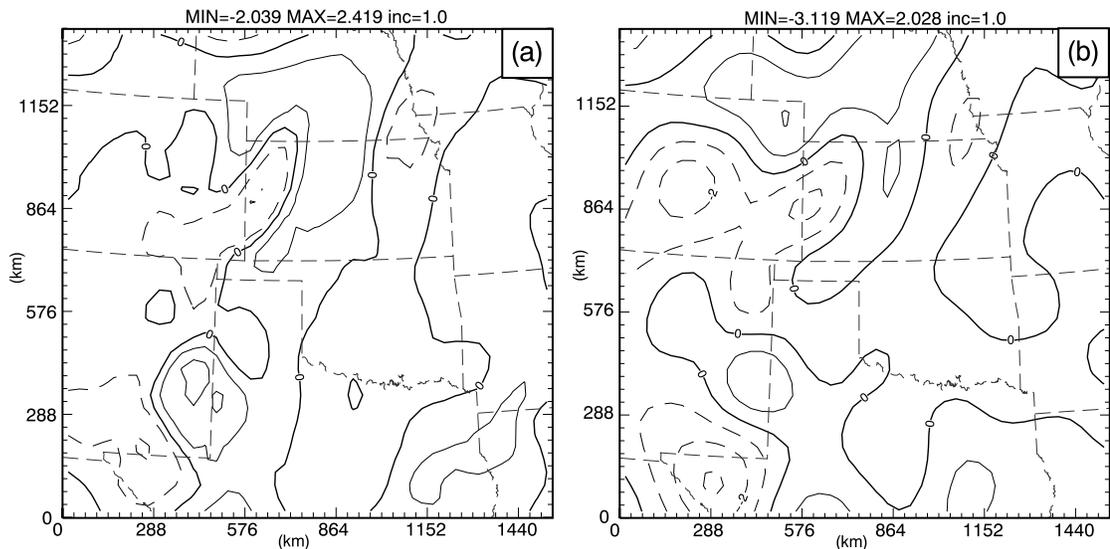
Fig. 3.11 Same as in Fig. 3.6 but (a) is for experiment STFNSFC (b) is for experiment SNFNSFC.

The surface increment field from this experiment is presented in the Fig. 3.11a. The pattern of the increment field is good, but the extrema are only half as large as those from CNTL (Fig. 3.6). Due to the integral nature of the *SWV* observations, the deterioration in accuracy of surface analysis will also worsen the analysis at the upper levels. This is shown by Fig. 3.12, which shows the correlation coefficients between the retrieval and 'truth' increment fields plotted against the vertical model layers[2]. It is seen that, below the 5th model level (about 500 meters AGL), the correlation coefficients

---

[2] The mean heights of the center of the model levels are 0.80, 0.89, 0.98, 1.12, 1.29, 1.50, 1.73, 2.00, 2.28, 2.58, 2.90, 3.24, 3.58, 3.94, 4.30, 4.66, 5.04, 5.41, 5.79, 6.16, 6.54, 6.92, 7.30, 7.67, 8.05, 8.43, 8.81, 9.20, 9.59, 9.98, 10.38, 10.79, 11.21, 11.65, 12.10, 12.57, 13.07, 13.59, 14.14, 14.72, 15.34, 16.00, and 16.66 km.

from experiment STFNSFC are always less than those from CNTL. At the upper levels, the correlation coefficients of STFNSFC are mostly smaller than those of CNTL. Clearly, the surface moisture observations improve the overall analysis by directly adjusting near-surface q_v field and by more accurately distributing water vapor in the vertical.

Another experiment, SNFNSFC (SNF plus No SurFaCe observations), is the same as SNF (Table 3.1) except that surface observations are excluded. The results show that the analyzed dryline is much weaker compared to the corresponding retrieval with surface observations, i.e., that of SNF. The increment field at the surface (Fig. 3.11b) does not match well the 'true' increment field (Fig. 3.6a) and the extrema are even weaker than in STFNSFC (Fig. 3.11a).

The overall correlation coefficient is 0.67 for SNFNSFC, about 0.26 and 0.22 less than those of CNTL and STFNSFC, respectively. The large drop in accuracy is mostly due to the differences at the lowest levels where the surface observations have the greatest impact. This is so partly because, near the surface, the model meshes are intersected by very few or no slant paths. Limited by the relatively small analysis domain, the lowest elevation angle of usable slant paths in our experiments is about 15 degrees. The inaccuracy in the surface moisture analysis influences the analysis at upper levels because of the integral nature of GPS observations. It is worth being pointed out that there is no much information above the 21st model level which is approximately 6.5 km in mean height.
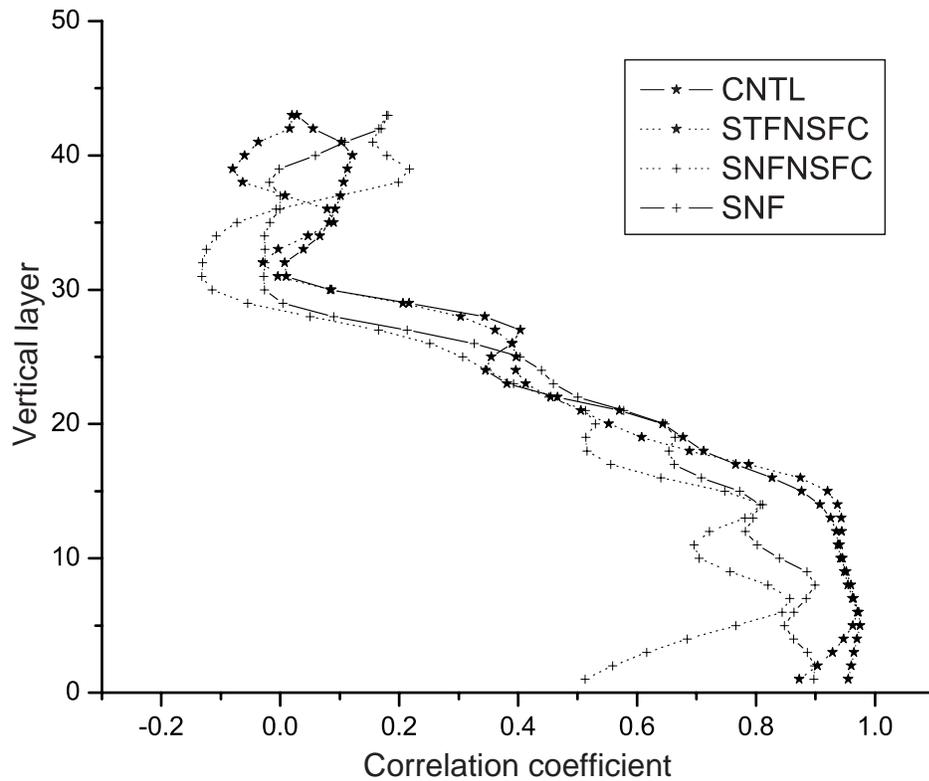
Fig. 3.12 Profiles of correlation coefficient of specific humidity increment (difference from background, in g kg-1) between those of 'nature' and 3DVAR analysis from experiments CNTL, STFNSFC, SNFNSFC, and SNF, plotted for different model levels. Mean height of each level is given in a footnote in this chapter.

The above comparisons of analyses tell us that the surface observations play an important role, especially when realistic flow-dependent background error covariances are not available. Flow-dependent background error covariances, consequently, have more impact on the analysis in the absence of surface observations. The best retrieval is obtained when both accurate background error covariance information and surface observations are included while the worst is obtained when neither is.

3.5.2 Impact of vertical filtering

To isolate the effect of vertical filtering, only horizontal filter is used in experiment STFNVF (Table 3.1), i.e., STF or CNTL plus no vertical filtering. All other parameter settings are the same as in CNTL. Fig. 3.13 shows the vertical profiles of correlation coefficients of analysis increment from CNTL and STFNVF with the 'truth' increment. It is clear that CNTL gives a better analysis than STFNVF. There is almost no difference right at the surface owing to the dominant contributions of surface observations there but the correlation coefficient of STFNVF is significantly lower between the 2nd and 5th levels, with the difference being larger than 0.3 at the 2nd level. Still, the correlation coefficients from the 3rd through 13th level are larger than or equal to 0.8, so the pattern of analysis increment remains reasonably good at those levels. The gradient of the low-level analysis increment is, however, clearly weaker than that of the 'truth' increment (not shown). Fig. 3.13 also shows a general improvement in the analysis at the upper levels when vertical filtering is included. Therefore, the vertical filtering is very important for accurate analysis in the boundary layer and beneficial at the upper levels too. It is so because, in the absence of vertical filtering, surface observation information cannot be spread upward into the boundary-layer where information from GPS data is sparse.

3.5.3 Sensitivity to observation error

One of the advantages of using simulated data is that observation data can be specified as error free, but the sensitivity to observation errors should be examined for practical use. This is done in experiment STF_ER ('ER' for error), in which normally

distributed errors with 5% and 7% standard deviations are added to the simulated

surface and *SWV* observations, respectively. The experiment is otherwise the same as

CNTL. The errors are consistent with the estimate of Braun et al. (2001) for real data.

Compared to CNTL, the relative weights for *SWV* and regular surface observation terms

are decreased to 80 from 100 and 400 from 500, respectively, because of the added

observational errors.
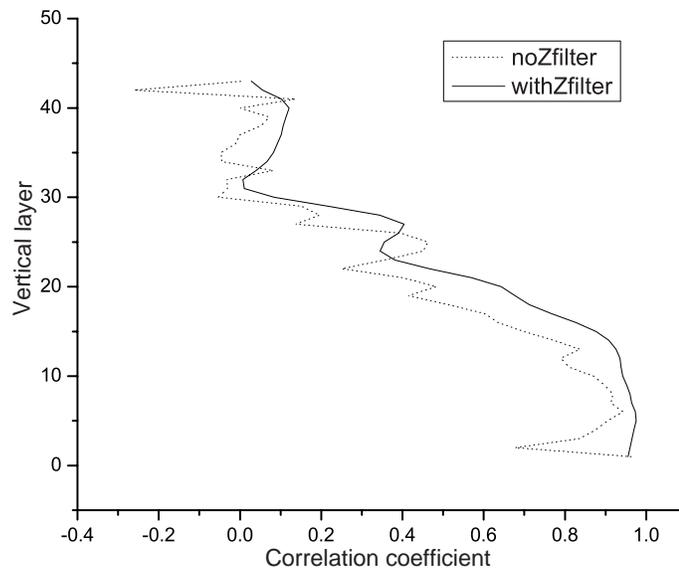
Fig. 3.13 Same as in Fig. 3.12 but for experiments CNTL (solid line) and STFNVF
(dotted line).

The analysis of STF_ER also matches the 'truth' reasonably well, as shown in

Fig. 3.14. In the vertical cross section, only the 2 g kg^{-1} isohume is prominently

different from the CNTL result. The analyzed maximum is 19.49 g kg^{-1}, 0.75 g kg^{-1}

larger than the 'truth' maximum of 18.64 g kg^{-1}. The horizontal structure (not shown)

also matches 'truth' well below 7 km where 95% of water vapor concentrates.

Therefore, even in the presence of realistic errors in the *SWV* and surface observations,

our 3DVAR system is still able to produce good analysis, although the overall correlation coefficient of the increments decreases from 0.926 to 0.79 (Table 3.1). Still, all major structures of the dryline are recovered well.

MIN=0.1727 MAX=19.49 inc=2.0
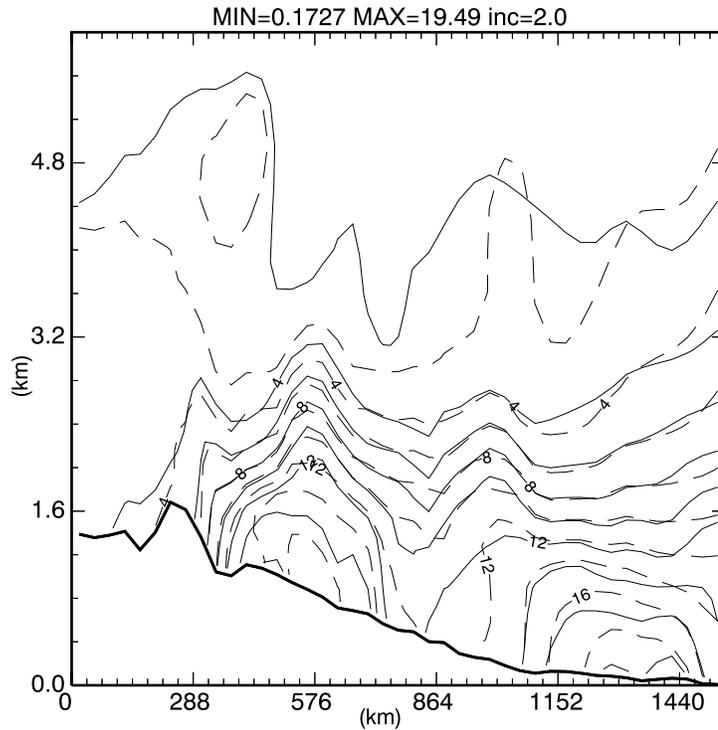
Fig. 3.14 Same as in Fig. 3.5 but dashed lines are for experiment STF_ER.

3.5.4 Observation density test

Finally, the sensitivity of 3D moisture analysis to the density of ground-based GPS receivers is examined. The receiver density is halved in experiments SNF_LR and STF_LR (LR for Low Resolution), with one receiver station every 8 grid intervals and a station spacing of 288 km. The total number of observations is 360. The horizontal de-correlation length scale in physical space, L_r, and the corresponding cutoff radius are

62

enlarged since their choices should be partly related to receiver network density. The length scale should be large enough to fill the gaps between receiver stations. Experiment SNF_LR uses an isotropic filter with L_r given a length of 5 grid intervals, while experiment STF_LR uses an anisotropic filter and a 6-grid-interval physical length scale. L_f remains 2.0 g kg^{-1}. SNF_LR and STF_LR should be compared with the high-resolution counterparts SNF and CNTL, respectively.
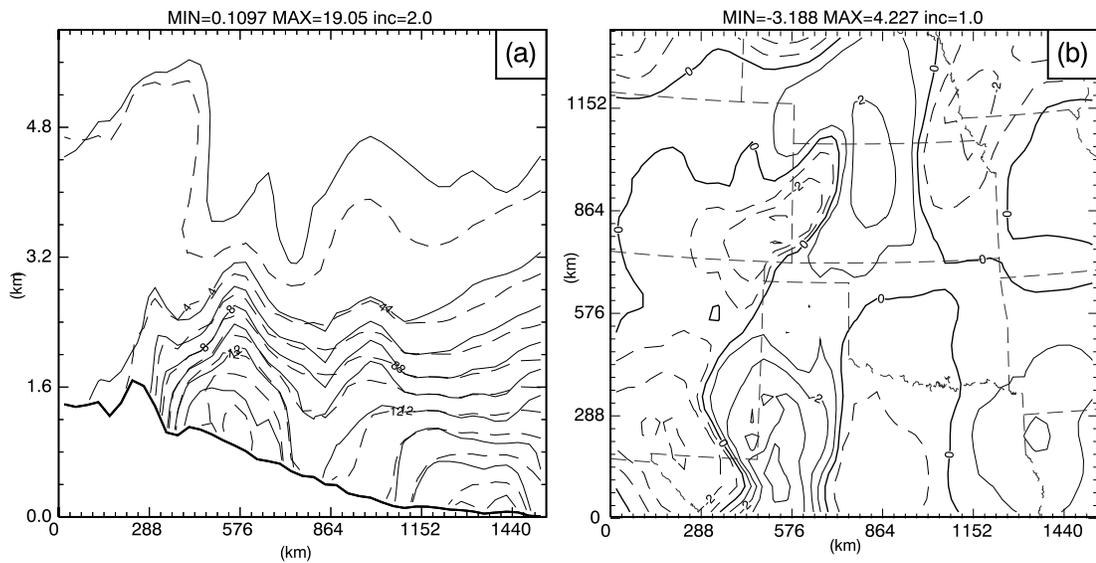
Fig. 3.15 Same as in Fig. 3.7 but for experiment STF_LR.

Fig. 3.15 presents the retrieval result from STF_LR. Comparing the east-west cross-section at $y = 234$ km (Fig. 3.15a) with that of CNTL (Fig. 3.5), we can see that the difference in the quality of analysis is relatively small, indicating that the 3D moisture retrieval is not very sensitive to the observation density, in this case when reliable statistics of the background error are available and used. This conclusion is also supported by the surface analysis increment field in Fig. 3.15b. The overall correlation

coefficient is about 0.87 for STF_LR, 0.06 less than that of CNTL (Table 3.1). When the background error covariances are given an isotropic form in SNF_LR, the overall correlation coefficient decreases to 0.68 from 0.83, that of the corresponding high density case (SNF). Clearly, this decrease is much larger than the flow-dependent error cases (CNTL and STF_LR). This implies that the retrieval quality is more sensitive to receiver station density when no good information on the background error structure is available or used.

3.6 Summary and discussion

A new 3DVAR analysis system is developed for retrieving the 3D water vapor structure of the atmosphere from a GPS observation network. This network provides integrated water vapor along slant paths between GPS satellites and ground-based receivers, as well as direct moisture measurements at the ground receiver sites. The ARPS mesoscale model is used to create a 'true' atmospheric moisture field for a dryline case that occurred during the IHOP_2002 field experiment, and this 'true' atmosphere is sampled by the GPS observation network to produce simulated slant-path water vapor data and surface moisture observations.

Our analysis system is formulated in the same generalized terrain-following coordinate system used by ARPS. It includes a background term in the 3DVAR cost function, which for one thing overcomes the under-determinedness problem with GPS data retrieval. Three dimensional Gaussian-type explicit spatial filters are used to model background error covariances which can be isotropic or flow-dependent and spatially anisotropic. In the latter case, a flow-dependent anisotropic filter is constructed based

on the true or estimated error field of the analysis background, following the approach of Riishøjgaard (1998). Three-dimensional variational retrieval experiments are conducted using the simulated data and the quality of the analyses is evaluated through comparisons with the truth. The results are summarized as follows:

1) The 3DVAR system, even with isotropic background error covariances, can retrieve from surface moisture and GPS *SWV* observations the 3D mesoscale moisture structure reasonably well, and the analysis is able to capture major features of the model simulated dryline.

2) The use of flow-dependent background error covariances realized through an anisotropic spatial filter always improves the analysis. The best analysis is obtained in the ideal situation where the background error structure is known. Otherwise, the background error structure can be estimated from a first-pass analysis obtained using isotropic background error covariances, and in this case, a significant improvement in the analysis can also be obtained. The role of flow-dependent covariances is enhanced at regions near the lateral boundaries and at the low levels, where the model grid cells are intersected by few if any slant paths. In these data sparse regions, the retrieval benefits more from the properly spread observation increments via background error covariances.

3) The retrieval is still feasible even with an artificial vertically logarithmic background that is homogeneous along the model levels when flow-dependent background error covariance is applied. The quality of analysis is not as good as the smoothed background case but still reasonable except for regions near the boundaries where few slant paths go through. This suggests that our 3DVAR method is rather robust,

and the analysis derives most of the water vapor structure information from the observations and the background error statistics.

4) Sensitivity experiments indicate that surface moisture observations are important for accurate analysis of water vapor at low levels, and more so when no good information on the background error covariances is available or used. When there is no surface observation, flow-dependent background error has even larger positive impact on the analysis. The vertical component of the spatial filter is shown to be very beneficial, especially in the low-level data-sparse region, where its main effect is in the upward spread of surface moisture information. Improved low-level moisture analysis also leads to better upper-level analysis through an improved vertical distribution of moisture.

5) Sensitivity tests on the observation errors show that our analysis system is also robust in the presence of realistic errors in the surface moisture and *SWV* observations. Main structures of the dryline can still be recovered with reasonable accuracy. With the density of ground-based receiver stations halved, the dryline structure can be reasonably recovered when flow-dependent background error covariances are used but it increases the problems noted near the boundaries. Such deterioration is more dramatic when an isotropic spatial filter is used. In other words, the positive impact of flow-dependent background error covariances increases when the density of ground-based GPS receiver stations decreases.

In our current analysis system, an explicit spatial filter is used to model the background error covariances as well as to reduce computer memory requirements as compared to storing the full **B** matrix. This treatment cannot guarantee the positive

definiteness of the modified covariance matrix, however. Meanwhile, the larger cutoff radii are, the more expensive the algorithm becomes. A computationally more efficient alternative is the recursive filter, which can be used to model both isotropic and anisotropic background error (Wu et al. 2002; Purser et al. 2003a, b), although the realization of the latter with recursive filter is much more complicated. In next chapter, the recursive filters are implemented and tested in this 3DVAR system.

Chapter 4
Retrieval of Moisture from Simulated GPS Slant-path Water Vapor Observations using 3DVAR with Anisotropic Recursive Filters[3]

4.1 Introduction

In Chapter 3, a 3DVAR analysis system is developed that models the flow-dependent background error field using an explicit spatial filter. Better moisture analysis from simulated GPS slant-path water vapor data and surface moisture data is obtained when using an anisotropic spatial filter to model the flow-dependent background error covariance. The explicit anisotropic filter, when applied over even a moderate number of grid points in three dimensions, is, however, too expensive in terms of both computational and memory storage costs, because of the need to calculate and store filter coefficients locally and apply the filter explicitly at every grid point, in all three directions. A much more computationally efficient algorithm is the implicit recursive filter because the recursive filters are typically applied only once or a few times (in the case of multiple filter passes) in each filtering direction while the explicit

---

filter is applied once at every grid point (see also Purser et al. 2003a for more completed discussion). For example, The univariate 3DVAR analyses in Chapter 3, using the explicit anisotropic filters with $L_r = 4$ grid intervals and $L_f = 2.0$ g kg^{-1} together with the cutoff radii of 10 grid intervals in the horizontal and 6 coordinate layers in the vertical, typically require about 160 minutes of CPU time to perform 100 minimization iterations while it takes the recursive filter only about 4 minutes to do the same, using a single 1.1 GHz IBM Power 4 (Regatta p690) processor. The recursive filter with flow-dependent anisotropic version, though much more complex than the isotropic version, has seen significant development recently (Purser et al. 2003b). The significantly increased efficiency using recursive filters makes their implementation in operational data assimilation systems practical (also refer to section 2.1.3.2).

In this chapter, the recursive filter with an anisotropic option is implemented in our 3DVAR system. Some retrieval experiments of GPS slant-path water vapor data are performed and the results are compared with those of explicit filters reported in Chapter 3. We also examine the impact of flow-dependent background errors realized through anisotropic recursive filters on the quality of 3DVAR analysis. Further, the sensitivity of isotropic and anisotropic recursive-filter analyses to the spatial de-correlation scales is also examined systematically. We point out here that even though the experiments performed in this chapter are similar to those presented in Chapter 3, the implementation of anisotropic recursive filters for the modeling of truly flow-dependent background error structures represents significant progress. The use of experiments with very similar configurations as those in Chapter 3 facilitates direct comparisons with the results of explicit filters.

The rest of this chapter is organized as follows. Section 4.2 describes our 3DVAR system with recursive filter and gives special attention to the procedure for determining the aspect tensor (the definition of aspect tensor is in section 2.1.3.2.3), especially for the anisotropic case, given the modeled background error covariances. Section 4.3 illustrates the effect of recursive filters on the analyses with single observation tests. The 3DVAR system with recursive filter is applied to the full 3D moisture retrieval in section 4.4. In section 4.5, we check the effect of filter length scales on the analysis quality and the sensitivity of the analysis to observational errors. Conclusions are given in section 4.6, together with suggested future work.

4.2 3DVAR system with recursive filters

4.2.1 Modified 3DVAR equations

We present in this section the 3DVAR analysis system developed and used in this chapter. It is based on the 3DVAR system developed in Chapter 3. The cost function is the same as it in Eq. (3.1) with its individual terms explained in Eqs. (3.1a-d). But there are some differences between this 3DVAR system and that in Chapter 3. First of all, this system uses a preconditioner that involves the square root $\mathbf{D}$ (see Eq. (2.19)) of the background error covariance matrix, $\mathbf{B}$, instead of $\mathbf{B}$ itself as in Chapter 3. As a result, the control variables of the current incremental 3DVAR system are different from those used in Chapter 3. The control variable for this system is set in Eq. (2.18). Further, it uses a recursive filter instead of an explicit spatial filter to model the square root of background error covariance.

The control variable $\mathbf{v}$ is rewritten here as follows,

$$\delta \mathbf{x} = \mathbf{Dv} \, , \tag{4.1}$$

where $\delta \mathbf{x} \equiv \mathbf{x} - \mathbf{x}_b$ is the increment of $\mathbf{x}$, and $\mathbf{D}$ is defined as $\mathbf{DD}^T = \mathbf{B}$. After utilizing weighting coefficients W_{swv} and W_{sfc} to simplify the roles of observation error covariances $\mathbf{R}_{swv}$ and $\mathbf{R}_{sfc}$, the cost function J, in Eq. (3.1) together with Eqs. (3.1a-d) can then be combined to formulate the cost function specifically with respect to the new control variable $\mathbf{v}$,

$$
\begin{aligned}
J(\mathbf{v}) = \frac{1}{2}\mathbf{v}^T\mathbf{v} + \frac{1}{2}\big[H_{swv}\left(\mathbf{x}_b + \mathbf{Dv}\right) - \mathbf{SWV} \big]^T W_{swv} \big[H_{swv}\left(\mathbf{x}_b + \mathbf{Dv}\right) - \mathbf{SWV} \big] \\
+ \frac{1}{2}\big[H_{sfc}\left(\mathbf{x}_b + \mathbf{Dv}\right) - \mathbf{q}_{v_{sfc}} \big]^T W_{sfc}\big[H_{sfc}\left(\mathbf{x}_b + \mathbf{Dv}\right) - \mathbf{q}_{v_{sfc}} \big] \\
+ \frac{1}{2}\left[\frac{\mathbf{x}_b + \mathbf{Dv} - |\mathbf{x}_b + \mathbf{Dv}|}{2} \right]^T W_c \left[\frac{\mathbf{x}_b + \mathbf{Dv} - |\mathbf{x}_b + \mathbf{Dv}|}{2} \right].
\end{aligned}
\tag{4.2}
$$

The operational implementation of this minimization method requires that the gradient of the cost function $J(\mathbf{v})$ be evaluated with respect to the control variable $\mathbf{v}$. The gradient $\nabla_{\mathbf{v}}J$ is given by differentiating Eq. (4.2) with respect to $\mathbf{v}$ as follows,

$$
\begin{aligned}
\nabla_{\mathbf{v}}J = \mathbf{v} + \mathbf{D}^T \mathbf{H}_{swv}{}^T \mathbf{R}_{swv}^{-1}\left(\mathbf{H}_{swv}\mathbf{Dv} - \mathbf{d}_{swv} \right) \\
+ \mathbf{D}^T \mathbf{H}_{sfc}{}^T \mathbf{R}_{sfc}^{-1}\left(\mathbf{H}_{sfc}\mathbf{Dv} - \mathbf{d}_{sfc} \right) + \nabla_{\mathbf{v}}J_c,
\end{aligned}
\tag{4.3}
$$

where $\mathbf{H}_{swv}$ and $\mathbf{H}_{sfc}$ are the linearized perturbation operators of the observation operator H_{swv} and H_{sfc}; $\mathbf{d}_{swv}$ and $\mathbf{d}_{sfc}$ are the innovation vectors of SWV and surface moisture observations which are given respectively as follows,

$$
\begin{aligned}
\mathbf{d}_{swv} = \mathbf{SWV} - H_{swv}\left(\mathbf{x}_b\right) \\
\mathbf{d}_{sfc} = \mathbf{q}_{v_{sfc}} - H_{sfc}\left(\mathbf{x}_b\right);
\end{aligned}
\tag{4.4}
$$

and $\nabla_{\mathbf{v}}J_c$ is given by $\nabla_{\mathbf{v}}J_c = W_c\mathbf{D}^T\left(\mathbf{x}_b + \mathbf{Dv}\right)$ only applied when the moisture analysis is negative. In all retrieval experiments we depict later the recursive filter models the

matrix **D** and is applied to control variable **v**. No explicit background error covariance matrix is involved in the calculation of the cost function and its gradient.

As discussed earlier, the background error covariance controls the extent to which the analysis at the grid points some distance from an observation is influenced by the observation innovation. Again, we use both isotropic and anisotropic background error covariance in the 3DVAR system to retrieve 3D water vapor and compare their analyses to gain knowledge of the effect of anisotropic error covariance on retrieval results. We also compare and contrast their analyses with those using explicit filters in Chapter 3.

The isotropic and anisotropic background error covariances are respectively defined in Eqs. (3.3) and (3.4). It is valuable to emphasize here that the Eq. (3.4) formulates a covariance function which is positive definite according to the definition 2.2 in Gaspari and Cohn (1999) and Schur product theorem (cf. Horn and Johnson 1985, p.458). The use of recursive filter can maintain the positive definite property of the background error covariance while the use of explicit filter in Chapter 3 cannot. Further, Eq. (3.4) is based on the idea of Riishøjgaard (1998) with an important difference. In his work, it is suggested that the analysis background field be used as the f, under the assumption that the error field has a similar pattern as the background field. This may be true for certain quasi-conservative quantities that are advected by the flow, but not necessarily true for all fields. In our case, f, is defined as the error field. To estimate the f field, one possibility is to first perform an isotropic analysis then use the difference between this 'trial' analysis and the background as an estimate of the error field.

4.2.2 Derivation of 'aspect tensor'

The implementation of recursive filter is very simple in the case that the background error covariance is isotropic. While it is much more complicated for anisotropic error covariance case as explained in detail in section 2.1.3.2.3. For 3D problems, the aspect tensor at each grid point has six independent components corresponding to a special configuration (a "hexad") of oblique lines of the grid. The background error pattern is constructed by applying six recursive filters along these specific six directions. In order to find the aspect tensor at each grid point for the flow-dependent background error covariance defined in Eq. (3.4), it is necessary to rewrite Eq. (3.4) in matrix and differential form to obtain the aspect tensor in analytical form. The finite difference $f_i - f_j$ in Eq. (3.4) is approximated by infinitesimal differential df and distance r_{ij} is replaced by the differential $d\mathbf{y}$, then we obtain

$$\mathbf{B} = \sigma_b^2 \exp\left[-\frac{1}{2}\left(\frac{d\mathbf{y}^T d\mathbf{y}}{L_r^2} + \frac{(df)^2}{L_f^2} \right) \right], \tag{4.5}$$

where superscript T denotes transpose. This spatial reach of the anisotropic background error correlation should shrink along the direction of strong gradient of the error field compared to the corresponding isotropic one. For example, if the gradient of the error field is large in a given direction, then the difference in the background errors is large, i.e., df is large, so that the background error correlation is small between points in that direction, according to Eq. (4.5). Alternatively, the background error covariance can be written in a general Gaussian form that involves the aspect tensor, $\mathbf{A}$, as follows,

$$\mathbf{B} = \sigma_b^2 \exp\left(-\frac{1}{2} d\mathbf{y}^T \mathbf{A}^{-1} d\mathbf{y} \right). \tag{4.6}$$

Equating Eq. (4.5) and Eq. (4.6) then gives

$$dy^T \mathbf{A}^{-1} dy = \frac{dy^T dy}{L_r^2} + \frac{(df)^2}{L_f^2}. \tag{4.7}$$

Differentiating the above equation twice with respect to **y,** and making the assumption that second derivatives of f can be neglected, gives the inverse of **A** as follows,

$$\mathbf{A}^{-1} = \frac{\mathbf{I}}{L_r^2} + \frac{(\nabla f)^T (\nabla f)}{L_f^2}, \tag{4.8}$$

where ∇f is the gradient vector of f field. For 3D problems, **I** is a 3×3 identity matrix in our case. Note that in the cases where different geometric length scales are used for the horizontal and vertical directions, term $\mathbf{I}/L_r^2$ in Eq. (4.8) should be a more general diagonal matrix. The aspect tensor **A** is a 3×3 symmetric and positive definite matrix and should have six independent components in general. It is locally defined at each grid point but is assumed to vary smoothly in space. Its linear projection onto the appropriate hexad's weights is therefore also a smooth function over the region of physical space to which that particular hexad configuration maps. When L_f goes to infinity, the anisotropic filter reduces to the special case of the isotropic one since, in this situation, the second term on the right side of Eq. (4.8) vanishes. The resulting diagonal matrix A must therefore map to a degenerate hexad in which three of the six weights vanish while the filtering that corresponds to the three nonvanishing weights acts only along the coordinate direction. In this special situation, the effective filtering scale does not change with grid points when the geometric de-correlation scale, L_r, is also constant.

After obtaining the aspect tensor in analytical form, we can apply the hexad algorithm described in section 2.1.3.2.3 to determine the filtering directions and hexad

weights and then apply 1D recursive filter prescribed in Chapter 2 along these directions.

4.2.3 Estimation of background error field for anisotropic analysis

We have already evaluated a procedure to directly obtain a flow-dependent background error covariance in Chapter 3. Here we simply summarize that procedure and repeat it with recursive filters. The variable f in Eq. (4.8) represents the background error field. For simulated observations, we know the truth so the true background error is also known. We can use the true background error as f to obtain the aspect tensor **A** for flow-dependent background error covariance according to Eq. (4.8). Then valid filtering directions and associated weights can be determined by the aspect tensor at each grid point. This is what will be done in experiment ANISO to be described in section 4.5b. But for realistic applications, the true background error is not known before hand. In such a case, an estimate of the error is needed before we can perform any anisotropic analysis. Following Chapter 3, we perform, first, an analysis using isotropic background error (as in an experiment called ISO). The difference between this analysis from the background is then used as an estimate of the background error field, i.e., as f in Eq. (4.8). An anisotropic analysis is then performed and this experiment is referred to as UB, implying Updated background error covariance **B'**. Such a two-step iterative procedure is feasible in practice, and is in a sense a double-loop strategy that is similar in procedure to, although different in purpose from, the

double-loop approach commonly employed by operational systems of variational analysis (e.g., Courtier et al. 1994).
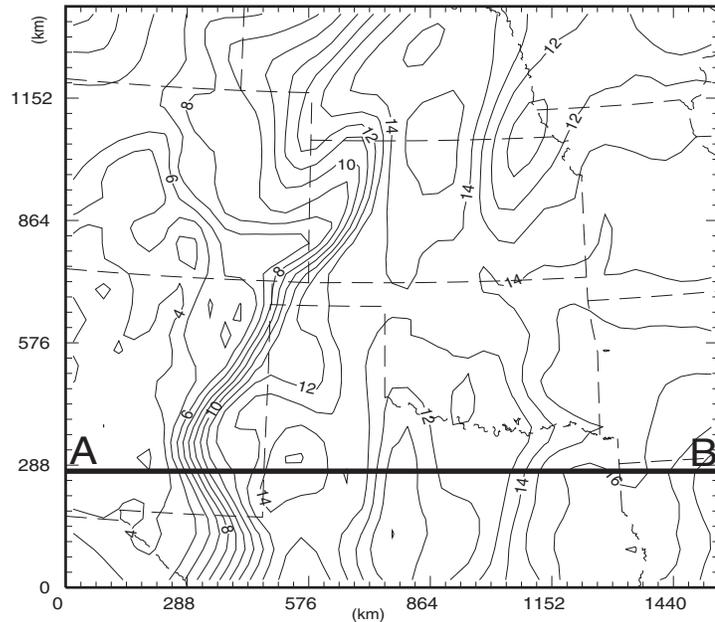
Fig. 4.1 The specific humidity, q_v, at the 5th terrain-following grid level, or about 500 meters above the ground, from ARPS 'truth' simulation for an IHOP case valid at 20 UTC, 19 June, 2002. The contour interval is 1 g kg^{-1}. The analysis domain is 1620 km x 1440 km in Great Plain. The dryline is represented by the strong gradient of q_v. The thick line A-B is at y = 270 km.

As in Chapter 3, we still use simulated observations to evaluate our 3DVAR system with a recursive filter. The generation of GPS *SWV* observations has been described in section 3.3 and the hypothetical GPS network is shown in Fig. 3.2. Shown in Fig. 4.1 is the truth at the 5th terrain-following model level, or about 500 meters above the ground. We show the truth of water vapor at the 5th model level rather than at the surface as in Chapter 3 because we desire to show more anlaysis results while at the same time we still can compare them with previous analyses from Chapter 3. Since the truth at the 5th model level and that at the surface are pretty similar, the horizontal cross-

sections of the figures shown in this chapter are mainly at the 5th model layer except for the single observation tests described in next section. Likewise, the vertical cross-sections of the figures shown in this chapter are along y = 270 km (thick line A-B in Fig. 4.1) rather than y = 234 km (thick line A-B in Fig. 3.1a).

4.3 Single observation tests

As in section 3.4.1, in order to assess the performance of the variational method described above using recursive filters and, more importantly, to understand the behaviors of the isotropic and anisotropic recursive filters, two single-observation experiments are performed using two-dimensional isotropic and anisotropic recursive filters, respectively. In such experiments, the *SWV* observation term is excluded from the cost function. Only one moisture observation at the surface marked by a filled black dot in Fig. 4.2 with a value of 14.72 g kg^{-1}, is analyzed. The background is set to a constant value of zero and the geometric de-correlation filter scale L_r is specified as 4 grid intervals. Since the filters are two dimensional, there is no coupling among the vertical levels therefore the analyses are essentially two dimensional. We will therefore examine the surface field only, which is impacted by the single surface observation.

Fig. 4.2 shows the surface analysis increments from these two experiments. Since the background is zero, the analysis increments are the analysis themselves and represent the corresponding structures of the background error covariance. Fig. 4.2a shows, as expected, the circular shape of the isotropic analysis increment. For the anisotropic case, L_r is also set to be equal to 4 grid intervals while L_f is specified as 2 g kg^{-1}. The true moisture field is used as the reference field (error field f) for this analysis

(the background is zero in this case). Strong anisotropy in the analysis increment is clearly revealed by Fig. 4.2b; the increment is stretched along the directions of the contours of the reference field. This is because the correlation decreases rapidly through
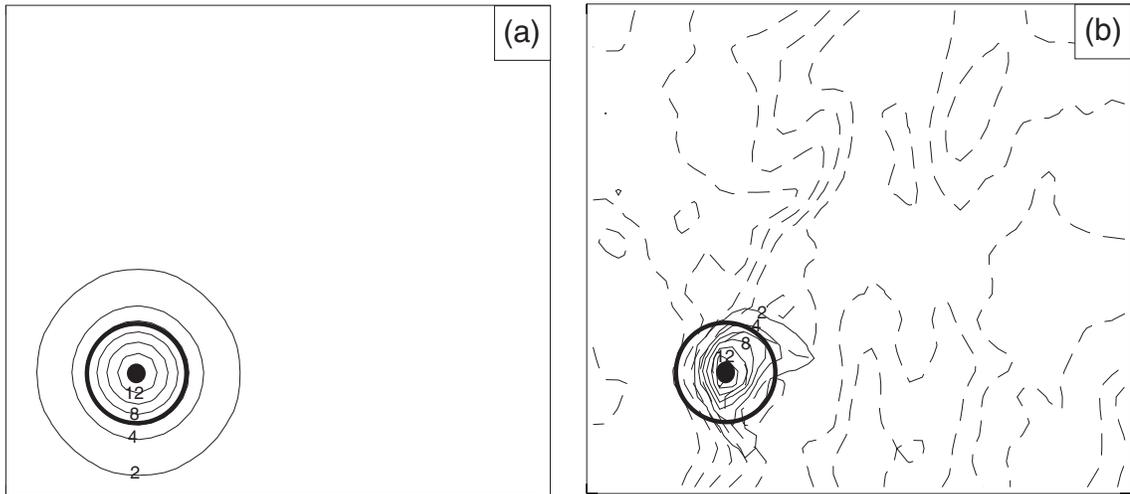
Fig. 4.2. Surface analysis increments from single observation experiments (a) for the isotropic example whose analysis increment is of circular shape and (b) for anisotropic example coupled to a reference field (dashed lines). The increment in the latter case is stretched along the contours of the reference field showing the strong anisotropy of the analysis. The contour interval for the increment is 2 g kg^{-1} and the first contour shown is at 2 g kg^{-1}. The filled black dots mark the locations of the single observations. A circle of radius $L_r = 4$ grid intervals and centered at the observation station is overlaid in thick black line in both panels.

the region where the reference field has a strong gradient, e.g., west of the single observation; in contrast, it decreases much more slowly near the northeast of the observation, where the gradient is small. The analyzed values at the observation station for both cases are about 14.69 g kg^{-1}, which is very close to the observed value 14.72 g kg^{-1}. This result is consistent with the given ratio, i.e., 1:500, of the weighting coefficients of the background and surface observation terms in the cost function; the analysis is much closer to the observation than to the background. In the current ideal

case where the background error covariance is modeled after the known truth, using an anisotropic recursive filter, the analysis should match the truth very well when a sufficient number of observations are present. This will be examined in the next section.

4.4 Three-dimensional moisture analysis

The single-observation experiments demonstrate correct behaviors of our analysis system using recursive filters. Subsequently, we move to the analysis of full 3D water vapor field from simulated *SWV* and surface moisture observations discussed in section 3.3. Three experiments are discussed in this section, which use different background error covariances. In all three cases, the observational data are error free, and the analysis background was created by smoothing the truth 50 times, using a 2-D quasi-horizontal 9-point filter on model levels. Our main purpose in this study is to examine the ability of our 3DVAR system to analyze meso- and small-scale moisture structures from the *SWV* and surface observations with an initial guess that does not contain such structures. The background produced by smoothing truth is adequate for this purpose. Example horizontal and vertical cross-sections of this smoothed field can be found in Fig. 3.4. The relative weighting coefficients of the four terms in the cost function are specified as 1, 100, 500 and 50, respectively, same as in Chapter 3.

In the first experiment, called ISO (Table 4.1), the correlation between any two points is only a function of their distance, so the covariance is isotropic; it is modeled using the isotropic recursive filter. The covariance is also assumed to be spatially homogeneous. For the latter two experiments, the correlation is the function of not only the distance but also the error structure; the covariance is therefore state-dependent (or

flow-dependent) and is modeled using an anisotropic recursive filter. For the first of the two, called ANISO (Table 4.1), the error field is based on the truth field, i.e., the f in Eq. (4.8) is equal to the truth minus analysis background. Through this experiment we can determine how well our analysis system can recover the 3D humidity field from the *SWV* and surface moisture observations under an ideal condition. For the second of the two anisotropic experiments (called UB, Table 4.1), the iterative procedure described in section 4.2.3 is employed, in which an estimate of the error field, as the difference between the first isotropic analysis and the background, is used for the subsequent anisotropic analysis.

Experiment	Observational errors	anisotropic Filter	RMSE (g kg^{-1})	CC	CC in Chapter 3
ISO	No	No	0.35	0.84	0.83[*]
ANISO	No	Yes	0.28	0.91	0.93
UB	No	Yes	0.34	0.86	0.83
UB_err	5% sfc error 7% *SWV* error	Yes	0.42	0.80	0.79

[*]$L_r = 4$, in unit of grid point, is optimal for the ISO experiment in this chapter while $L_r = 3$ is optimal in Chapter 3.

Table 4.1 List of retrieval experiments. In this table, *SWV* denotes GPS slant-path water vapor data and 'sfc' denotes the surface moisture observation data. CC is the overall correlation coefficient and RMSE is the root-mean square error between the derived moisture increment and the true moisture increment (truth minus background).

4.4.1 Analysis with an isotropic background error covariance model

The one-dimensional fourth-order isotropic recursive filter is applied along each coordinate direction using one pass only (Purser et al. 2003a). The horizontal and

vertical filtering scales are chosen to be four grid intervals which are found to be nearly optimal for this case (see later discussion in subsection 4.5.1). The choices of the geometric part of the filtering scales are, in practice, often linked to the observational network density; we want the observation innovations to spread far enough to at least cover the gaps between ground receiver stations (in the current case the station spacing is 4 grid intervals). The sensitivity of the analysis to the value of the de-correlation length scale is examined in section 4.5.1.

Fig. 4.3 shows the cost function and the norm of the cost-function gradient as functions of the number of iterations during the minimization procedure for experiment ISO. Significant reductions (by at least two orders of magnitude) occur in both the cost function and the norm of the gradient during the first 100 iterations. In all cases, we run the minimization algorithm for 100 iterations, which should be sufficient for the desired accuracy.

Shown in Fig. 4.4 is the east-west vertical cross-section of the analyzed 3D water vapor field (dashed lines) versus the truth of the moisture field (solid lines) at $y = 270$ km (along A-B line in Fig. 4.1). It can be seen that the analysis follows the truth reasonably well. The moisture contours take an essentially vertical orientation at the location of the dryline (about $x = 360$ km) below the 1.5 km level. This boundary separates the dry air from the high plateau to the west and the moist air originating from the Gulf of Mexico to the east. Moisture ridges and troughs are found at the right locations and the moisture extrema match the truth well also.

This analysis obtained using an isotropic recursive filter is actually much better than that obtained using an explicit isotropic Gaussian filter (c.f., Fig. 3.7). All

parameter configurations are the same as experiment SNF in Chapter 3 except for the geometric de-correlation scale L_r, which was set to 3 grid intervals that was found to be optimal for that case. In the case of explicit filtering, the correlation had to be cut off at
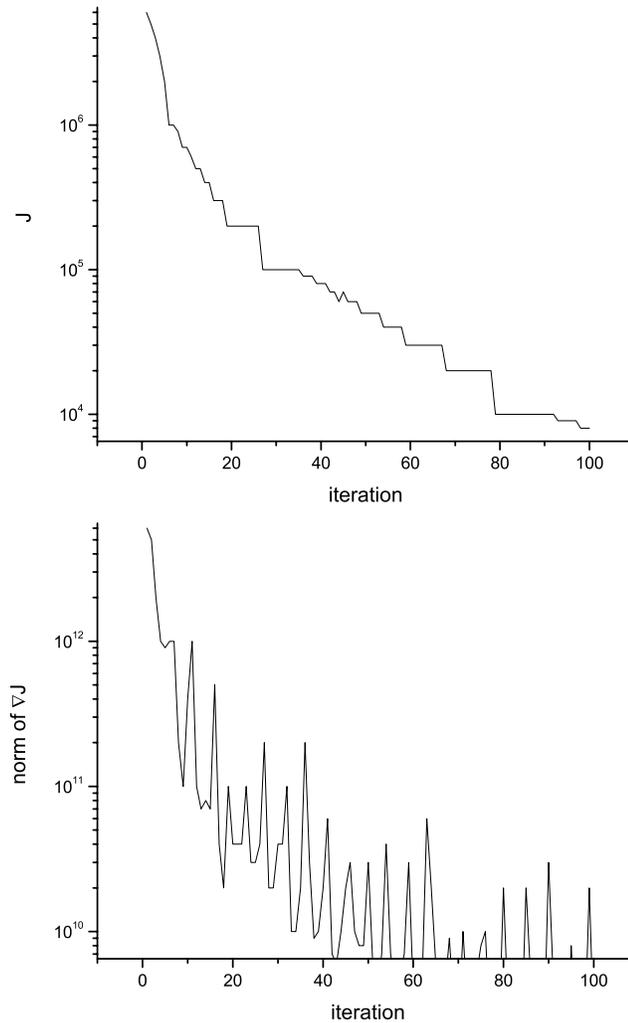
Fig. 4.3 The variation of the cost function J and the norm of the gradient ∇J with the number of iterations during the minimization procedure for experiment ISO.

a certain distance to keep the computational cost manageable. This action actually destroys the exact positive definiteness of the background error covariance[4] although the effect is usually small. In the case of the recursive filter, no cut-off radius is necessary so that the positive definite property can be preserved. In addition, the recursive filter does have the important advantage of being much more computationally efficient than the explicit filter.
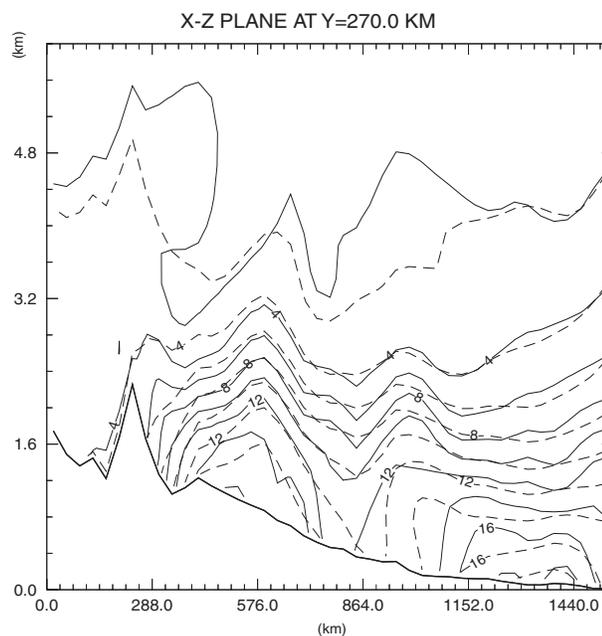
Fig. 4.4 East-west vertical cross-section of the retrieved specific humidity field (dashed lines) from experiment ISO at y = 270 km versus the truth (solid lines). The contour interval is 2 g kg^{-1}.

The analysis increment at the 5th model level is presented in Fig. 4.5a, together with the corresponding truth increment (truth minus background) in Fig. 4.5b. They show roughly similar patterns and extremum locations. The dryline can be recognized

[4] We have since realized that Gaspari and Cohn (1999) have proposed filter functions for localizing covariance while preserving the positive definiteness. These functions can be applied to the explicit filter although they do not solve the problem we have with anisotropic explicit filter.

easily in the analysis. The overall correlation coefficient (CC) and the root-mean square error (RMSE) between the analysis increment and the truth increment are presented in Table 4.1. The CC is 0.84 and the RMSE is 0.35 g kg^{-1}, both indicating good analysis. For reference, the RMSE for the background is 2.70 g kg^{-1}.
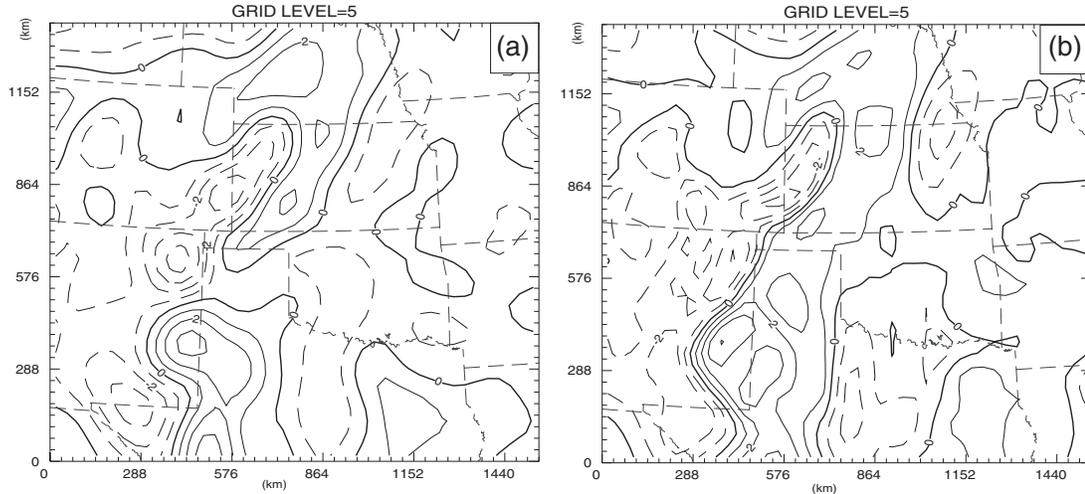
Fig. 4.5 (a) Analysis increment of q_v at the 5th grid level from the experiment ISO. (b) Truth minus background at the same level. The contour interval is 1 g kg^{-1}. Dashed lines represent negative values and solid lines positive values.

4.4.2 Analysis with an anisotropic background error covariance model

Experiment ANISO is performed to examine how the anisotropic background error covariance affects the analysis. The chosen de-correlation scales are four grid intervals for L_r and 2 g kg^{-1} for L_f. This set of scales will be shown to be nearly optimal in section 4.5.1. The analysis increment at the 5th grid level shown in Fig. 4.6a matches the truth increment (Fig. 4.5b) very well. The dryline pattern is analyzed with pronounced similarity to the truth. Their extremum locations coincide almost exactly.

The analysis through the same vertical cross section as in Fig. 4.4 is shown in Fig. 4.6b.

Obviously, there is a significant improvement compared to the analysis of ISO. The

dryline structure is analyzed very well and the analyzed moisture contours almost

coincide with the truth. The fine-scale structures are also captured well. For example,

the $q_v = 14.0$ g kg^{-1} contour has a sharp downward drop at x = 620 km in the truth, a

fine-scale feature that is also captured by the analysis. Further, an upward moisture

bulge at x = 300 km, associated with upward motion at the dryline, is recovered very

well by this anisotropic analysis but is missed in the isotropic analysis. The overall CC

and RMSE for experiment ANISO are, respectively, 0.91 and 0.28 g kg^{-1} (Table 4.1),

obviously better than those of ISO.
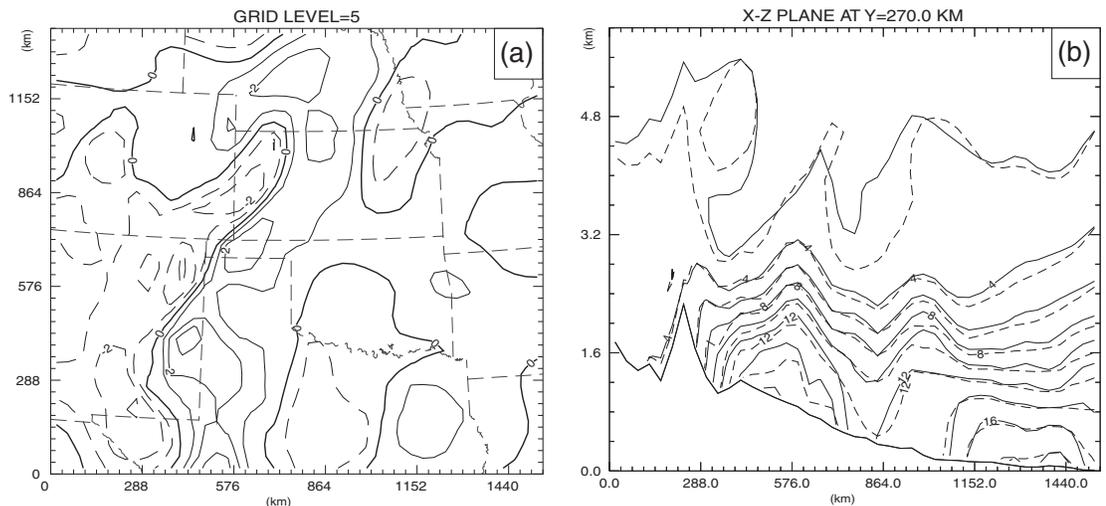
Fig. 4.6 (a) Analysis increment of q_v at the 5th grid level from experiment ANISO with contour interval 1 g kg^{-1}, where dashed lines are for negative values and solid lines for positive values. (b) East-west vertical cross-section of q_v at y = 270 km with interval 2 g kg^{-1}. Solid lines are for truth and dashed lines for experiment ANISO.

4.4.3 Anisotropic analysis based on estimated background error field

Experiment ANISO presented previously has shown clearly that the use of an anisotropic spatial filter improves the results of analysis when the background error covariance is modeled based on the structure of true error field. This suggests that flow-dependent background error covariance can play a significant role in 3DVAR system. However, in reality, the true error field is not known before hand. One promising solution is to use an ensemble of forecasts to estimate the flow-dependent error covariances (e.g., Buehner 2005) but the cost of running the ensemble is high. Here, we present results from experiment UB, which has been introduced at the beginning of the section 4.4 and also discussed in section 4.2.3. Experiment UB uses a two-step iterative procedure.
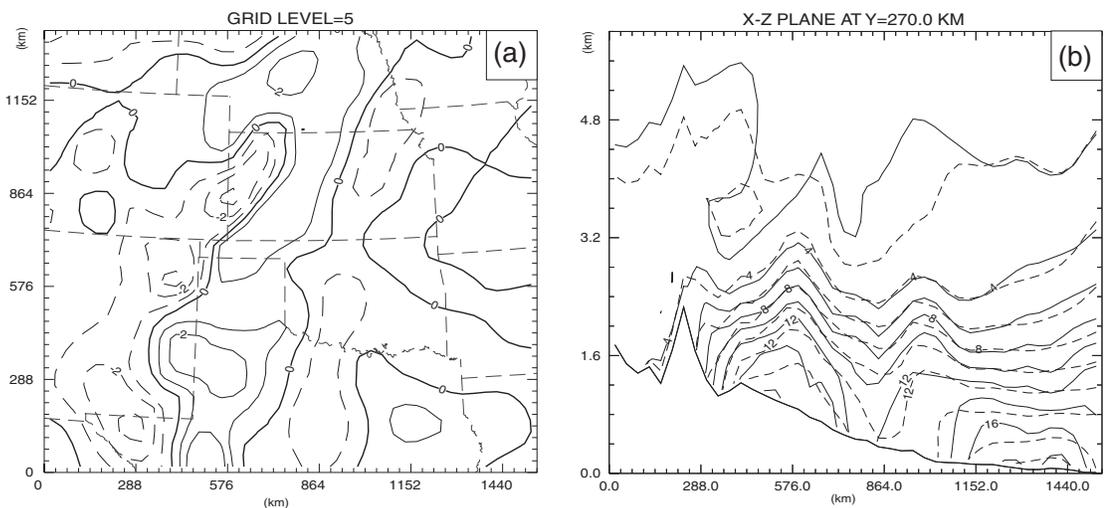
Fig. 4.7 Same as in Fig. 4.6 but for experiment UB.

The analysis of UB is shown in Fig. 4.7. The analysis increment at the 5th grid level (Fig. 4.7a) is more stretched along the dryline direction in comparison with the analysis from ISO (Fig. 4.5a), and the pattern also agrees with that of the true increment (Fig. 4.5b) much better. The agreement of the analysis with the truth is also excellent in the vertical cross section (Fig. 4.7b). For example the 4 and 6 g kg^{-1} q_v contours match the truth contours down to the fine scale details while the fine-scale details of the ISO analysis are not as good (Fig. 4.4). These fine-scale structures may play an important role for accurate convection initiation along a dryline and the subsequent precipitation forecast. The CC and RMSE for this experiment are 0.86 and 0.34 g kg^{-1}, respectively, compared to the 0.84 and 0.35 g kg^{-1} of ISO. The improvement, though not as dramatic as ANISO, is nevertheless evident. This improvement is in fact more evident in the analyzed fields shown in Fig. 4.7 than these scores reveal.

Compared to the analysis from experiment SUF in Chapter 3, we found that the dryline structure in this analysis using recursive filter is more prominent suggested by the more stretched analysis increment along the dryline. It is also supported by the CC from experiment UB (0.86) higher than CC from experiment SUF (0.83).

To provide a quantitative measure of the difference between the flow-dependent **B** derived from the 'updated' error field (i.e., the 'updated' **B** used in experiment UB) and that derived from the true error field (i.e., the 'truth-based' **B** used in experiment ANISO), we calculate the L2-norm of the difference (matrix) between the two matrices. It is found that this difference is a factor of 2.5 smaller than that between the truth-based **B** and the isotropic **B** (i.e., the **B** used in experiment ISO), indicating that the updated **B** is much closer to the truth-based **B** than the isotropic one.

The above procedure for estimating **B** is an iterative procedure. One naturally would ask if additional iterations would further improve the estimation of **B** and the subsequent analysis. To seek the answer, additional iterations were performed. It was found that the quality of analysis after the third iteration remains essentially the same, therefore only one update step or two total iterations are employed here. This result may be case dependent, however. It should be tested when applying it to other cases.

4.5 Sensitivity experiments

4.5.1 Sensitivity to de-correlation scales

The quality of an analysis is closely related to the de-correlation scales used in the definitions of both isotropic and anisotropic background error covariances, Eqs. (3.3) and (3.4). These scales control the spatial extent over which an observation increment is spread. Fixed values of L_r (4 grid intervals) and L_f (2 g kg^{-1}) were used in the earlier 3D moisture analysis experiments. We examine in this subsection how the analysis quality varies with the de-correlation scales, as measured by the CC and RMSE of the analysis increment with the true increment. In these sensitivity experiments, the weighting coefficients specified for the terms in the cost function remain the same.

In the isotropic case, only L_r is a free parameter. Given that the truth of moisture is known, we can explore the parameter space of L_r in order to find a value that yields the best moisture analysis. In Fig. 4.8, the dotted line shows the RMSEs of analysis as a function of L_r (in units of analysis grid intervals). We see that the optimal de-correlation length scale is equal to four grid intervals for this isotropic case. This appears

reasonable because the 4 grid interval is actually the distance between our uniformly spaced ground receivers.
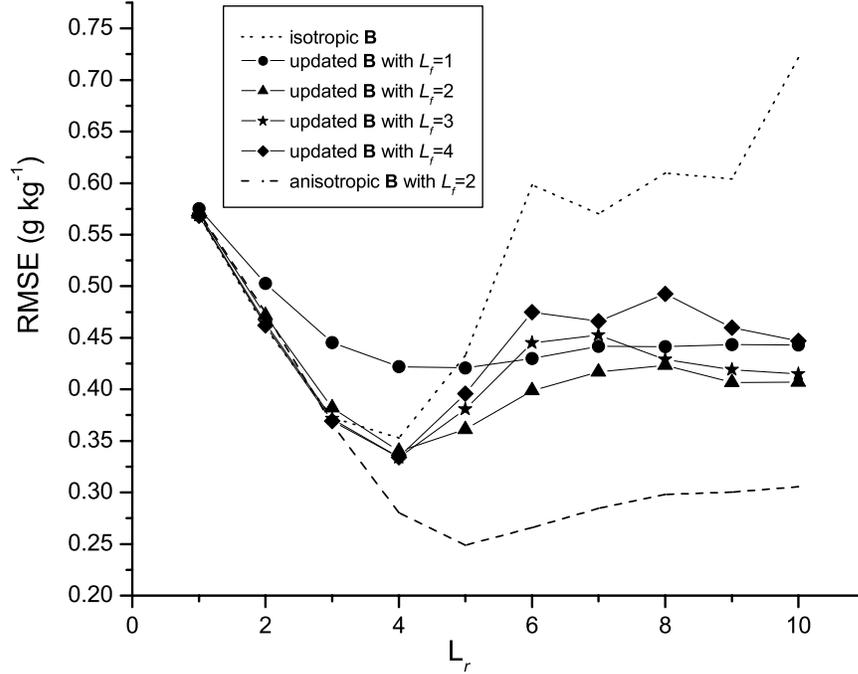
Fig. 4.8 The overall RMSE (g kg^{-1}) between retrieved 3D analysis increments and the true increment (truth minus background), as a function of the geometric de-correlation scale L_r (in units of analysis grid intervals). The dotted line is for the experiments using the isotropic recursive filters and the dashed line is for the experiments using the truth-based anisotropic background error covariance with $L_f = 2$ g kg^{-1}. The solid lines are for the experiments with the anisotropic error covariances based on the 'updated' error fields with $L_f = 1, 2, 3, 4$ g kg^{-1}, respectively.

In the anisotropic case, there are two free parameters, L_r and L_f, so we explore the parameter space of the correlation model to find the set of L_r and L_f that yields the best analysis. For the experiments that use 'updated' **B,** the RMSEs (solid lines in Fig. 4.8) as a function of L_r are presented for four different values of L_f, that is, 1, 2, 3 and 4 g kg^{-1}. It can be seen that for the $L_f = 1$ g kg^{-1} case, the RMSEs are the largest among all

cases when $L_r \leq 4$ grid intervals. This suggests that this value of L_f is too small when L_r is also small, so that the combined spatial correlation fails to fill the gaps between observation stations. For other more appropriate values of L_f, the optimal value of L_r is 4 grid intervals. Overall, the optimal de-correlation scale set is $L_r = 4$ grid intervals and $L_f = 3$ g kg^{-1} for the 'updated' **B** cases.

The dashed line in Fig. 4.8 shows the RMSEs as a function of L_r, for experiments that use the **B** based on that the true error field. ANISO is one of the experiments. L_f is equal to 2 g kg^{-1} for these experiments. It is obvious that this set of experiments always yields the best analysis for a given value of L_r, compared to the other sets of experiments. It is also clear from Fig. 4.8 that when $L_r \geq 4$ the isotropic analysis is always worse than the corresponding anisotropic analyses with the same L_r, except for the anisotropic case with 'updated' **B** and $L_f = 1$ g kg^{-1}. For $L_r \leq 3$, the analyses are of similar quality except for the $L_f = 1$ g kg^{-1} case. As pointed out earlier, this value of $L_f = 1$ g kg^{-1} is too small. The RMSE increases considerably with L_r when it is larger than 4 grid intervals for the isotropic case whereas the worsening is much less significant for the anisotropic cases, indicating a much smaller sensitivity of the analysis to the choice of L_r in the anisotropic cases; the use of an improperly large L_r that helps to fill the observation gaps does not hurt as much as the isotropic case. This is because in the anisotropic case, the field-dependent covariance imposes an additional constraint on the spatial spread of the observation increment, and helps limit the potential damage of too large an L_r. As long as the choice of L_f is appropriate, the analysis tends to be good, according to Fig. 4.8.

4.5.2 Sensitivity to typical observation errors

All experiments presented so far use simulated *SWV* and surface moisture data that include no observation errors. In practice, the observations would not be error free, so it is important to test the sensitivity of the analysis to the observation errors, in part to test the robustness of our analysis system. We perform experiment UB_err, which is the same as experiment UB except for the errors added to the observations. The standard deviations added to the simulated surface and *SWV* observations are, respectively, 5% and 7% of the error-free values and the added errors are normally distributed with zero means. The *SWV* errors are consistent with the estimate of Braun et al. (2001) for real data. In this case, because of the presence of observation errors, the relative weighting coefficients for *SWV* and surface observation terms are specified to 15 and 29, respectively, relative to the 1 of the background term. These weights are specified to be proportional to the inverse of estimated background error variance and the variances of the errors added to simulated observations. The analysis from this experiment, though not as good as the corresponding error free case, still matches the truth reasonably well (Fig. 4.9). In other words, our 3DVAR analysis procedure is able to retrieve the 3D structure of moisture field from the slant-path water vapor observations (which are integrated values), even though the observations are contaminated by errors of typical magnitudes. This is also supported by the error statistics. The overall correlation coefficient of the increments decreases from the 0.84 of the error-free UB case to 0.80 and the RMSE increases from 0.35 g kg^{-1} to 0.42 g kg^{-1} (Table 4.1).
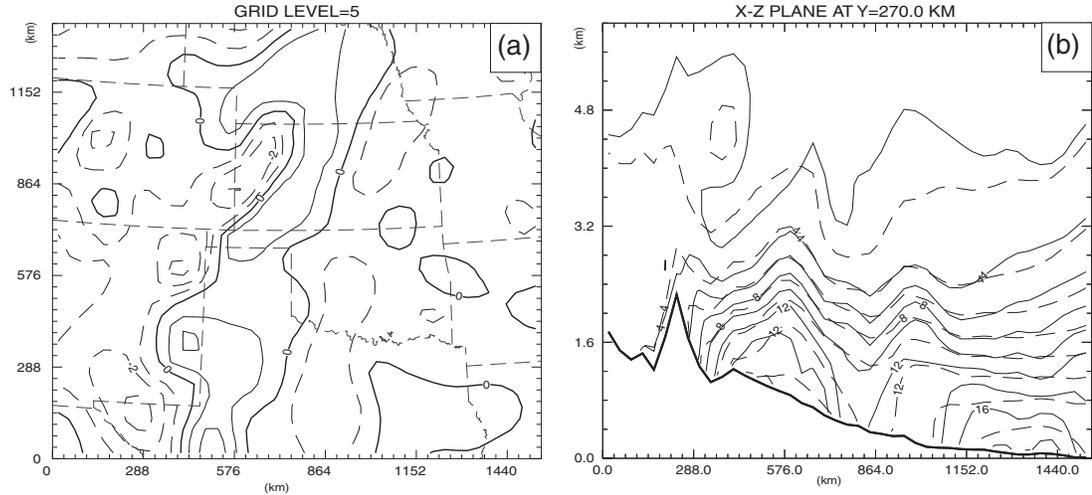
Fig. 4.9 Same as in Fig. 4.6 but for experiment UB_err.

4.6 Summary and discussions

Compared to those experiments in Chapter 3 which use an explicit spatial filter, a computationally much more efficient algorithm based on the recursive filter is implemented and evaluated in this chapter, for the purpose of analyzing three-dimensional water vapor fields from simulated GPS *SWV* observations. Surface moisture observations collected at the ground receiver sites are analyzed at the same time. The study in this chapter represents the first time that a fully anisotropic recursive filter is used for modeling flow-dependent background errors in the context analyzing GPS observations. The main conclusions are listed as follows.

1) The analysis, produced by our 3DVAR method with an isotropic recursive filter, captures the main structure of the dryline examined.

2) An anisotropic recursive filter, which is adaptive to the structure of the background error both in smoothing directions and spatial correlation scales, produces

significantly better analyses of the specific humidity field associated with a dryline than the isotropic one, especially in the fine-scale moisture structures.

3) In the absence of a good knowledge of the background error, a two-step iterative procedure to estimate it is proposed, in which an isotropic analysis is performed first. The difference between this tentative analysis and the background is used to define the error field needed by the flow-dependent background error covariance model. This estimated error field is then used in the second anisotropic analysis step. Improved analysis, compared to the isotropic one, is obtained through this procedure.

4) Experiments on the sensitivities of the analysis to the error de-correlation scales are performed. It is found that the isotropic analysis is more sensitive to the geometric de-correlation scale L_r and in such a case the range of L_r with which a good analysis is obtained is narrow. The analysis is much less sensitive to L_r, however, when the flow-dependent component of the background error is introduced. For the current dryline test case, the optimal geometric length scale L_r is found to be equal to the distance between neighboring GPS ground receiver stations.

5) The analysis procedure is found to be feasible and effective for this dryline case. The analysis is found to be not very sensitive to the presence of observational errors of typical magnitudes in the *SWV* data and in the surface moisture observations. But more sensitivity tests are necessary to show the statistical significance and widespread applicability of this finding.

6) Compared to the explicit filters examined in Chapter 3, the biggest advantage for using recursive filters is the computational efficiency. The computational cost of a

recursive filter is about one fortieth that of the corresponding explicit filter even when moderate cut-off radii are used with the latter. The quality of analyses using recursive filters are in general better than that obtained with explicit filters. In the isotropic case, the analysis obtained using the recursive filter is much better than that of the explicit filter.

The results of this study can be statistically more significant if the procedure tested against more cases. Further, the effectiveness of the two-step procedure for estimating the background error then using it in the analysis is worth further investigation, as they are applied to more cases. In the near future, we will use the retrieved moisture field to initialize a mesoscale model, such as the ARPS, and to examine the impact of assimilating *SWV* data on short-range precipitation forecasts. The assimilation and the examination of the impact of real *SWV* data collected during the IHOP_2002 field experiment are also planned.

Chapter 5
Prediction of Convection initiation and Storm Evolution on 12 June 2002 during IHOP_2002: Control Simulation and Sensitivity Experiments[5]

5.1 Introduction

During the warm season over the Southern Great Plains (SGP) of the United States, strong convective storms are responsible for a large portion of the annual rainfall. Accurate prediction of quantitative precipitation associated with these warm season systems has been a particularly elusive task (Fritsch and Carbone 2004). The prediction of the exact timing, location and intensity of convection initiation and the subsequent evolution of the convective systems are even more difficult. Such difficulties arise in part from the poor knowledge of four-dimensional water vapor distribution with high temporal and spatial variability, inadequate understanding of the convection initiation (CI) processes and the inability of typical numerical models to accurately represent important physical processes. To address some of these questions, the International

---

[5] This chapter is an extended version of our conditionally accepted paper: Liu, H. and M. Xue, 2007:Prediction of convective initiation and storm evolution on 12 June 2002 during IHOP_2002. Part I: Control simulation and sensitivity experiments. Mon. Wea. Rev., Conditionally accepted.

H$_2$O Project (IHOP_2002, Weckwerth et al. 2004) field experiment was carried out in the spring of 2002.

Weckwerth and Parsons (2006) present a review on convection initiation, in particular, that by surface boundaries prevalent in the SGP environment. Wilson and Roberts (2006) systematically summarize all CI events and their evolution during the IHOP period, based on observational data. The ability of the operational 10-km Rapid Update Cycle (RUC) (Benjamin et al. 2004) in predicting these events is also briefly discussed. Xue and Martin (2006a; 2006b, hereafter XM06a and XM06b respectively or XM06 for both) present a detailed numerical study on the 24 May 2002 dryline CI case.

In XM06, the Advanced Regional Prediction System (ARPS, Xue et al. 2000; Xue et al. 2001; Xue et al. 2003) and its data assimilation system were employed to simulate the events at 3 and 1 km horizontal resolutions. Accurate timing and location of the initiation of three initial convective cells along the dryline are obtained in the model at the 1 km resolution. Through a detailed analysis on the model results, a conceptual model is proposed in which the interaction of the fine-scale boundary-layer horizontal convective rolls (HCRs) with the mesoscale convergence zone along the dryline is proposed to be responsible for determining the exact locations of convection initiation. Worth noting of this case is that the CI did not occur at the intersection point between the dryline and a southwest-northeast-oriented surface cold front located in the north, or at the dryline-cold front 'triple point', which conventional wisdom would highlight as the location of highest CI potential. In fact, most of the observing instruments were deployed around the triple point that day, missing the true CI that actually occurred further south along the dryline.

Another CI event that was extensively observed during IHOP_2002 is that of 12 June 2002, which also involved a dryline intersecting a cold front. Further complicating the situation was a cold pool and the associated outflow boundary that ran roughly east-west and intercepted both cold front and dryline near its west end. In the afternoon of 12 June, CI occurred along and near the dryline, and along and near the outflow boundary. Some of these storm cells organized into a squall line into the evening and propagated through the central and northeast part of Oklahoma through the night, producing damaging wind gust, hail and heavy precipitation. On this case, Weckwerth et al. (2005) performed a preliminary observation-based study that employed multiple datasets and discussed pre-convective, clear-air features and their influence on convection initiation. This case is also one of the two highlighted in the survey study of Wilson and Roberts (2006). Because of the limitations of the observational data sets, the CI mechanisms of this case could only be hypothesized in these two observation-based studies. For the same case, Markowski et al. (2006) analyzed the 'convection initiation failure' in a region near the intersection of the outflow boundary and dryline. Data from multiple mobile Doppler radars were used in their analysis. This region was chosen for intensive observations because of its proximity to the outflow-boundary–dryline intersection point (similar to a triple point) but the actual initiation occurred about 40 km to the east and to the south along the dryline. Clearly, a better understanding of the CI mechanisms in this and other cases, and improvement in NWP model prediction skills, are much needed.

In this study, a similar approach to that employed in XM06 is used to study the CI processes and subsequent storm evolutions for the 12 June, 2002 case. Additional

numerical experiments are also conducted to evaluate the impact of various model and data assimilation configurations on the prediction of CI and storm evolution.

The rest of this chapter is organized as follows. In section 5.2, we discuss the synoptic and mesoscale environment of the 12 June 2002 case, the sequence of storm initiations along the dryline and the outflow boundary, and the subsequent evolution of these cells and their eventual organization into a squall line. Section 5.3 introduces the numerical model used and its configurations, as well as the design of actual experiments. The results are presented and discussed in sections 5.4 and 5.5 and a summary is given in section 5.6.

5.2 Overview of the 12 June 2002 case

As pointed out in the introduction, the case of 12 June, 2002 is a complicated one that involves a number of mesoscale features that interact with each other. Figure 5.1 shows the surface observations superposed on visible satellite imagery at 2045 UTC (all times are UTC unless otherwise noted) or 1445 LST, 12 June 2002 in the IHOP domain. There was an outflow left behind by a mesoscale convection system (MCS) earlier that day, located over southern Kansas (KS), northeastern Oklahoma (OK) and northwest Arkansas (AR). The southern boundary of this outflow (indicated by the dashed line in Fig. 5.1) stretched from far northwest OK to the northwest AR, separating the warm, moist, generally southerly flow to its south from the cool, but comparatively moist, easterly and southeasterly flow to the north of the boundary. During the day, this boundary receded to the north, acting more like a warm front. A weak cold front extended from the eastern OK panhandle (at the western end of the

outflow boundary) toward the south-southwest to the central Texas (TX) panhandle. A

dryline was present at the same time, oriented northeast-southwest from the eastern OK
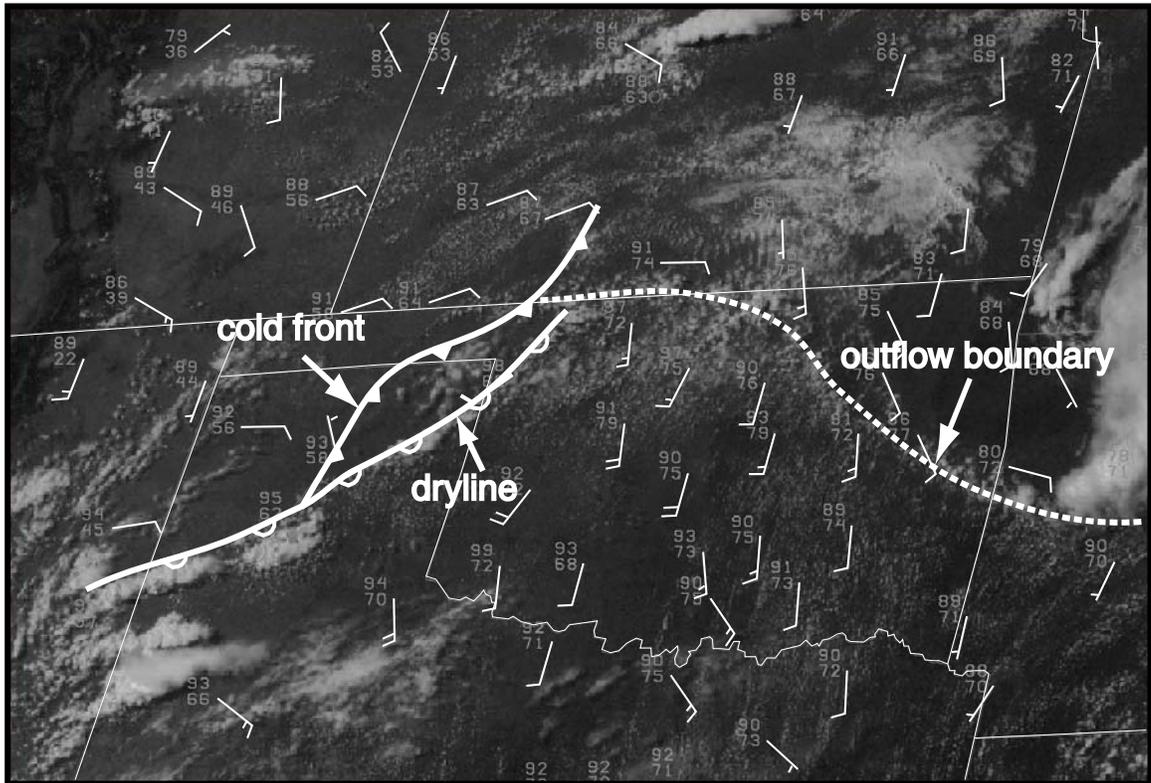
Fig. 5.1. Visible satellite imagery at 2045 UTC, 12 June, 2002, with surface observations overlaid. Station models show wind barbs in knots (with one full barb representing 10 knots), and temperature and dew point temperature in Fahrenheit.

panhandle to the southwestern TX panhandle and intersected the cold front at the

central TX panhandle (at the southern end of the cold front). Warm dry air existed west

of the dryline and ahead of the cold front where southwesterly winds dominated. Behind

the cold front, most of the winds came from the north or north-northeast. The low-level

winds showed the existence of a mesoscale cyclone west of the dryline-outflow

boundary triple point (see, e.g., Fig. 5.5 d). Another feature worth pointing out is a

region east of the dryline with generally southerly surface winds exceeding 15 knots

(7.7 m s^{-1}) which provided ample moist air for CI near the dryline and outflow boundary.

Shown in Fig. 5.2 is the surface convective available potential energy (CAPE, Fig. 5.2a)

and convective inhibition (CIN, Fig. 5.2b) at 2200, adapted from Wilson and Roberts

(2006). The CAPE maximum of over 5000 J kg^{-1} and CIN values near or lower than 15

J kg^{-1} were located along the outflow boundary. Near the intersection of the cold front

and the dryline, as well as along the southwest portion of dryline, the CAPE was over

3000 J kg^{-1} and CIN was smaller than 15 J kg^{-1}. These three regions were considered the

preferred CI locations based on these data.
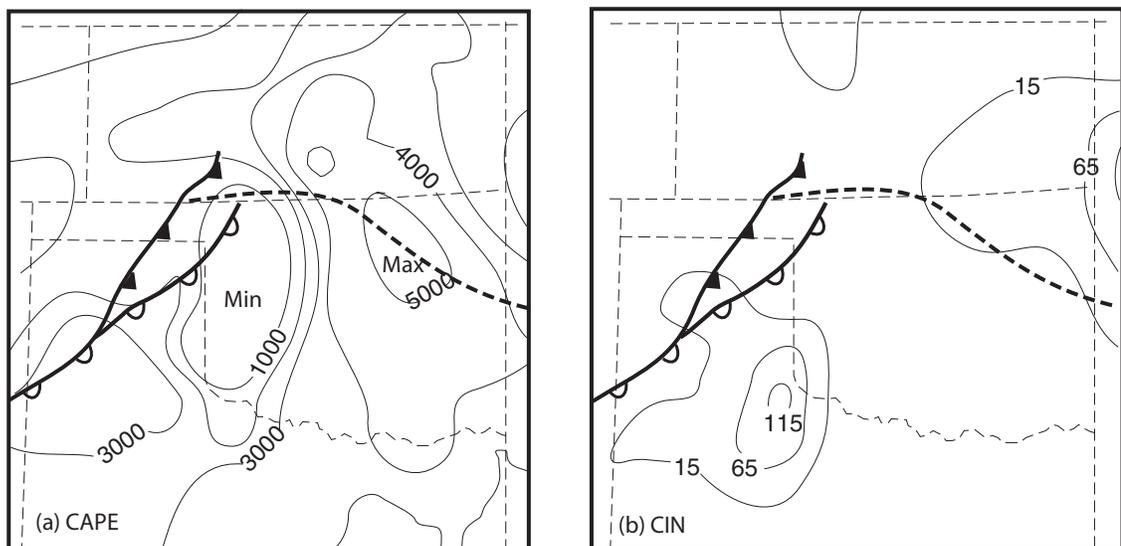
Fig. 5.2. (a) CAPE (contour interval of 1000 J kg-1) and (b) CIN (first contour at 15 J kg-1 with contour interval of 50 J kg-1) at 2200 UTC, 12 June, 2002 (adapted from Wilson and Roberts 2006).

Fig. 5.3 shows the multi-radar mosaic of composite (vertical column maximum)

reflectivity as produced by the procedure of Zhang et al. (2005) at 2130, 0000, 0100,

0300, which are the times when most storms were initiated, and when the squall line

was starting to organize, intensifying, and maturing, respectively. The first group of convective cells in Fig. 5.3 was initiated at about 1900 near the central TX-New Mexico (NM) border (denoted '1a' in Fig. 5.3a). One hour later (2000), the second cell group (denoted as '1b' in Fig. 5.3a) was initiated 100 km north of group '1a'. Group '1a' was ahead of the dryline while group '1b' was right over the southern extent of the dryline. During the next 40 minutes, more convective cells (denoted as '1c' in Fig. 5.3a) were initiated near these two groups. These regions were favorable for CIs as suggested by Fig. 5.2. At about 2030, near the intersection of the cold front and dryline near Amarillo, TX, another group of convective cells (denoted as '2' in Fig. 5.3a) was initiated and intensified quickly, leading to hail reports and strong winds along their gust fronts. During the next hour, additional convective cells formed, along the northern portion of the dryline (denoted as group '3') and near, but south of, the outflow boundary (denoted as group '4'). Further east along the outflow boundary, group '5' is found which was initiated at around 2000 (Fig. 5.3a). By 0000 of 13 June (Fig. 5.3b), these cells reorganized into somewhat different cell groups, denoted as 'A', 'B', 'C', '4' and '5'. Group A is basically the group evolved from '1a', and 'B' is a combination of groups '1b', '1c' and the southern part of '2' that underwent splitting during the period. Group 'C' was made up of the northern part of '2' and '3' while groups '4' and '5' maintained their identities. Between 2130 and 0000, more cells developed north of the OK-KS border (Fig. 5.3b). During the hour after 0000, cell groups 'A', 'B' and 'C' either weakened or nearly dissipated, while group '4' extended further westward into the eastern OK panhandle and group '5' grew in size (Fig. 5.3c). In the next 2 hours, groups '4' and '5', together with other cells between them and further to the east, became

connected and organized into a solid squall line (Fig. 5.3d) which continued its propagation southeastward for the next 3 hours until around 0600. The processes involved in the cell initiation and evolution will be discussed in more detailed in the next two sections, together with the model simulations of these processes.
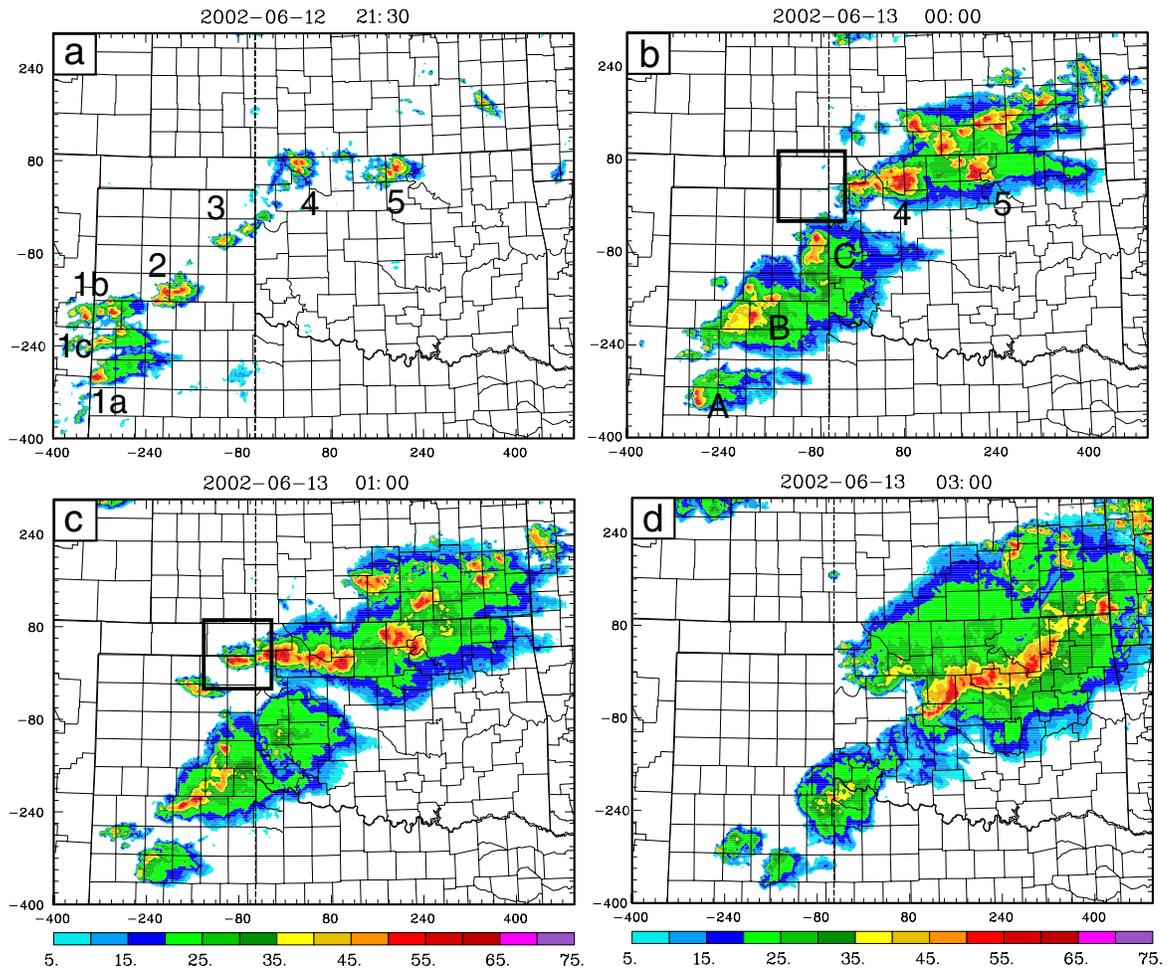
Fig. 5.3. Observed composite reflectivity mosaic at (a) 2130 12 June, (b) 0000, (c) 0100, and 0300 13 June, 2002. The letters 1a, 1b, 1c, 2, 3, 4 mark the CI locations. The black squared box in panels (b) and (c) corresponds to the small zoomed-in domain shown in Fig. 5.8.

5.3 Numerical model, data and experiment design

As in XM06, version 5 of ARPS (Xue et al. 2000; 2001; 2003) is used in this study. The ARPS is a nonhydrostatic atmospheric prediction model formulated in a generalized terrain-following coordinate. As in XM06, two one-way nested grids at 3 and 1 km horizontal resolutions, respectively, are used. In the vertical, the grid spacing increases from about 20 m near the ground to about 800 m near the model top that is located about 20 km above sea level. The 3 km resolution is believed to be high enough to resolve important mesoscale structures while 1 km resolution is necessary to begin resolving smaller convective structures, including the boundary layer horizontal convective rolls and individual cells of deep moist convection.

The model terrain and land surface characteristics on the 3 and 1 km grids are created in the same way as in XM06. The lateral boundary conditions (LBCs) for the 3 km grid are from time interpolations of 6-hourly NCEP (National Centers for Environmental Prediction) Eta model analyses and the 3-hour forecasts in-between the analyses, while the 1 km grid gets its LBCs from the 3 km forecasts at 10 min intervals. In this study, the results of numerical simulations are found to be sensitive to the lateral boundary locations of the 3 km grid, and the domain of the 3 km grid used in our control simulation (see Fig. 5.4) is much larger than that used in XM06. The impact of the domain size and boundary locations will be specifically discussed in section 5c.

The ARPS is used in its full physics mode (see Xue et al. 2001, 2003). The 1.5-order TKE-based subgrid-scale turbulence parameterization and TKE-based PBL-mixing parameterization (Sun and Chang 1986; Xue et al. 1996) are used. The microphysics scheme is the Lin et al. (1983) 3-ice microphysics while no cumulus

parameterization is activated. The NASA GSFC long and short-wave radiation package (Chou 1990, 1992; Chou and Suarez 1994) is used and the land surface condition is predicted by a two-layer soil-vegetation model initialized using the state variables presented in the Eta analysis.

The initial conditions of our numerical simulations are created using the ARPS Data Analysis System (ADAS, Brewster 1996), in either the cold-start mode where the analysis is performed only once using an Eta analysis as the background, or with intermittent assimilation cycles where ARPS forecasts from the previous forecast cycles are used as the background for the cycled analyses. For all experiments to be presented, the initial conditions, created with or without assimilation cycles, are valid at 1800, 12 June, about 1 hour preceding the first observed convection initiation near the dryline. As one of the intensive observation days of IHOP_2002 with convection initiation study as the mission goal, various remote sensing instruments were deployed on that day, in addition to routine and special conventional observations (Weckwerth et al. 2004). In this study, conventional forms of data are assimilated into the model initial condition, including those of (regular and mesonet) surface stations, upper-air soundings and wind profilers. Available aircraft data (MDCRS) are also included. Table 5.1 lists the standard and special data sets used, together with their key characteristics. Data from the IHOP-deployed NCAR S-pol radar and from the WSR-88D (Weather Surveillance Radar 88 Doppler) radars in the region are used extensively for verification, especially KVNX (at Enid, OK) and KAMA (at Amarillo, TX) radars (see Fig. 5.4).

After an initial condition is obtained at 1800 on the 3 km grid, the ARPS model is integrated for 9 hours until 0300, 13 June, 2002, the mature time of the squall line

system. The 1 km grid forecast also starts at 1800, with the initial condition interpolated from the 3 km grid, and runs until the same ending time. We will concentrate on presenting the results from 3 km experiments. The results of 1 km grid experiments will only be described briefly.
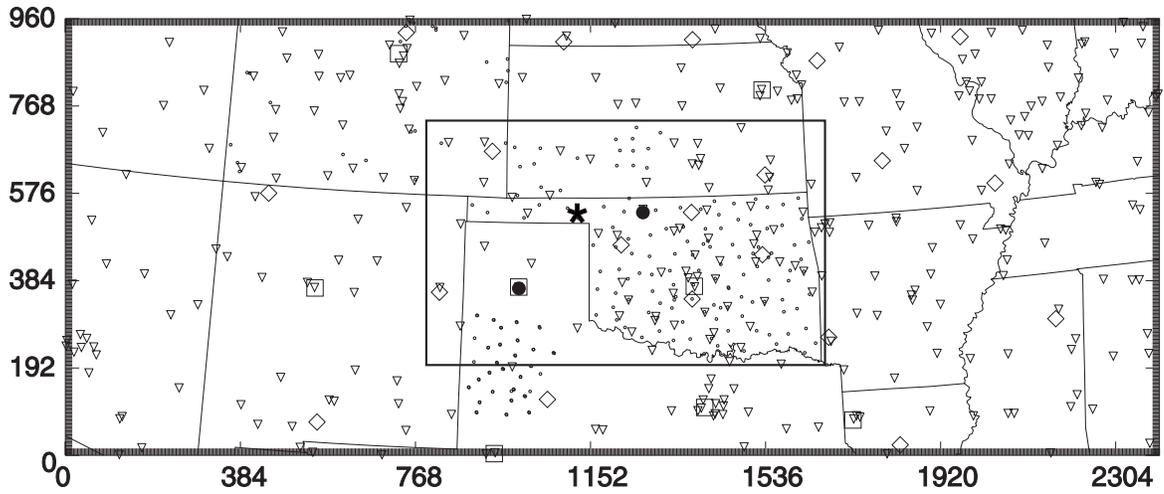
Fig. 5.4. The 3 km model domain used by all experiments except for SML, which uses the smaller domain shown by the rectangle in the figure. The stations of the Oklahoma Mesonet, the West Texas Mesonet, the southwest Kansas mesonet, the Kansas ground water management district # 5 network, and the Colorado agricultural meteorological network are marked by small dots; the stations from ASOS and FAA surface observing network (SAO) are marked by downward triangles; the stations from the NWS radiosonde network are marked by squares; and the stations from the NOAA wind profiler network are marked by diamonds. Two filled circles mark the locations of KVNX and KAMA WSR-88D radars in Okalahoma and Texas respectively. The filled star represents the S-Pol radar station.

In addition to a control simulation, we perform a set of sensitivity experiments at 3 km resolution to examine the impact of intermittent data assimilation cycles and IHOP special data, the effect of vertical correlation scales in the ADAS, and the effect of lateral boundary locations (Table 5.2). In all ADAS analyses, five analysis passes are performed, with each pass including different sets of data and using different spatial

Type of dataset	Abbreviation	description	Temporal resolution	Special or standard	Number of stations
Upper-air datasets	raob	National Weather Service (NWS) radiosonde network	3 hour	data at 1200 are standard, others are considered special	18 at 1200; 10 at 1500 and 1800
	wpdn	Wind Profiler Demonstration Network	1 hour	standard	20
	comp*	special composite data set composed of many upper-air observing networks	1 hour	special	1
	mdcrs	NWS Meteorological Data Collection and Reporting System aircraft observations	1 hour	special	varies
Surface datasets	sao	Surface observing network composed of the Automated Surface Observing System (ASOS) and the Federal Aviation Administration's (FAA) surface observing network.	1 hour	standard	about 250
	coag	Colorado Agricultural Meteorological Network	1 hour	special	29
	okmeso	OK Mesonet	1 hour	special	About 125
	swks	Southwest Kansas Mesonet	1 hour	special	8
	gwmd	Kansas Ground Water Management District # 5 Network	1 hour	special	10
	wtx	West Texas Mesonet	1 hour	special	30

*A description on the individual networks included in the composite can be found in Stano (2003)

Table 5.1 List of the abbreviations of the observation networks used in this study and some of their characteristics.

correlation scales. Table 5.3 lists the observations analyzed and the vertical correlation scales for the horizontal and vertical for each analysis pass, as used in all experiments unless otherwise noted. Using one pass more than in XM06, the horizontal correlation scale starts at a value slightly larger that in XM06, and ends at a value that is smaller. The vertical correlation scales are generally smaller than the corresponding ones used in XM06. These correlation scales were chosen based on additional experiments performed after the study of XM06 for the 24 May, 2006 case.

Table 5.2 lists all numerical experiments with abbreviated names and their descriptions. The control experiment, CNTL, includes the most data (Table 5.1). Standard and special IHOP observations are assimilated in hourly analysis cycles over a 6 hour period that ends at 1800. CNTL is designed to capture the convective cell initiations and later evolution into a squall line. Among the other experiments, COLD uses a cold-start analysis for the initial condition; 3HRLY uses two 3-hourly assimilation cycles while 6HRLY uses a single 6-hourly cycle. STDOBS includes only standard observations, as listed in Table 5.2, while ZRANGE tests the impact of different vertical correlation scales used in ADAS, and SML tests the impact of lateral boundary locations.

The performance of forecasts is evaluated by comparing the timing and locations of the initiations of convective cells along and near the dryline and the outflow boundary against radar observations. The structure and evolution of the model storms and their later organization into a squall line are examined by comparing predicted and observed reflectivity fields.

Experiment	Assimilated data	Assimilation interval	CI1a	CI2	CI3	CI4
			Time of CI in model Position error			
CNTL	all data	1 hour	2040 40 km SW	2040 < 5 km	2250 60 km NE	2130 20 km NE
COLD	all data	single analysis at 1800	Missing	Missing	2120 < 10 km	Missing
3HRLY	all data	3 hours	2030 40 km SW	2040 < 5 km	2200 70 km NE	2050 15 km NE
6HRLY	all data	6 hours	2030 60 km SW	2100 < 5 km	2140 70 km NE	2050 50km NE
STDOBS	standard data only	1 hour	2050 40 km SSW	2030 10 km E	2140 < 10 km	2040 5 km E
ZRANGE	all data	1 hour	2030 100 km SW	2000 < 5 km	2220 70 km NE	2100 5 km N
SML	all data	1 hour	1940 10 km N	2010 10 km NE	2240 70 km NE	2110 20 km N
Time of observed initiation			1900	2030	2130	2100

Table 5.2 Table of numerical experiments and their characteriscs. CI1, CI2, CI3, and CI4 refer to the convection initiation near the southwest most portion of the dryline, near Amarillo, Texas, the intersection of cold front and dryline, and near Woods, Oklahoma, near the intersection of outflow boundary and dryline, corresponding to cell groups '1a', '2', '3' and '4', respectively.

Pass number	Analyzed observations	Horizontal filter length scale (km)	Vertical filter length scale (m)
1	raob, wpdn, comp,mdcrs	320	500
2	raob, wpdn, comp, mdcrs, sao	160	100
3	sao, coag, okmeso, swks, wtx, gwmd	80	100
4	sao, coag, okmeso, swks, wtx, gwmd	50	50
5	coag, okmeso, swks, wtx, gwmd	30	50

Table 5.3. List of analyzed observations and the horizontal and vertical correlation scales used by each pass of the ADAS analysis in all experiments except for ZRANGE.

5.4 Results of the control experiment

In experiment CNTL, standard and special surface and upper-air observations (see Table 5.1) are assimilated from 1200 through 1800 at hourly intervals. The analyzed surface fields of temperature, mean sea level pressure, wind and water vapor mixing ratio during this 6-hour period show strong surface heating and the formation of a mesoscale low center near eastern OK panhandle (Fig. 5.5).

The surface analysis, at the end of 6-hour assimilation window, on the 3 km grid, is shown in Fig. 5.5d. The main surface features discussed earlier, including the cold front, dryline, outflow boundary and mesoscale low, are evident in the analysis. There

exists a moisture gradient along the entire length of the dryline and strong convergence

along the southern half of the dryline where the cold front is absent. In the northern
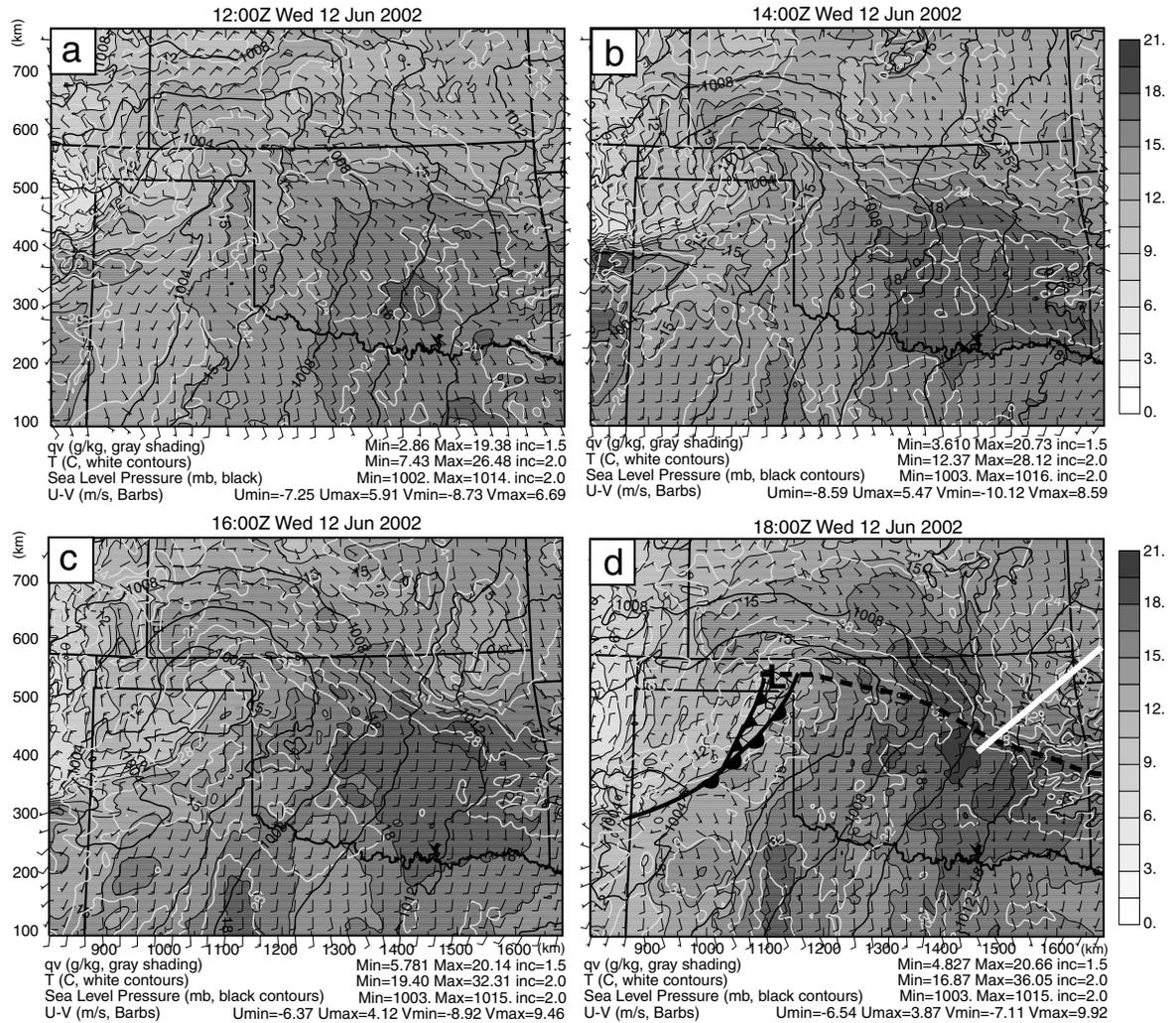
Fig. 5.5 The surface fields of temperature (thick white contours, °C), mean sea level pressure (thick black contours, hPa), water vapor mixing ratio (gray shading plus thin black contours, g kg^{-1}) and the wind vector (full barb represents 5 m s^{-1}, half barb 2.5 m s^{-1}) from ADAS analysis at (a) 1200 UTC, (b) 1400 UTC, (c) 1600 UTC, (d) 1800 UTC 12 June 2002. In panel (d), the thick straight white line indicates the vertical cross-section shown in Fig. 5.11. The cold front and dryline are marked by standard symbols. The even thicker black dashed line marks the MCS outflow boundary.

portion, the convergence straddles the zone between the cold front and dryline. The wind shift line along the outflow boundary is present; wind convergence is found along this line. North of the boundary, especially near the central OK-KS border, moisture is enhanced. To the south of the boundary and east of the dryline, strong southerly winds with speeds between 5 and 10 m s^{-1} exist at the surface, with the strongest winds being located in western OK and central TX; they bring rich moisture into the region and provide a favorable environment for CI and for the establishment of a squall line later on.

Significant fine-scale structures exist in the surface moisture field, as indicated by the wiggles on the specific humidity contours. These are related to the boundary layer (dry) convective structures that develop due to surface heating, and are generally of smaller scales than can be captured by the surface observation networks. In fact, such details are absent in the single-time analysis of cold-start experiment COLD (Table 5.2), and most of the gradients are also weaker in that analysis (not shown).

In general, the prediction of convection initiation in CNTL is good. Fig. 5.6 depicts the forecast fields of water vapor mixing ratio and winds at the surface, and the composite (vertical column maximum) radar reflectivity at 2130, 12 June, 2002 and at 0000, 0100 and 0300 of 13 June, which can be compared directly to those in Fig. 5.3.

The model predicts the convection initiation at the intersection of the cold front and dryline near Amarillo, TX (denoted as '2' in Fig. 5.3a or CI2 in Table 5.2) remarkably well. The model convection is initiated around 2040 and shows up as fully developed cells at 2130 (marked by '2' in Fig. 5.6a). The location of this group of cells is almost exact and initiation timing error is about 10 minutes.

For the groups of cells denoted as '1a', '1b' and '1c" in Fig. 5.3a, the situation is more complicated. In the real world, these cells were initiated over a period of about 1.5 hours, starting at 1900, as described in section 2. The cells along the dryline, marked by '1b' in Fig. 5.3a, were initiated around 2000. In the model, there are not three separate
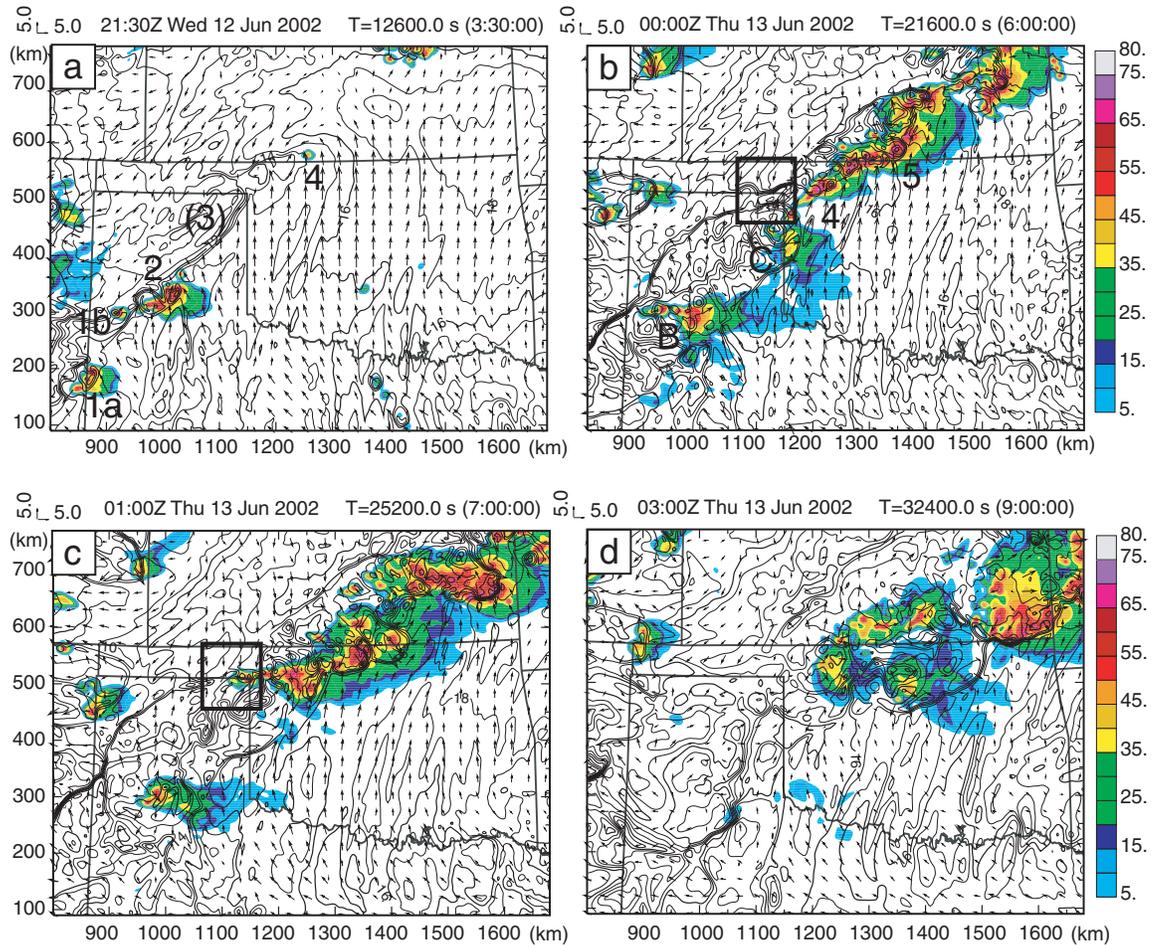
Fig. 5.6. The forecasted surface fields of water vapor mixing ratio (contours, g kg^{-1}), the wind vector (m s^{-1}) and composite reflectivity (shaded, dBZ) at (a) 2130, 12 June, 2002 (b) 0000, (c) 0100 and (d) 0300, 13 June, 2002 from CNTL run. The number 1, 2 and 4 in (a) indicate the locations of three primary convective cells. The black squared box in (b) and (c) corresponds to the small zoomed-in domain shown in Fig. 5.8.

groups of cells as observed. A group of cells is initiated along the TX-NM border, south of the dryline at around 2040, at roughly the location of observed group '1a'. At 2130 (Fig. 5.6a), this group matches very well the observed cells in location (Fig. 5.3a). The cells associated with observed group '1b' are much weaker in the model and are located further east along the dryline, but still separate from observed '2' (Fig. 5.3a), especially as earlier times (not shown). Despite these discrepancies, the overall behavior of model forecast in this region is still quite good.

Additional convective cells along the northern part of the dryline (group '3' in Fig. 5.3a) also developed in CNTL, but at a later time between 2240 and 2300 (not shown) or about 1.5 hours later than the observations. They are marked as '(3)' in Fig. 5.6a where '( )' indicates that the cells do not yet exist at this time. In the real world, part of cell group '2' merged with group '3' between 2130 and 0000 to form the group marked by 'C' in Fig. 5.3b, located on the west side of the western OK-TX border. In the model, a similar process occurred during this period and the model group 'C' is located off to the east side of the same OK-TX border (Fig. 5.6b), giving rise to a location error of less than half a county or about 30 km.

In the model, a small cell starts to become visible at 2130 ('4' in Fig. 5.6a) that corresponds to the observed group '4' near the OK-KS border. The observed cell '4' had a similar intensity as this model cell in terms of radar echo at around 2110 and reached 55 dBZ intensity by 2130 (Fig. 5.3a); there is therefore a time delay of 20 to 30 minutes in the model with this cell. The model initiation occurred about 20 km northeast of the observed one. This cell does occur in the model to the south of the surface wind shift and convergence line and to the east of the dryline, as was observed

by radar which can identify the dryline and convergence line as reflectivity thin lines (not shown).

The evolution of the model predicted reflectivity pattern is similar to that observed. In the real world, cell group '2' split at around 2150, with the southern part merging with groups '1b' and '1c' to eventually form group 'B' and the northern part merging with group '3' to form group 'C' (Fig. 5.3b). Group '1a' remained by 0000 of June 13 (Fig. 5.3b). In the model, the splitting of group '2' started to occur at around 2140 with some sign of splitting visible at 2130 (Fig. 5.6a); the northern part moved northeastward and merged with some much weaker cells in the model (model group 3) that developed along the northern portion of the dryline to form group 'C'. Group 'C' gained its maximum echo intensity of almost 70 dBZ near Amarillo, TX at around 2330, the same time observed reflectivity reached maximum intensity, then started to weaken. By 0000, when it crossed the western OK border, it was already rather weak; it dissipated quickly afterwards. Such an evolution is very similar to the observed one. As pointed out earlier, the peak intensity of the observed group 'C' also occurred before 0000 (the time of Fig. 5.3b), at around 2330.

In the model, the southern part of the split group '2' moved south-southeastward slowly and merged with the northeastward propagating group '1', at around 2350 to form group 'B' seen in Fig. 5.6b. This group then died out gradually over the next three hours (Fig. 5.6c and d).

Almost all cells that were initiated along the dryline dissipated by 0300, June 13, both in the real world (Fig. 5.3d) and in the model (Fig. 5.6d). The main development between 0000 and 0300 June 13 occurred along the outflow boundary close to the OK-

KS border, and the storm cells there eventually organized into a squall line by 0300 (Fig. 5.3d). Actually, cell groups '4' and '5' found at 2130 (Fig. 5.3a) represent the origin of the final organized squall line system. These cells formed just south of (group '4') or along (group '5') the outflow boundary, and intensified (Fig. 5.3b) and merged with new cells that developed over the ensuing few hours near the convergence boundary, as well as with cells that formed east of the dryline in northwest OK before 0000. In the model, cell group '4' is found at a similar location as the observed counterpart at 0000 (Fig. 5.6b) while the modeled group '5' is located further north than the observed, and exists in the form of a connected line rather than more discrete cells. The group of cells in a northeast to southwest oriented line north and northeast of group '5' seems to also match the observations well at this time. In the model, these cells apparently formed near the convergence boundary that had been pushed northward across the OK-KS border by the strong southerly flow. A similar development appears to have occurred in the real world too, based on more frequent radar maps (not shown).

By 0000, observed cell group '4' had already gained an elongated east-west orientation (Fig. 5.3b). During the next hour, this 'line' extended westward by about 100 km (Fig. 5.3c) through the initiation of new cells. The initiation of these cells in a region behind the dryline was actually due to the collision between the original outflow boundary and the northwestward propagating gust front from the earlier dryline convection. Such a process is most clearly seen in the low-level reflectivity fields of the NCAR S-pol (S-band polarimetric) radar deployed in the OK panhandle during IHOP. In Fig. 5.7, the gust fronts and the convergence lines are seen clearly as thin lines with enhanced reflectivity. At 2303, two outflow boundaries are clearly visible (Fig. 5.7a)

and by 0006 (Fig. 5.7b), the eastern portion of the gust front, in a bow shape, has just collided with the northern outflow boundary, starting to produce new cells pointed to by the large open arrow. The western, stronger, bow-shaped gust front was advancing and spreading rapidly and collided before 0006 with the eastern bow-shaped gust front, producing a cell pointed to by double solid arrows. But 0036, only 30 minutes later, this western portion has also collided with the northern outflow boundary, triggering and leaving right behind the gust front a new cell, indicated by the large black arrow (Fig. 5.7c). By 0100, this cell and the one formed earlier to the east, i.e., the two indicated by the two large arrows, reached their full strength and started to merge laterally (Fig. 5.7d).

Interestingly, almost exactly the same processes occurred in the model (Fig. 5.6b,c and Fig. 5.8). At 2300 (Fig. 5.8a), the two predicted outflow boundaries as indicated by bold dashed lines, are seen to match very well the observed ones (Fig. 5.7a). At 0000 (Fig. 5.8b), the cell (pointed to by double arrays) triggered by the two bow-shaped outflow boundaries are almost exactly reproduced, so are the shape and location of the three outflow boundaries. The cell pointed to by the large open arrow also matches observation at this time. By 0030, the western portion of the northward advancing boundary has collided with the northern one, and produced, as observed, a new cell, pointed to by the large black arrow, and by 0100, this new cell as well the eastern one intensified and the shape, intensity and location of these two cells match the observations almost exactly (Fig. 5.8d and Fig. 5.7d). These cells became the westward extension of cell group '4' (Fig. 5.6c), as observed (Fig. 5.3c).
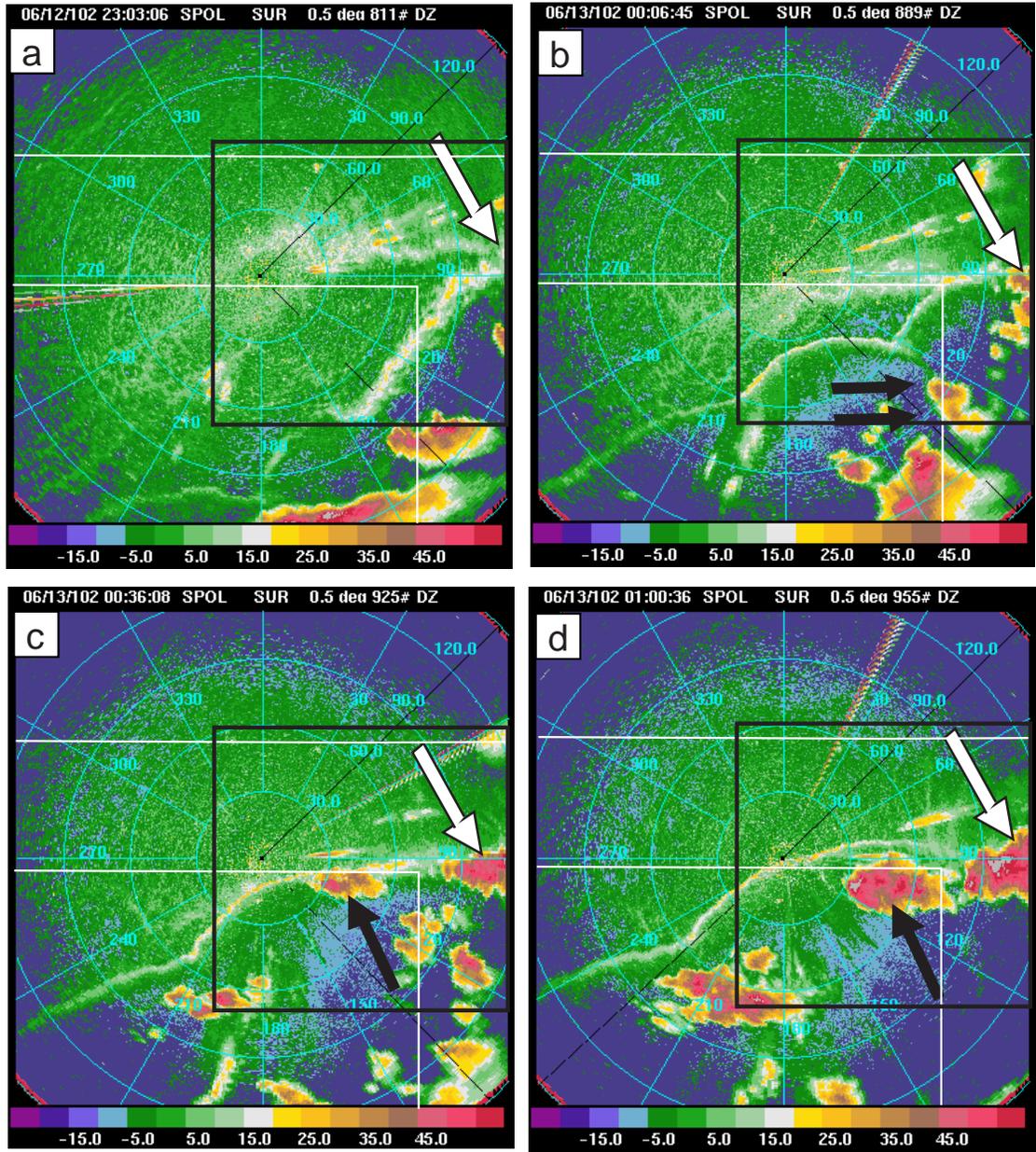
Fig. 5.7. The S-Pol radar reflectivity observations at 0.5 degree elevation angle at (a) 2303, 12 June 2002, (b) 0006, (c) 0036 and (d) 0100, 13 June 2002. The large black box in each panel indicates the domain shown in Fig. 5.8 and the arrows point to the locations of convective cells triggered by collisions of outflow boundaries.
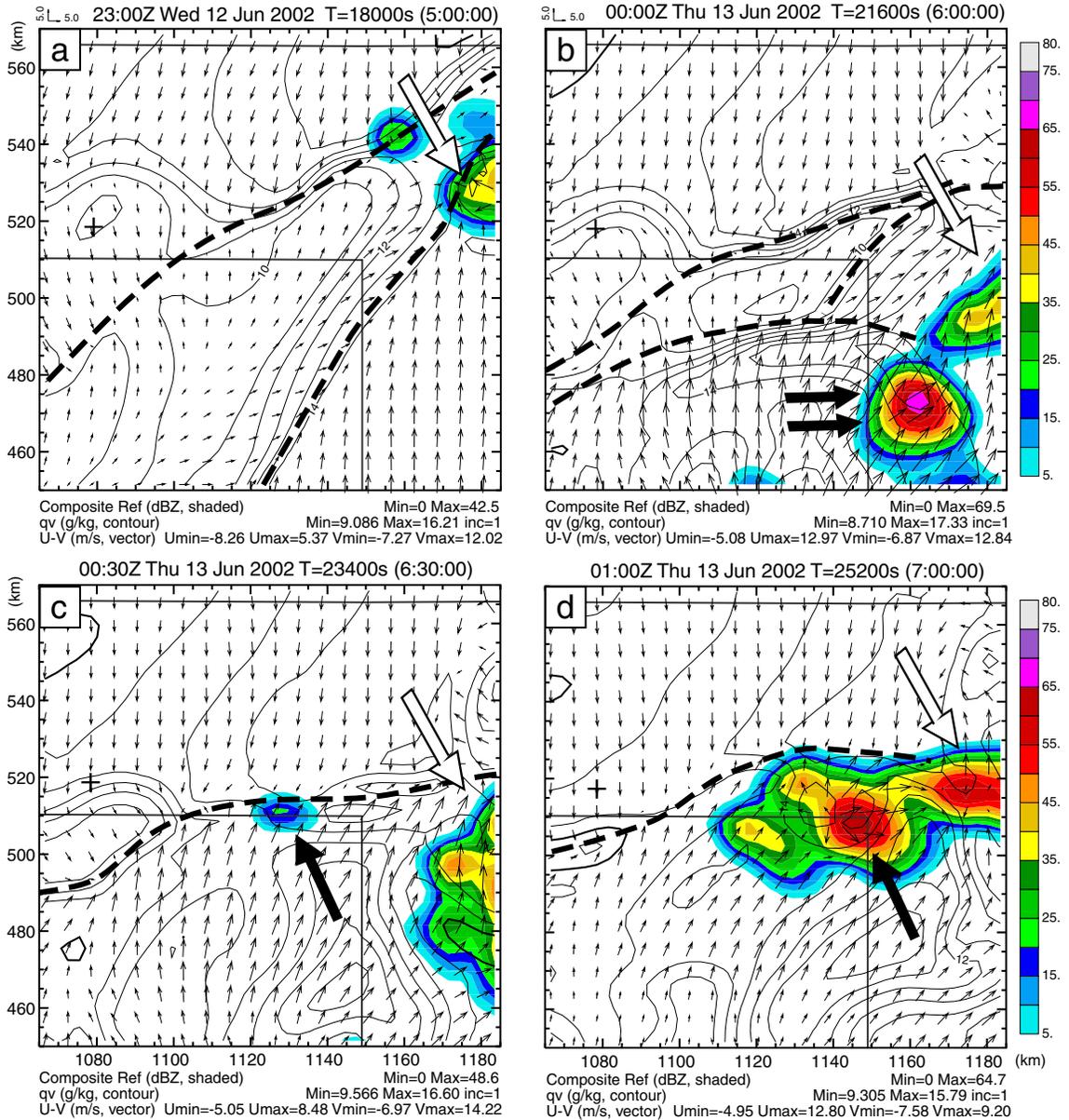
Fig. 5.8. As Fig. Fig. 5.6, but for a zoomed-in region shown by the black squared box in Fig. 5.6b and for times (a) 2300, 12 June 2002, (b) 0000, (c) 0030 and (d) 0100, 13 June 2002, that are close to the times of NCAR S-pol observations shown in Fig. 5.7. The '+' sign indicates the location of S-pol radar. The arrows point to convective cells to be discussed in the text and the bold dashed lines indicate the outflow convergence boundaries.

In the next 2 hours from 0100, the model did not do a good job in organizing the cells into a squall line. The cells in group '4' that should have contributed to the western

section of the squall line weakened subsequently and remained too far north, in northwest OK, while those that should make up the eastern section remained too far northeast, in the far southeast corner of KS (Fig. 5.6d). As will be shown in later sensitivity experiments, too strong southerly flow found in eastern OK is at least partly responsible for the dislocation of the eastern part of the squall line.

In summary, experiment CNTL presented above which incorporated routine and special observations through hourly assimilation cycles successfully reproduced many of the observed characteristics of cell initiation in a complex mesoscale environment that involved an intensifying mesoscale low, a dryline, a cold front as well as an outflow boundary resulting from an earlier mesoscale convective system. The predicted location and timing of most of the cells.agree rather well with observations, with CI timing errors being only about 10 minutes and location errors being less than 5 km for one cell group. The secondary cell initiation due to the collision between the pre-existing outflow boundary and the new gust front developing out of earlier dryline convection is also predicted very well by the model. The most significant problem is with the lack of organization of the cells into a solid squall line after 0010, or 7 hours into the prediction. The difficulty in maintaining the position of the initial outflow boundary to within northeastern Oklahoma in the model appears to have contributed to this problem, which appears to be related to the too strong southerly flow in that region. This issue will be explored through a sensitivity experiment that attempts to better analyze the initial cold pool behind the outflow boundary and one that uses a different eastern boundary location which results in a somewhat better flow prediction in eastern OK. Further, the 3-km model resolution may have been inadequate for the cell

interaction and organization. The impact of higher resolution will be examined in Part II.

The results of sensitivity experiments will be presented in the following sections.

5.5 Results of sensitivity experiments

5.5.1 The impact of data assimilation length and frequency and the impact of special IHOP data

For high-resolution convective-scale prediction, special issues exist for arriving at the optimal initial condition. At such scales, conventional observational data, including those from mesoscale surface networks, usually do not have sufficient resolution to define storm-scale features. Improper assimilation of such data sometimes can cause undesirable effects such as weakening existing convection in the background and introducing unbalanced noise. The simulation reported in XM06 used only a single 6-hourly assimilation cycle, and no impact of data assimilation was examined in that study. For the prediction of an isolated supercell storm event, Hu and Xue (2007) examined the impact of assimilation window length and assimilation intervals, for storm-scale radar data. The prediction results were found to be sensitive to the assimilation configurations.

Among all experiments presented in this paper, CNTL assimilates the most data (Table 5.2). Both standard and IHOP special observations (Table 5.1) are assimilated during a 6-hour time window at hourly intervals. To examine the impact of assimilation interval, we perform additional experiments 3HYLY and 6HRLY, in which both standard and special observations are assimilated, but at 3 hourly and 6 hourly intervals,

respectively, over the same 6 hour period (between 1200 and 1800). In addition, in 'cold-start' experiment COLD, a single analysis without assimilation cycle is performed at 1800.

Another experiment, called STDOBS (Table 5.2), was also performed, which is the same as CNTL except for the exclusion of special data collected or gathered by IHOP. Here, the surface data routinely available from the Automated Surface Observing System (ASOS) and the Federal Aviation Administration's (FAA) surface observing network (SAO data in Table 5.1), and the NWS radiosondes available twice daily and the hourly wind profiler network data are considered standard data. All other data listed in Table 5.1 are considered special data, including special soundings taken at 1500 and 1800. For all cases, 9-hour forecasts were performed, and the results are compared in terms of the prediction of CI and subsequent storm evolution.

Fig. 5.9 shows the model predicted fields of composite reflectivity, and surface water vapor mixing ratio and wind vectors from COLD, 3HRLY, 6HRLY and STDOBS, valid at 0100. It can be seen that the overall storm structure in COLD matches the observed reflectivity shown in Fig. 5.3c poorly (e.g., the convection in western TX is mostly missing) while those in the other three experiments match observations better, especially for the convection in northwest OK. However, unlike in CNTL, the initiation of new convection in eastern OK panhandle due to the collision of outflow boundaries (c.f., Fig. 5.6c) is missing in all of these experiments. In 6HRLY, the convection in western TX is over predicted (compare Fig. 5.9c and Fig. 5.3c) while in STDOBS, the convection is overall too strong. At the southwestern end of the overall system, the convection and the associated cold pool spread too far southeastward (Fig. 5.9d v.s. Fig.

5.3c), and the cold pool in northern OK and in KS appears to have also spread too far, creating two separate lines of cells along the gust fronts on its southeast and northwest sides. All other experiments predicted one dominant line of cells along the southern gust front as observed. Overall, the prediction of CNTL matches the observation best, at least at this time.
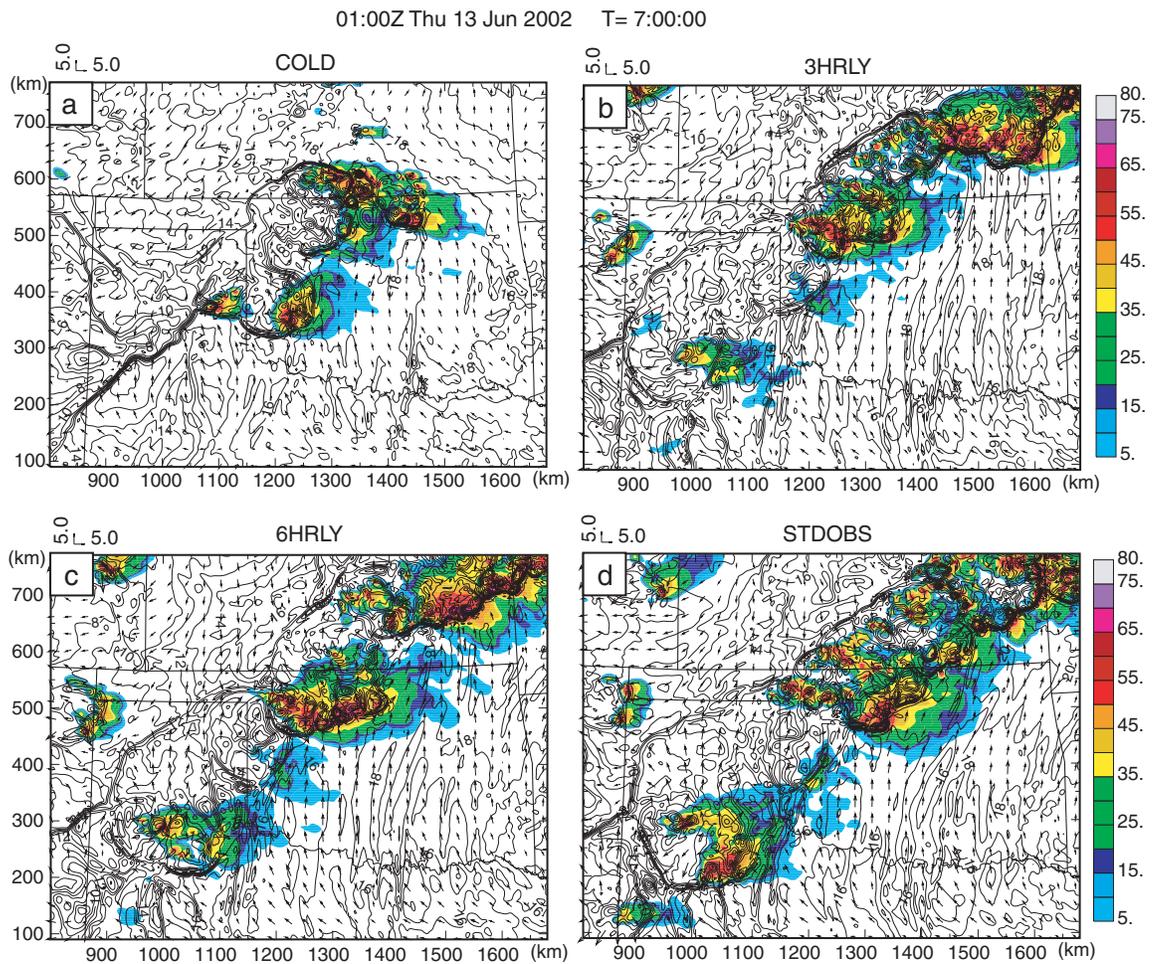
Fig. 5.9. As Fig. 5.6c but for experiments (a) COLD, (b) 3HRLY, (c) 6HRLY and (d) STDOBS, at 0100, 13 June, 2002.

Table 5.2 lists the timing and location errors of the four primary cell initiations ('CI1a', 'CI2', 'CI3', 'CI4'), as compared against radar observations. Here the timing of convection initiation is determined as the time of first significant radar echo or reflectivity exceeding 30 dBZ. It can be seen that in most cases, the model CI tends to be delayed compared to observations. In the case of COLD, CI1a, CI2 and CI4 are completely missing. In all other cases listed in the table, the model was able to predict all 4 CIs, although with different degrees of accuracy. Among the 5 experiments (CNTL, COLD, 3HRLY, 6HRLY and STDOBS), 3HRLY has the best timings for CI1a and CI4, STDOBS has the best timings with CI2 and CI3, while 6HRLY shares the best timing for CI3 with STDOBS, and for CI4 with 3HRLY. CNTL has timing accuracies for CI1a and CI2 similar to the other experiments, but has delay in the initiation of CI3 and CI4 (2250 v.s. observed 2130 for CI3 and 2130 v.s. 2100 for CI4). The other three experiments predict the initiation of CI4 somewhat earlier instead. Overall, CI2 is best predicted; the presence of strong cold front-dryline forcing is probably the reason. The differences in the timing and location errors of CI1a among the successful experiments are also relatively small; again probably due to the strong dryline line forcing.

Intuitively, experiment CNTL assimilated the most data, so the final analysis at 1800 should be more accurate than those obtained using fewer data. We believe this is true for the analysis of mesoscale and synoptic scale features, including the dryline, outflow boundary, mesoscale low, and the broad flow pattern in general, as supported by the fact that the subsequent evolution of storms is predicted best in CNTL overall. Very frequent assimilation of mesoscale and synoptic scale observations do not, however, necessarily improve the analysis of *convective-scale* features or flow

structures that are resolved by the high-resolution model grid in the background forecast because of the insufficient spatial resolutions of such data. In this case, the 3 km grid is able to resolve a significant portion of the *convective-scale* ascent forced by the horizontal convergence of the developing dryline and the outflow boundary, and by boundary layer convective eddies and rolls (c.f., XM06b). The analysis of mesoscale data, being of much coarser spatial resolutions (at ~ 30 – 100 km), tends to weaken low-level horizontal convergence that develops in the model, hence weakening the forced ascent that is responsible for the triggering of convection.

A comparison between the forecast and an analyzed maximum vertical velocity time series from 1200 to 1800 in the regions where CI occurs later along the dryline, shows that the analyzed maximum vertical velocities are always less than those of the background forecast; i.e., the analysis reduces small-scale upward motion. We believe that the reduced ascent is partly responsible for the delay of CI4 and northward displacement of cells (because of the further northward retreat of the outflow boundary) in CNTL and in some of the other experiments, while the relatively coarse 3-km resolution is another major reason for the delay (Part II will show that the CI timing is much earlier when a 1 km grid is used). The dynamic consistency among the analyzed fields does not seem to be a major issue with the use of frequent hourly cycles.

The timing and location errors in STDOBS for CI1a and CI2 are similar to those of CNTL (Table 5.2). The predicted timing and location for CI3 and CI4 are better in STDOBS than in CNTL, however. For CI3, the timing error is only about 10 minutes (2140 v.s. 2130) and location error is less than 10 km, while for CI4, the timing error is 20 minutes (2040 v.s. 2100) and the location error is less than 5 km. The prediction of

these two CIs is much better than that of CNTL, which has a significant delay in both CIs. The prediction of the convective storm evolution at later times in STDOBS is not better than in CNTL, however, as discussed earlier; there is a significant over-prediction of convection at, e.g., 0100 (Fig. 5.9).

Cell group '4' was initiated near the dryline-outflow boundary 'triple' point, which was the focal point of intensive observation during IHOP_2002. The actual initiation was to the southeast of the triple point, however. Further, it is not obvious from the CAPE/CIN map (Fig. 5.2) that CI is preferred there. To better see how and why cell group '4' is initiated in the model, we plot in Fig. 5.10 the horizontal convergence (gray shading), specific humidity, temperature and wind fields at the surface for CNTL, 3HRLY, 6HRLY and STDOBS at their times of first cloud formation, for a small domain around CI4. The first cloud formation is determined as the time when the 0.1 g kg^{-1} contours of column maximum total condensate first appear within the plotting domain, which are shown as bold solid contours in the plots. Also overlaid in the plots are composite reflectivity contours for precipitation that first appear later on out of the initial clouds. We refer to such reflectivity as first echo. The times of first clouds are close to 2020, 2010, 2000 and 1950 for CNTL, 3HRLY, 6HRLY and STDOBS, respectively, while the corresponding times of first echo or CI are 2130, 2050, 2050 and 2040, as discussed earlier. The observed CI is at 2100. The maximum timing difference among the experiments is 30 minutes for the first cloud and that for first echoes is 50 minutes.

The general surface flow patterns at the time of first cloud are similar between CNTL and STDOBS (Fig. 5.10a and Fig. 5.10d) while those of 3HRLY and 6HRLY are
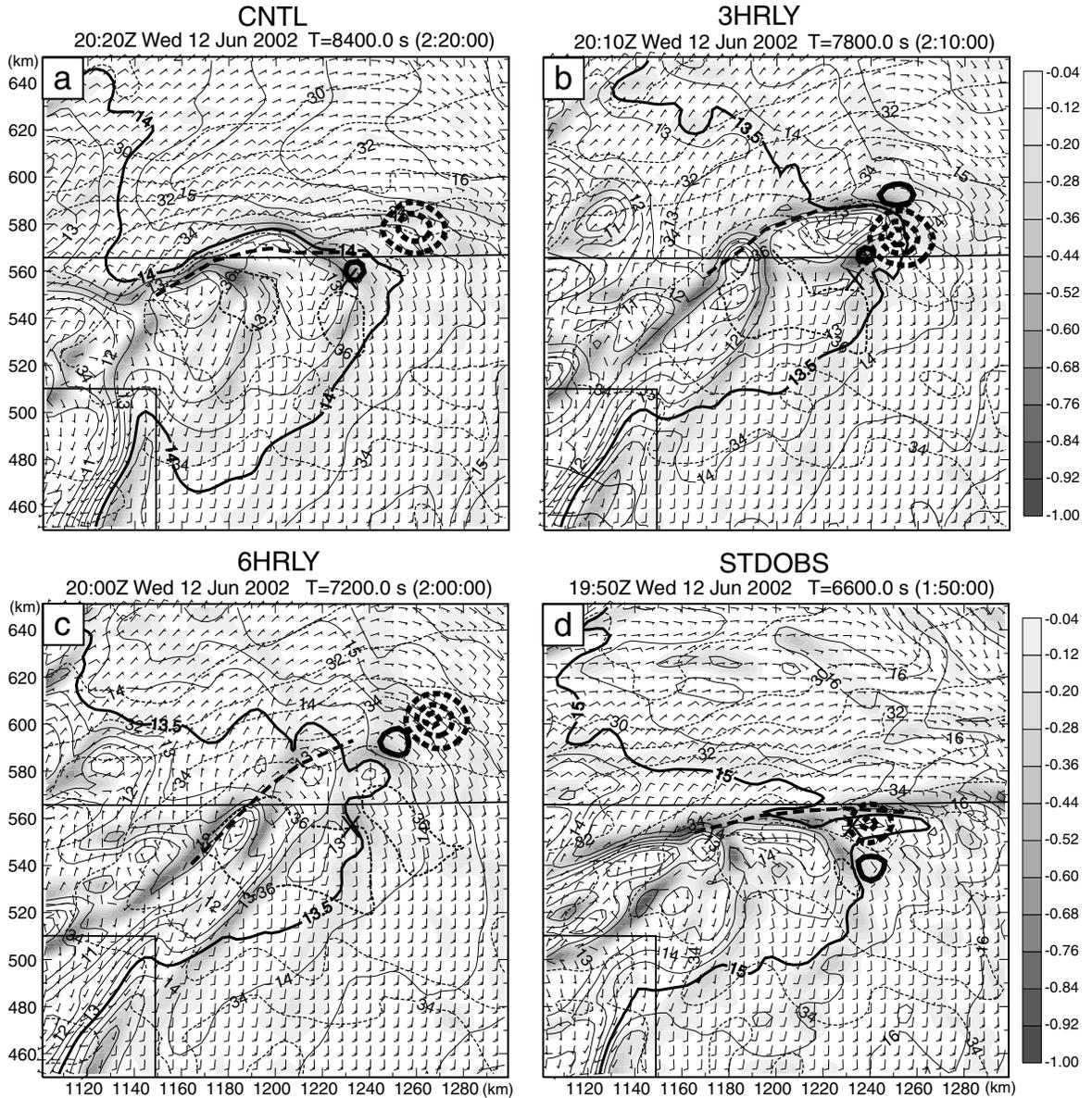
Fig. 5.10. Surface fields of horizontal divergence (only negative values shown in shaded gray), specific humidity (thin solid contours with 14, 13.5, 13.5 and 15 g kg⁻¹ contours highlighted by thicker lines in a, b, c and d, respectively), temperature (thin dashed contours with 36° C contours highlighted by thicker lines) and the 0.1 g kg⁻¹ contour of total condensed water/ice (bold solid contours) for experiments CNTL at 2020 (a), 3HRLY at 2010 (b), 6HRLY at 2000 (c) and STDOBS at 1950 (d), 12 June, 2002, which correspond to the times of first cloud formation in the experiments. The bold dashed contours are for composite reflectivity (10 dBZ intervals starting at 10 dBZ) when it first appears out of the initial clouds, at 2130, 2050, 2050, 2040 for the four experiments, respectively. The main wind shift or shear line associated with the outflow boundary is indicated by a thick dashed line in each plot. The location of observed CI4 is marked by an 'X' symbol.

similar to each other (Fig. 5.10b and Fig. 5.10c). For CNTL and STDOBS, the line of strong wind shift between southerly flow ahead of and the easterly or northeasterly flow behind the outflow boundary is located near OK-KS border, in a east-west orientation, while those in 3HRLY and 6HRLY are in a more northeast-southwest orientation, located further north. It is believed that the hourly assimilation cycles helped improve the low-level flow analysis in CNTL and STDOBS.

The wind shift or shear line corresponds to a zone of enhanced convergence. South of this shear line in the generally southerly flow, fine-scale convergence bands are clearly evident in all 4 experiments, with the orientation more or less parallel to the low level winds. These bands are associated with boundary horizontal convective rolls and eddies; the interaction of these bands can create localized convergence maxima that form preferred locations of convection initiation (XM06b) Apparently, in all four cases, the first cloud (indicated by the bold solid contours in Fig. 5.10) is found directly over or very close to the localized convergence maximum (spots of enhanced gray) that is closest to the warm and moist air coming from the south or southeast. The convergence maxima located further west or north do not trigger convection as early or not at all because of lower values of low-level moisture and/or temperature there.

The location of first cloud in CNTL almost exactly coincides with the observed first echo (marked by '**x**' in Fig. 5.10) while the first clouds in the other three experiments are located within 30 km of this location. The ensuing first echoes developed at different rates, with that in CNTL being the slowest (taking 70 minutes until 2130), and those in the others taking 40 to 50 minutes. In CNTL, 3HRLY and 6HRLY, the first echoes are found to the northeast of the corresponding first clouds,

while that in STDOBS is found to the north of the first cloud. These relative locations indicate the direction of cloud and cell propagation, which is to a large degree controlled by the horizontal winds that advect them. The complexity of the first cloud formation and the subsequent development of the first echo, in terms of the location relative to the primary outflow boundary convergence and maximum convergence centers due to boundary layer convective activities, suggest a degree of randomness.

As discussed earlier, among experiments CNTL, 3HRLY, 6HRLY and STDOBS, the initiation of CI4 occurring the earliest in STDOBS, at 2040, 20 minutes earlier than observed while that in CNTL occurred 30 minutes later than observed at 2130. Such timing differences can be explained by the fact that the surface relative humidity at the time of first cloud is the highest in north-central OK in STDOBS (Fig. 5.10), which has values of around 15 g kg^{-1} in the region (Fig. 5.10d) while in other cases the values are between 13 and 14 g kg^{-1} (see the highlighted dark contours in the plots). The surface temperatures in the region are much closer, all around 36 C°. Because CNTL, 3HRLY, 6HRLY assimilated Oklahoma Mesonet data (Brock and Fredrickson 1993; Brock et al. 1995), which enjoy good data quality, surface analyses using them should be more reliable than those from STDOBS. Another reason that the low level air of STDOBS is believed to be too moist is that there was some spurious light precipitation around 1800 in STDOBS in southwestern OK (not shown); the advection of moistened air would result in higher low level moisture in north-central OK. Therefore, the apparent better timing of CI4 initiation is not necessarily for the right reason.

5.5.2 Effect of vertical correlation scales in ADAS on the analysis and prediction of the cold pool

The outflow boundary created by the earlier MCS played an important role in this case, in helping initiate cell groups 4 and 5 and in the later organization of convection into a squall line. Earlier studies have shown the importance of properly initializing a cold pool for mesoscale prediction (Stensrud and Fritsch 1994; Stensrud et al. 1999). In our case, the ARPS Data Analysis System (ADAS) is used to analyze the surface and other observations. The ADAS is based on the Bratseth (1986) successive correction scheme and analyzes observations using multiple iteration passes. The spatial correlations scales of observations are empirically specified and usually change with data sources and iterations (Brewster 1996). Theoretically, spatial correlation scales should be based on flow-dependent background error covariance but such covariance is generally unavailable at the mesoscale. Because the choice of correlation scales is empirical, the impact of the choices should be investigated. For the analysis of cold pool, the vertical correlation scale is of particular interest.

The horizontal and vertical correlation scales used in CNTL and other experiments (except for ZRANGE) are listed in Table 5.3. The choice of these correlation scales is based on additional experiments performed after the study of XM06, for the 24 May, 2002 case that focuses on convection initiation along a dryline; these values differ somewhat from those used in XM06. For the analysis of the cold pool behind the outflow boundary, the vertical scales ranging from 50 to 500 m used in CNTL appear too small for the surface data to properly reconstruct the cold pool, because too shallow a cold pool results. In experiment ZRANGE, larger vertical

correlation scales of 800, 400, 300, 200 and 100 meters are used for the five successive passes. This results in a deeper vertical influence of surface observations and hence a deeper analyzed cold pool, as shown in Fig. 5.11 by the comparison of vertical cross-sections from CNTL and ZRANGE, in northeast OK along a line roughly normal to the outflow boundary (as indicated in Fig. 5.5d). It is clear from Fig. 5.11 that the analyzed cold pool is deeper in ZRANGE (Fig. 5.11b v.s. Fig. 5.11a), and is maintained longer in the forecast, as seen from both of its depth and horizontal extent (Fig. 5.11c through 10f). The deeper cold pool in this region helped create a strong convergence further west along the outflow boundary as the cold air is advected west-northwestwards (c.f., Fig. 5.5), resulting in a somewhat earlier and better timing of the initiation of cell group 4 (Table 5.2) than in CNTL.

However, this set of larger vertical correlation scales did not lead to a better prediction of the initiation of all of the other cell groups, nor of the general evolution of convection. This suggests that the increased vertical correlation scales do not necessarily improve the analysis in other regions outside the cold pool. For truly optimal analysis, flow-dependent background error correlation scales have to be estimated and used. Such flow-dependent statistics will require more sophisticated assimilation methods such as the ensemble Kalman filter (Evensen 1994).

5.5.3 Impact of lateral boundary locations

For limited area simulation and prediction, the location of the lateral boundaries and the specification of lateral boundary conditions have a significant impact (Warner et al. 1997). In this study, the lateral boundary conditions are obtained from the Eta realtime analyses at 6 hour intervals, and from interleaved 3-hour forecasts. They are
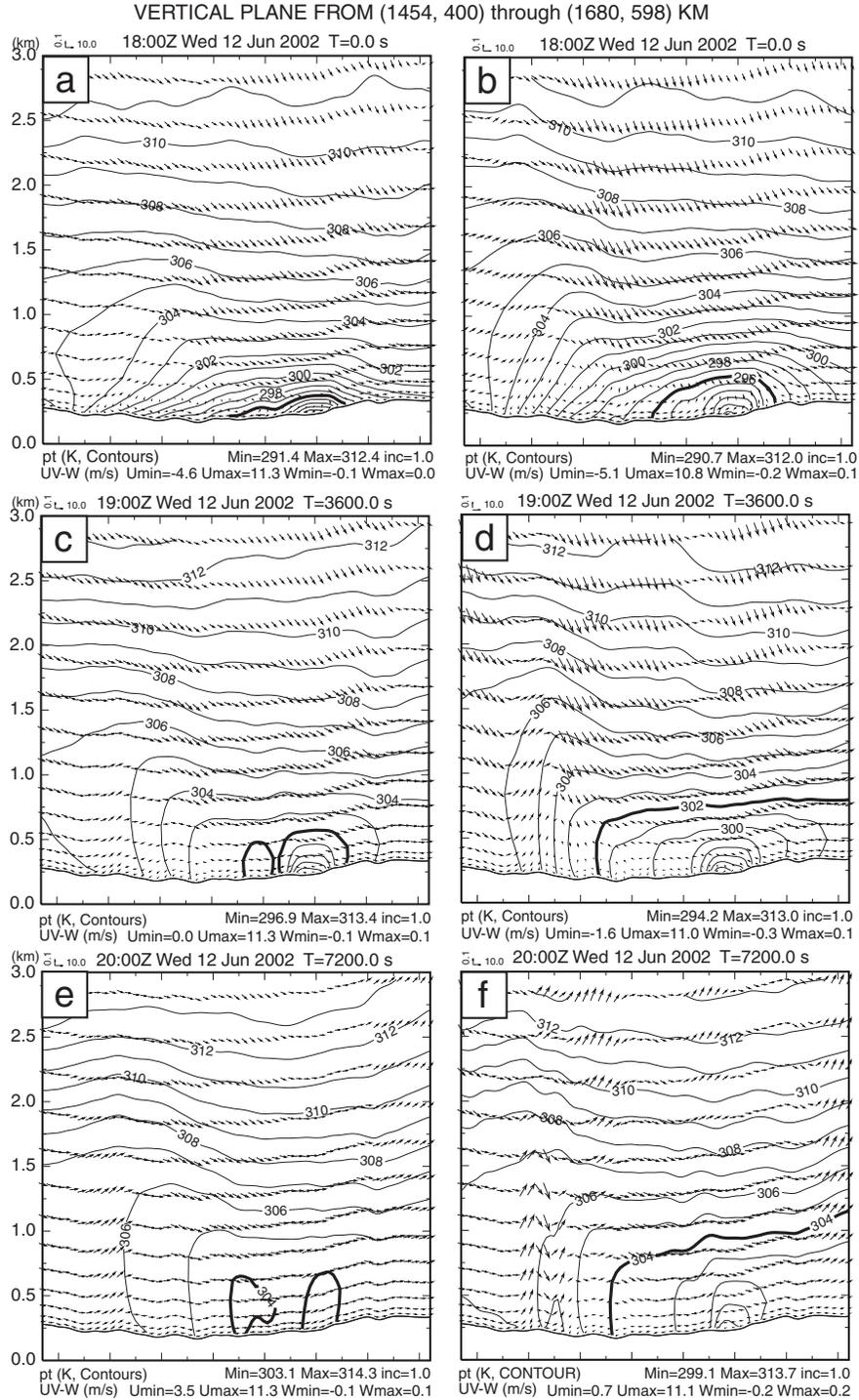
Fig. 5.11. Vertical cross-sections of potential temperature and wind vectors projected to the cross-section, through points (1454, 400) and (1680, 598) km, as indicated by the thick straight white line in Fig. 5.5d, at 1800 (upper panel), 1900 (middle panel) and 2000 (lower panels), for experiments CNTL (left panels) and ZRANGE (right panels). Certain characteristic contours are highlighted as bold to facilitate comparison.

linearly interpolated to the model time levels and spatially interpolated to the 3-km resolution grid. In 2002, the horizontal resolution of the operational Eta forecasts was 12 km and the data used in this study had been interpolated to a 40 km grid with 39 pressure levels before downloading from NCEP. For the experiments reported earlier, a rather large computational domain, as shown in Fig. 5.4, is used. This choice was based on some initial experiments where sensitivity to the lateral boundary location was found. In this subsection, some of the sensitivities of CI and later evolution of convection to the boundary location are documented.

In general, the upstream boundary conditions have the most significant impact on model simulation or prediction. In our case, there exists a significant flow response to the day time heating over the sloping terrain in the TX panhandle area. Between 1200 and 1800, the flow ahead (east) of the dryline turned from south-southwesterly into south-southeasterly, as a response to the elevated heating and to the tightening mesoscale low circulation in the OK panhandle (c.f., Fig. 5.5). In our initial experiments, a smaller domain was used, as shown by the box in Fig. 5.4. With this smaller domain, the western boundary is located just west of the NM-TX border and the southern boundary is about 200 km north of the larger domain boundary. In experiment SML (Table 5.2), the same configurations, including the assimilation cycles, as CNTL are used, except for the use of this smaller domain. In this case, the westerly winds behind the dryline are found to be too strong (which mostly came from the lateral boundary condition), and the upslope acceleration east of the dryline is too weak, causing the dryline to propagate too far to the east. Consequently, the storms along the southern

portion of the dryline also propagated too far to the east (Fig. 5.12). The too weak upslope flow was related to the fact that the southern boundary was located within the region of flow response. A separate experiment in which the southern boundary alone was placed further south, to a location similar to that of CNTL, a much stronger upslope response was obtained (not shown). The strong westerly winds behind the dryline in SML also enhanced the convergence along the dryline, resulting in earlier initiation of cell groups 1a and 2 (Table 5.2 and Fig. 5.12a) than in CNTL. The initiation of group 3 was affected by the too far eastward propagation of cell group 2 (Fig. 5.12b).

To see if the upslope flow was a response to the elevated heating or to the dryline convection, we performed an alternative experiment to CNTL, in which the moist processes were turned off. In that case, the upslope flow response was found to be as strong as in the moist case, suggesting that convective heating did not play a major role.

The location of the eastern boundary of the model also affects our simulations in a significant way, especially in terms of the winds in northeast OK, northwest AR and southeast KS that are associated with the cold outflow from the MCS passing through that region earlier in that day (see Introduction). When the eastern boundary is located just east of the OK-AR border in SML, a strong southeasterly component of winds through the OK-AR border into the northeastern OK region is maintained into the later period of simulation (Fig. 5.12b,c,d), which actually verified well against OK Mesonet data (not shown). This southeasterly flow is maintained a result of spreading cold outflow from the MCS in AR. This particular feature is not handled well in all experiments that use the larger domain; in fact, a slightly westerly wind component

develops early in all the simulations (e.g., Fig. 5.6) and persists in northeast OK and

southeast KS. This deficiency is at least partly responsible for the poor organization of
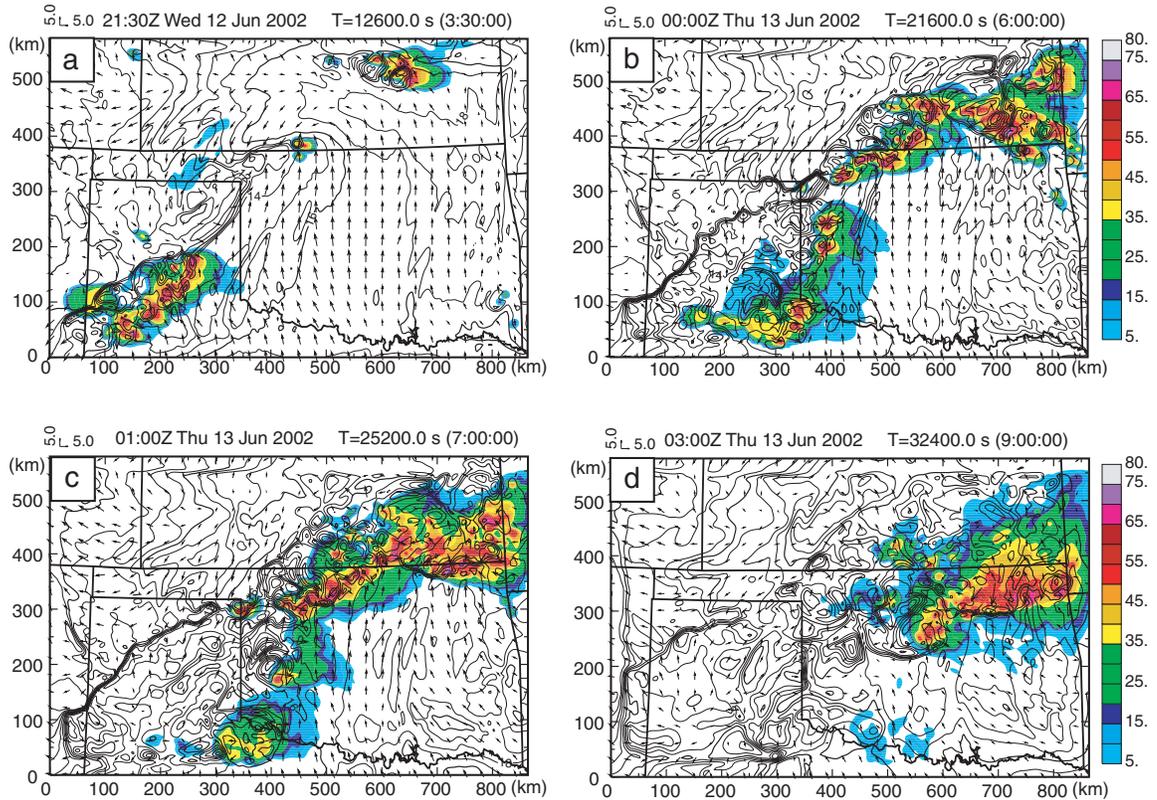
Fig. 5.12. As Fig. 5.6 but for small-domain experiment SML, at (a) 2130, (b) 0000, (c) 0100, and (d) 0300, 13 June, 2002.

convection at the later stage of forecast in CNTL (Fig. 5.6) and for the generally

northeastward dislocation of convection (c.f. Fig. 5.6d and Fig. 5.3d). Actually, in SML,

despite the much poorer evolution of the earlier convection starting from the dryline

(which should have mostly dissipated by 0100 anyway, c.f. Fig. 5.3d), the prediction of

convective organization into a squall line is actually better reproduced (compare Fig.

5.12d with Fig. 5.6d and Fig. 5.3d). The southeasterly inflow forced in from the eastern

boundary against the convective outflow associated with the squall line is believed to have played a role in this.

In most cases, a larger high-resolution domain is preferred. However, in this case, the MCS that passed through southern KS, northeastern OK into AR was not represented in the model; hence the model, despite its high resolution, was incapable of correctly reproducing the later southeasterly flow. In SML, the use of analysis boundary conditions from Eta helped capture this feature, resulting in a better prediction of convection in this region at the later time.

5.6 Summary

The non-hydrostatic ARPS model with 3-km horizontal resolution is used to numerically simulate the 12-13 June 2002 case from the IHOP_2002 field experiment that involved initiation of many convective cells along and near a dryline and/or outflow boundary. The ARPS Data Analysis System (ADAS) is used for the data assimilation. The initial condition of the control experiment is generated through hourly intermittent assimilations of routine as well as non-standard surface and upper-air observations collected during IHOP_2002 from 1200 to 1800. The model is then integrated for 9 hours, spanning the hour before the first observed convection initiation along the dryline through the mature stage of a squall line organized from a number of initiated cells. The forecast domain is chosen large enough to minimize any negative effects from the lateral boundary.

As verified against multi-radar composite reflectivity fields, the model reproduced most of the observed convective cells with reasonably good accuracy in

terms of the initiation timing and location, and predicted well the general evolution of convection within the first 7 hours of prediction. Detailed characteristics they were captured by the model include cell splitting, merger and regrouping, and the triggering of secondary convective cells by new outflow boundaries colliding with a pre-existing boundary. The main deficiencies of the prediction are with the organization of cells into a squall line and its propagation, during the last 2 hours of the 9-hour forecast, and the mostly delay in the initiation timing.

Sensitivity experiments were performed to examine how the data assimilation intervals and non-standard observations influence the prediction of convection initiation and evolution. The results show that the experiment with 3-hourly assimilation cycles provides the best CI prediction overall while control experiment with hourly assimilation intervals predicts the best convective evolution. The CI in the control experiment is delayed in general, insufficient spatial resolution and the typically damping effect on the forced ascent in the high-resolution forecast background when assimilating data that contain only mesoscale information are suggested to be the causes. The apparent improvement to the timing of some of the CI in the experiment that did not include non-standard data is suggested to be due not necessarily to a better initial condition, but rather to the cancellation of resolution-related delay and the too moist initial condition at the low levels.

The vertical correlation scales used in ADAS which employs multi-pass successive corrections are shown to significantly impact the structure of the analyzed cold pool using surface observations. Larger vertical correlation scales resulted in a deeper cold pool that lasted longer, leading to stronger convergence and earlier

initiation at the outflow boundary. Truly flow-dependent background error covariances will be needed to provide the best information on how the surface observation information should be spread in the vertical.

When the western boundary of the model grid was placed close to the southwest end of the dryline, apparently too strong westerly flow initiated convection at the dryline earlier, and helped push the convective cells too far to the east. When the southern boundary of the model grid is placed not far enough south, the upslope flow response east of the dryline is constrained significantly, reducing the easterly flow component needed to slow down the eastward propagation of the dryline and related convection. When the eastern boundary is placed near the Oklahoma-Arkansas border in order to bring in observed information of the spreading cold pool from the earlier mesoscale convection in Arkansas, the information helped improve the prediction of flow ahead of an organizing squall line later into the prediction, hence leading to a better organized squall line.

Chapter 6
Impact of GPS *SWV* data on the Prediction of Convection initiation and Precipitation

6.1 Introduction

The cost effective ground-based GPS receiver network has been deployed in recent years. There exist a number of studies on the impact of the GPS data on mesoscale numerical weather prediction. The high spatial and temporal resolutions of the water vapor measurements possible with the GPS network have proven to be beneficial for precipitation forecast. For example, the short-term precipitation forecast can be improved by assimilating surface humidity and *PW* data into a mesoscale model (Kuo et al. 1996). De Pondeca and Zou (2001) demonstrated that assimilating real *ZTD* data together with profiler wind observations into a mesoscale model significantly improve the prediction of the 6- and 12-hour accumulated rainfall over southern California. Moreover, assimilating GPS PW also has potential to better retrieve the orographic rainfall (Falvey and Beavan 2002). All these studies concentrate on the improvement of rainfall prediction, generally at relative coarse resolutions. The objective of our study documented in this chapter is to investigate the impact of GPS slant-path water vapor (*SWV*) data on the prediction of convection initiation (CI) at few

kilometer horizontal resolutions, as well as their impact on subsequent precipitation, using the 3DVAR analysis method developed in the earlier chapters.

The exact timing and location of the first initiated storm during summer are hard to predict. One of the reasons for this difficulty is our poor knowledge of three-dimensional moisture distribution due to its high variation over time and space. It has been shown that the storm initiation is sensitive to the moisture amount (Lee et al. 1991). Ziegler and Rasmussen (1998) also demonstrated that it is essential for the development of deep moist convection that the moist boundary layer air parcels reach their lifted condensation level (LFL) and level of free convection (LFC) prior to leaving the mesoscale updraft zone. The moisture at the surface is a key factor in determining both LFL and LFC of air parcels according to the parcel theory. Meanwhile, Crook (1996) studied the sensitivity of storm initiation and the subsequent strength to the surface temperature and moisture as specified by a single sounding. He demonstrated that the surface temperature is the first factor to influence storm initiation while the storm strength is most sensitive to the surface moisture. Therefore, a better knowledge of moisture amount and distribution should help improve the prediction of deep moist CI and its precipitation.

Recently, studies have demonstrated that the use of integrated slant-path water vapor *(SWV)* data from ground-based GPS network can better characterize the three-dimensional moisture structure (MacDonald et al. 2002; Liu and Xue 2006; Liu et al. 2007). It is also recognized by the IHOP_2002 field experiment that GPS is a good platform for improving the measurement and understanding of four-dimensional water vapor distribution (Crook 1996; Fabry 2006). In this chapter, we further examine the

impact of GPS *SWV* measurement, through OSSEs, on the prediction of the initiation and subsequent evolution of storm convection.

In subsection 6.2, a set of 3D moisture analysis experiments using simulated GPS *SWV* data is described. The 3 km control forecast from Chapter 5 for the June 12, 2002 convection initiation case is used as the truth. The analyzed water vapor fields are then used to initialize the ARPS model forecasts. The analysis and forecast results are presented in subsection 6.3. Discussions on the results and a summary are given in subsection 6.4.

6.2 Experiment design of moisture analysis and storm prediction

We continue to employ OSSEs in this chapter due to the lack of real GPS observations with high enough temporal and spatial resolution in storm-scale. Compared to the OSSEs presented in Chapters 3 and 4, we take one step further by using the analyzed moisture fields in the model initial condition and examine the impact of such analysis on the model forecast.

The 3DVAR method with recursive filter developed in Chapter 4 is utilized in this study. The analysis is performed on the 3 km grid. The coarser resolution analysis coming from the operational Eta model is interpolated to 3 km as the analysis background. The forecast of the 3-km CNTL experiment presented in Chapter 5 is considered as the 'truth' from which GSP *SWV* and surface observations are sampled. In the OSSEs, the horizontal resolution of ground-based GPS receiver stations is assumed to be 60 km, i.e., we assume that there is one receiver station every 20 grid points at the

surface. The analysis domain is about 2400 km x 960 km, so the total number of receivers is 697 (41 × 17). As we assumed in Chapter 4, we continue to assume 9 GPS satellites in view at any ground receiver station for the OSSEs here even though the number of analysis grids is much larger (800 × 320 × 50 vs 46 × 41 × 40). Fig. 3.2 in Chapter 3 shows a schematic to illustrate the hypothetical ground-based GPS observation network used. The total number of slant paths is 6273 (697 × 9). The GPS *SWV* observations are simulated as in Chapter 3, according to Eq. (3.5).

As in Chapter 4, the observations to be analyzed include the *SWV* from ground-based GPS receivers and the moisture data at the surface obtained from moisture measurement instruments collocated with GPS receivers. As mentioned in Chapter 4, the realistic observation errors for these two kinds of data have zero mean with Gaussian distribution. The standard error deviations are 5% and 7% respectively for surface moisture and *SWV* data. The weights of the background, the GPS observation and the surface moisture observation terms are specified respectively according to the inverse of their error variances. The non-negative-water-vapor weak constraint is given a weight of 50 based on our previous study in Chapter 4. According to the receiver resolution used in these OSSEs, the horizontal de-correlation length scale is specified as 40 grid intervals. The vertical de-correlation length is set as 6 in terms of grid points. The parameter to control the degree of anisotropy, L_f in Eq. (4.8) is specified as 3.0 g kg^{-1} in terms of mixing ratio based on the sensitivity study performed in Chapter 4.

It is worthy pointing out again that the total number of grid points is 1.3×10^7 (800 × 320 × 50) in this set of OSSEs while it is about 8×10^4 (46 × 41 × 40) in those conducted in Chapters 3 and 4. Because much more grid points are involved in these

OSSEs, there are a few additional issues related to the large number of grid points. For such OSSEs, it is impossible to store the anisotropic background error at every grid point as we did in Chapter 3 using explicit filters due to the typical single-node computer memory limit. But there is no such a problem if we use recursive filters to model anisotropic background error covariance. However, the memory requirement is still very large. Secondly, it is more difficult for the minimization to converge, i.e., the cost function decreases slowly. This is because more grid point values have to be simultaneously adjusted to fit the observations to a given accuracy. Thus, the iteration number to consider as minimization convergence is increased for this set of OSSEs to 500 from the previous 100. When the iteration stops at 500, the magnitude of the total cost function is reduced 2 orders.

In the OSSEs, the moisture field in the initial condition of the 'truth' forecast is replaced by analyzed moisture field. Three forecasts are initialized with such moisture fields. All forecasts start from 1800 UTC 12 June 2002, and are run for 9 hours. These forecasts are respectively called experiments qvGPS_ISO, qvGPS_ANISO and qvGPS_UB (Table 6.1). The name qvGPS denotes that the model initial moisture is retrieved from GPS data. The suffixes (ISO, ANISO and UB) in the names indicate if the GPS data are analyzed with isotropic, truth-based anisotropic filters or anisotropic filters based on the updated background error field. These suffixes are used in the same way as in Chapter 4. The Eta moisture analysis interpolated to 3 km is also used to substitute the moisture initial condition of 'truth' to perform the fourth 9-hour forecast, called experiment qvETA (Table 6.1), to provide a baseline for comparison purpose.

The forecast model is the version 5 of ARPS (Xue et al 2000, 2001, 2003), same as used in Chapter 5 for the truth simulation. The model configurations are the same as those used by CNTL experiment in Chapter 5. Basically, the model is non-hydrostatic with generalized terrain-following coordinate and vertical grid stretching. The model terrain and land surface characteristics are created using U. S. Geological Survey 30-s terrain and surface dataset. The lateral boundary condition comes from time interpolations of 6-hourly Eta analyses and 3-hour forecasts in between the analyses. The model is used in its full physics mode. Other configuration settings can be found in section 5.3.

Forecast experiments	Experiment description		CI timing (UTC)	
			CI2	CI4
qvETA	Moisture initial condition from Eta analysis		2040	2000
qvGPS_ANISO	Moisture initial condition from 3DVAR analysis using GPS *SWV* and surface moisture data	Anisotropic **B** based on true background error	2040	2030
qvGPS_ISO		Isotropic **B**	2040	2150
qvGPS_UB		Anisotropic **B** based on isotropic analysis	2040	2040
'Truth'			2040	2130

Table 6.1 List of the experiments and their descriptions as well as the timings of CI2 and CI4.

6.3 Results

Only the moisture initial conditions are different among the forecast experiments, hence we will first look at the moisture analyses. The comparison is performed among the 'truth' moisture field, the Eta-interpolated moisture which serves as the analysis background and the 3DVAR analyzed moisture fields. A careful examination on the

forecast results is performed subsequently to see how the initial moisture differences influence the forecast.

6.3.1 Moisture analysis

Because we are mainly interested in the Central Great Plains region centered in Oklahoma in which the dryline convection initiation and the later evolution occurred, we will only plot a portion of the analysis domain. The 'truth' and the Eta background moisture fields at the surface are shown in Fig. 6.1a and Fig. 6.1b, respectively. The 'truth' moisture contains mesoscale structures related to the cold pool, dryline, and the structures due to boundary layer convective eddies. It is easy to see in the 'truth' field a dryline extending from eastern OK panhandle to western TX panhandle with a northeast-southwest orientation and the dryline is stronger than that in the Eta background. Moreover, the background is drier inside the state of Oklahoma while it is more moist in the TX panhandle region in general than the 'truth'. Near the northeastern corner of Oklahoma, a minimum moisture center indicates the location of a cold pool in both the background and 'truth'.

Shown in Fig. 6.2 are the moisture analyses at the surface derived from GPS *SWV* and surface moisture observations using the 3DVAR method with the anisotropic background error structures derived from the 'truth' (ANISO, Fig. 6.2a) and with the isotropic background error (ISO, Fig. 6.2b). Fig. 6.2c shows the surface moisture analysis which uses a 2-step iterative procedure in which a trial analysis is first performed using isotropic background error and the analysis is then used to estimate the
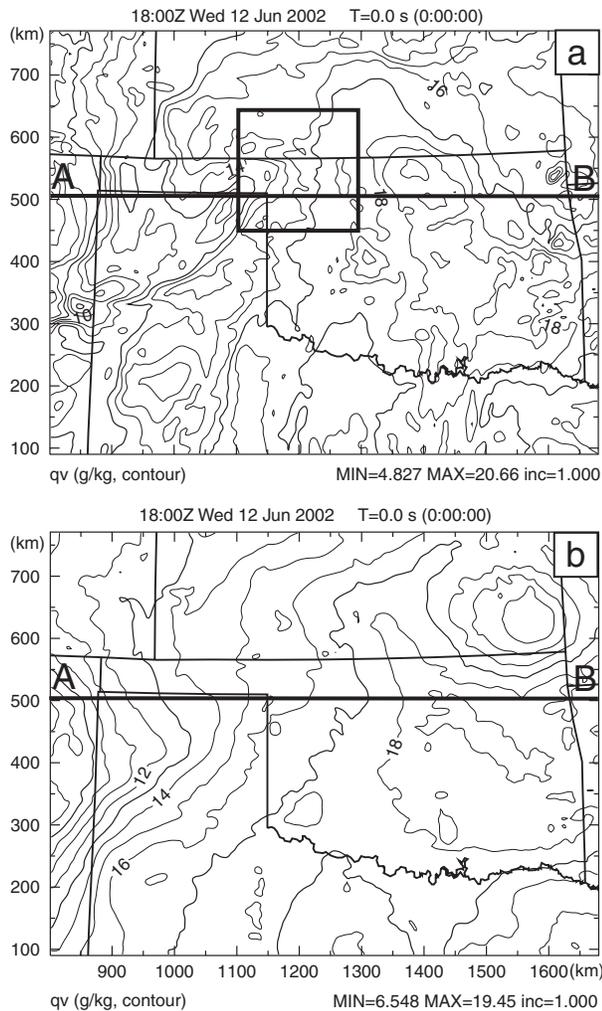
Fig. 6.1 The specific humidity field at the surface from (a) the 'truth' and (b) the analysis background at analysis time 1800 UTC. The thick black line AB denotes y = 505.5 km. The black square denotes the plotting domain shown in Fig. 6.11.

anisotropic background error structures in the second anisotropic analysis step. Here, UB in the experiment name implies the use of updated background error covariance estimate. Generally, all analyses improve the moisture distribution over the background with the use of *SWV* and surface observations. The analysis with the isotropic filter shows clearly a moist tongue extending northwestward from the southeast corner of Oklahoma to south central Kansas although the analyzed moist tongue is not as strong

as in the 'truth' (Fig. 6.1a). The dry tongue near Oklahoma panhandle is also resolved well in this analysis. The dryline structure can be identified in this analysis though the moisture gradient is not strong along the dryline.

The analysis with the updated background error is much improved (Fig. 6.2c). The moisture gradient along dryline appears stronger. The moist tongue extends further northwestward as suggested by the 19 g kg^{-1} isohume that extends further northwest. It is obvious that a dry air center near the eastern OK panhandle is present in the UB analysis but not in the ISO analysis. Among the three experiments, ANISO produces the best analysis (Fig. 6.2a) with more fine-scale moisture structures being recovered. The correlation coefficients (CC) between the analysis increment and the 'truth'-minus-background are 0.82, 0.77 and 0.75, respectively, for experiments ANISO, UB and ISO. These correlations actually reveal less difference among the analyses than the plotted cross sections in Fig. 6.2 indicate.

To understand how UB improves upon the analysis of ISO, we plot in Fig. 6.3 the 'truth' minus background (Fig. 6.3a) and the analysis increment of ISO (Fig. 6.3b). The former denotes the true background error while the latter indicates the pattern used to estimate the background error covariance in UB analysis. We can see that the ISO analysis increment shows a pattern similar to although smoother than the true background error. The use of this reasonably good estimate of the true error pattern apparently was beneficial in further improving the analysis in the second anisotropic analysis step.

146
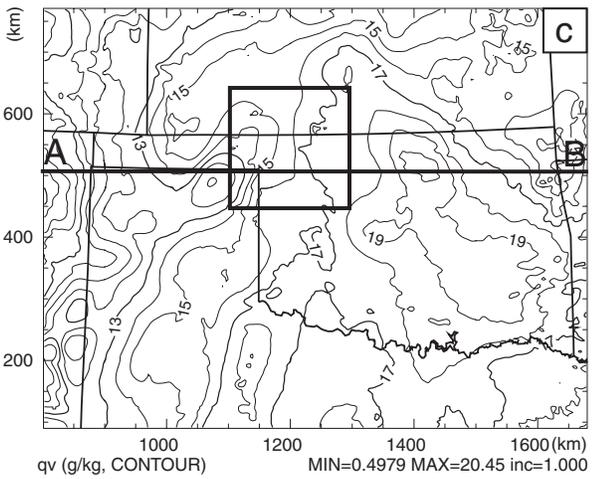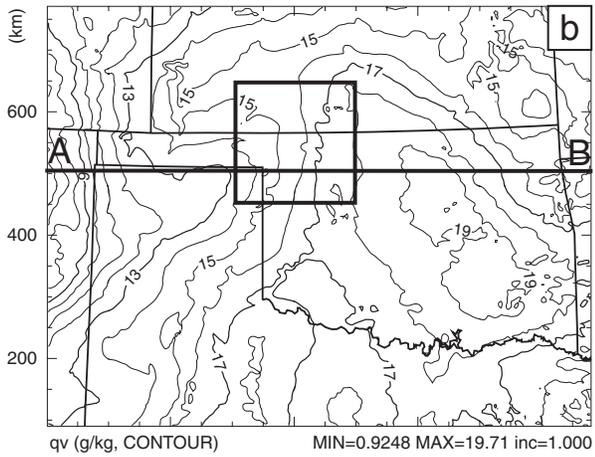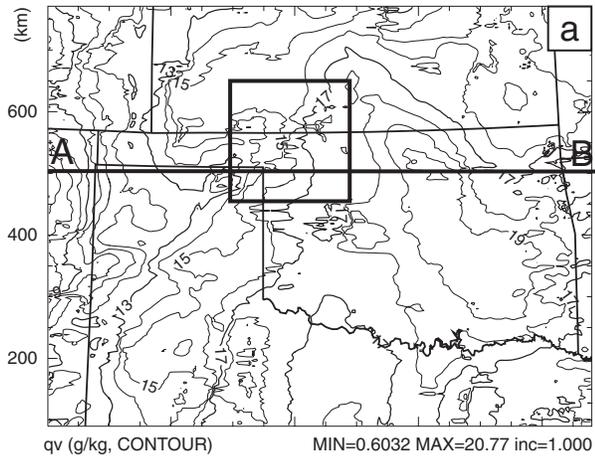
Fig. 6.2 The specific humidity analysis at 1800 UTC from (a) ANISO, (b) ISO and (c) UB at the surface. The thick black line AB denotes y = 505.5 km. The black square denotes the plotting domain shown in Fig. 6.11.

147
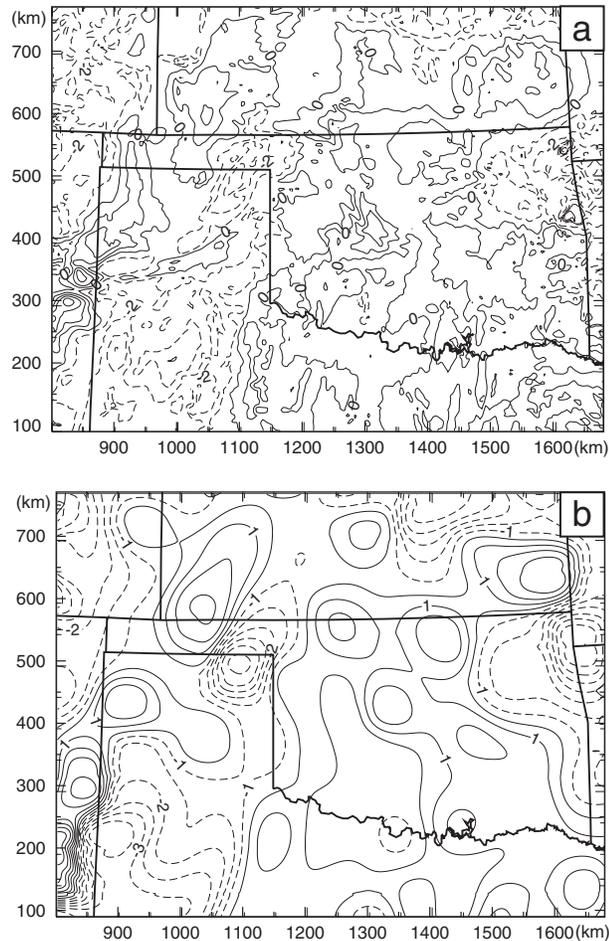
Fig. 6.3 (a) 'truth' minus background specific humidity and (b) the specific humidity analysis increment from the experiment ISO at the surface.

Shown in Fig. 6.4 are the east-west vertical cross-sections of specific humidity fields, for the truth, background and three different analyses, along $y = 505.5$ km which cuts through the dryline, the moist tongue and the cold pool near the northeastern corner of Oklahoma (see the thick black line AB in Fig. 6.1 and Fig. 6.2). A few structures found in the 'truth' field (Fig. 6.4a) either look quite different or are missing in the background (Fig. 6.4b). The first of such structures is the very dry air in the lower to middle troposphere (from 3 km to 6 km) between $x = 1000$ km and $x = 1200$ km caused by the approaching cold front. The second is the dryline structure as indicated by the

148
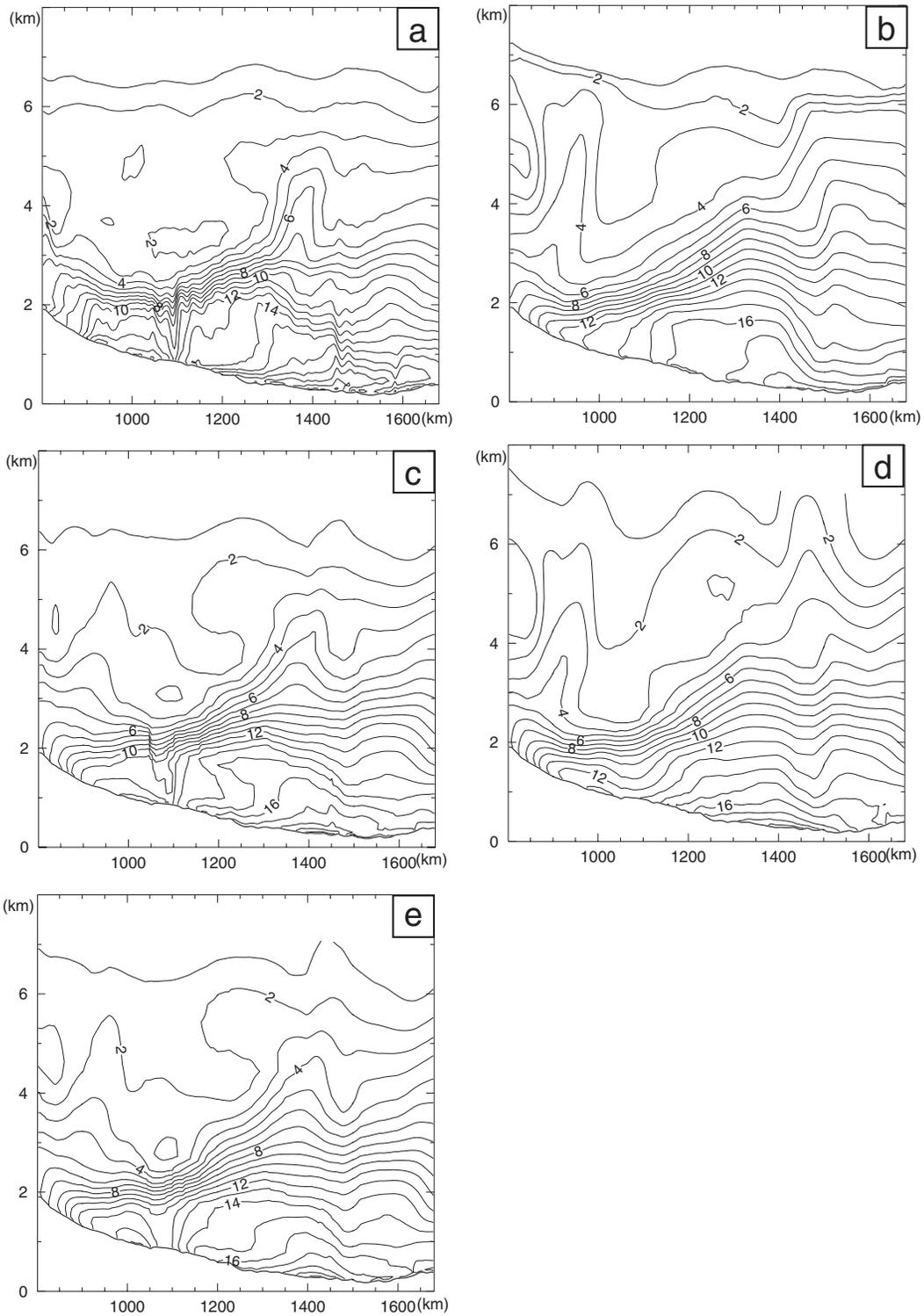
Fig. 6.4 The east-west vertical cross-section of specific humidity through y = 505.5 km from (a) the 'truth', (b) the background Eta analysis and the 3DVAR analyses (c) ANISO, (d) ISO and (e) UB at 1800 UTC.

almost vertically oriented moisture isohumes near $x = 1100$ km. The third is the moist tongue extending from the surface to about 5 km height level which represents the moist region due to the low-level moisture transport by southeasterly winds. The fourth is related to the cold pool near the eastern boundary of the plotting domain. In the background (Fig. 6.4b), the isohume contours are not tight enough to show the advancing cold front and the dryline near $x = 1100$ km is more or less missing. The moist tongue near $x = 1400$ km is not obvious either. The air near the eastern plotting boundary is much more moist in the background than in the 'truth'.

The ISO analysis (Fig. 6.4d) is able to retrieve the dryline structure but not very well. However, the ANISO (Fig. 6.4c) and UB (Fig. 6.4e) analyses show very similar humidity pattern as the 'truth', including the successful representation of the cold front structure, dryline system, moist tongue and cold pool.

In summary, it is demonstrated that our 3DVAR system is able to produce rather accurate moisture analyses using the simulated GPS *SWV* data and surface moisture measurements at the ground receiver stations, and the results are improved when flow-dependent background error covariance is modeled based on estimated background error structures. This is consistent with the findings reported in Chapters 3 and 4, except that the data and analysis resolutions are much higher here and the case examined is different. In the next section, we will examine the impact of these analyses on the forecast.

6.3.2 Convection initiation and precipitation prediction

Within the plotting domain, multiple storms are initiated in the 'truth' forecast. Two types of convection initiation (CI) are found in this case. One is associated with

strong low level mesoscale forcing while the other lacks such forcing. The cell group 2 initiated at the intercepting point of a cold front and dryline in western TX (CI2 following the naming scheme of Chapter 5) obviously belongs to the first category (c.f., Fig. 5.6a). The convection near Oklahoma /Kansas border (marked as CI4 in order to be consistent with the naming scheme used in Chapters 5) is initiated east of the dryline and south of the MCS outflow boundary and is related to the interaction of the boundary layer convective rolls and eddies with a weak mesoscale convergence zone. Because of the lack of strong mesoscale forcing, it is more sensitive to the fine-scale moisture values and distribution. In contract, CI2 is less sensitive to the initial moisture field. Therefore, in this section, we will focus on the prediction of the CI4 in terms of its timing and location while briefly discussing CI2 and the precipitation of the entire system within the plotting domain.

As described in section 6.2, we performed four forecasts which serve to examine the impact of analyzing the *SWV* and surface moisture data on the prediction of storm initiation and precipitation. First, we look at the 'truth' and the forecast of qvETA, in which the moisture field in the initial condition at 1800 UTC is replaced by the Eta analysis valid at the same time. Fig. 6.5 shows the 'truth' composite reflectivity and specific humidity at the surface at the initiation times of CI2 and CI4, i.e., at 2040 and 2130 UTC. Fig. 6.6 shows the same fields at the same times but from experiment qvETA. It can be seen that there exist large differences in the reflectivity pattern between the 'truth' and qvETA. Care is needed, however, in interpreting these results. It is clear that qvETA has much more precipitation, as indicated by the reflectivity field, than the 'truth' at both times. This is mainly caused by the presence of nearly saturated
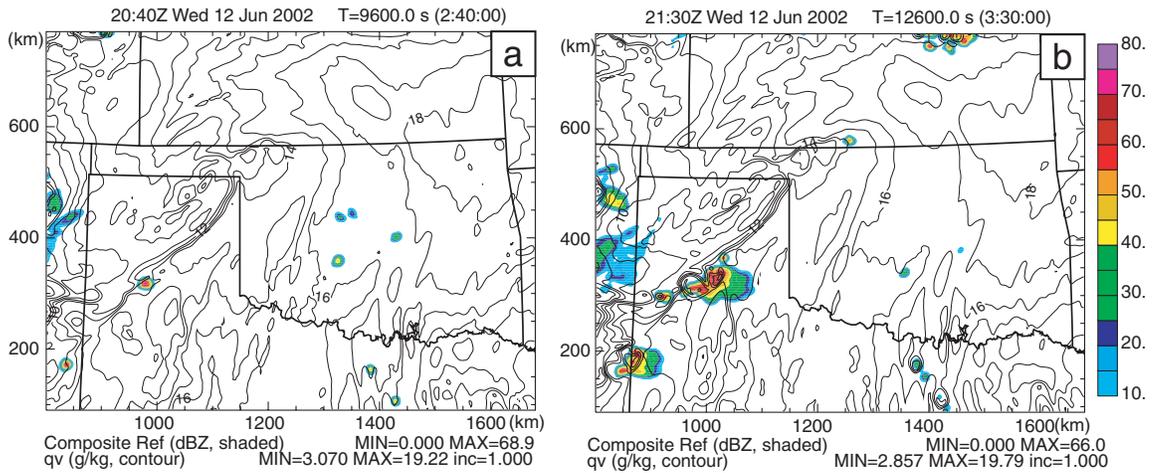
Fig. 6.5 The composite reflectivity and specific humidity at the surface from the 'truth' at (a) 2040 UTC and (b) 2130 UTC which are the convection initiation times for CI2 and CI4 respectively.
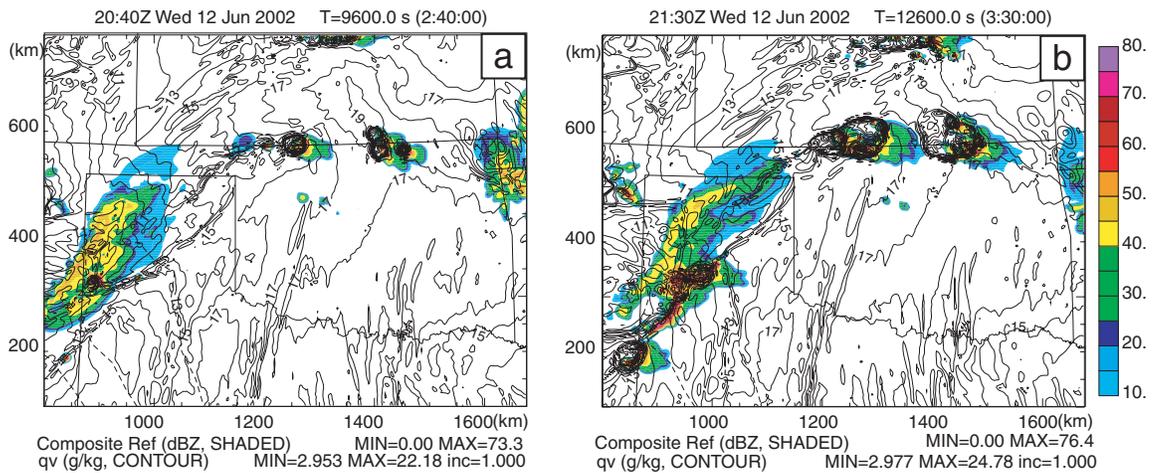
Fig. 6.6 Same as in Fig. 6.5 but from the experiment qvETA.

water vapor in the middle to high levels near the east part of the plotting domain in the initial condition of qvETA (Fig. 6.7). Fig. 6.7a plots the relative humidity contours larger than 0.8 in an east-west vertical cross-section which passes through the precipitation region at y = 550.5 km, from qvETA at 1800 and 1830 UTC and for the

'truth' at 1800 UTC. It can be seen that the water vapor near the east part of the domain is close to saturation in the Eta analysis and in the subsequent forecast of qvETA while the air in the same region is drier in the 'truth' initial condition. The higher initial moisture content in qvETA results in precipitation 10 minutes into the forecast and much more 30 minutes into the forecast (Fig. 6.7b). The precipitation reaches the ground by 1840 UTC (not shown). The precipitation there then continuously strengthens the existing cold pool (Fig. 6.1b) near the northeast corner of Oklahoma that is associated with the earlier MCS. The strengthened cold pool helps initiate more and earlier convective storms along the outflow boundary (Fig. 6.6a and b) than in the 'truth' (Fig. 6.5a and b), affecting CI4 also. The CI4 in the 'truth' is not triggered by strong surface convergence forcing at the outflow boundary while it is in qvETA in which CI4 is triggered at around 2000 UTC. Fig. 6.8 shows the surface wind vectors together with the specific humidity and composite reflectivity from qvETA at 2000 UTC, indicating strong wind convergence along the outflow boundary. At 2040 (Fig. 6.6a), the convection at CI2 location is initiated. This CI is not much affected in terms of its timing and location by the precipitation nearby which is caused by the nearly saturated layer of mid- to high-level moisture as well (not shown). The weaker sensitivity here is because this initiation is strongly forced by the cold front and dryline.

However, the convection initiation mechanism and precipitation pattern from the forecasts with the initial moisture fields obtained from our 3DVAR analyses are generally much more similar to the 'truth' (Table 6.1). Because most of the nearly saturated layer of water vapor in the Eta background is removed by the analysis, no precipitation is found to occur before 2030 UTC within our plotting domain in all of

(km) 0.1 5.0   18:00Z Wed 12 Jun 2002   T=0.0 s (0:00:00)
X-Z PLANE AT Y=550.5 KM

a

12

8

4

0

1000   1200   1400   1600(km)
RH (CONTOUR) MIN=0.1229E-01 MAX=1.000 inc=0.2500E-01
U-W (m/s) Umin=-10.82 Umax=36.34 Wmin=-1.16 Wmax=1.19

(km)   18:30Z Wed 12 Jun 2002   T=1800.0 s (0:30:00)
X-Z PLANE AT Y=550.5 KM

b

12

8

4

0

1000   1200   1400   1600(km)
Ref (dBZ, SHADED)   MIN=0.00 MAX=42.2
RH (CONTOUR)   MIN=0.000 MAX=1.000 inc=0.2500E-01
U-W (m/s)   Umin=-10.59 Umax=36.88 Wmin=-0.68 Wmax=2.46

80.
70.
60.
50.
40.
30.
20.
10.

(km)   18:00Z Wed 12 Jun 2002   T=0.0 s (0:00:00)
X-Z PLANE AT Y=550.5 KM

c

12

8

4

0

1000   1200   1400   1600 (km)
RH (CONTOUR) MIN=0.4945E-01 MAX=0.9979 inc=0.2500E-01
U-W (m/s)   Umin=-10.84 Umax=36.31 Wmin=-1.16 Wmax=1.07

Fig. 6.7 The relative humidity (contour) larger than 0.8 with contour interval 0.025, reflectivity (dBZ, shaded) and wind vector (m s^{-1}) at east-west vertical cross-section along y = 550.5 km from qvETA at (a) 1800 and (b) 1830 UTC and (c) from "truth' at 1800 UTC.

these forecasts. Shown in Fig. 6.9 are the forecast results from experiments qvGPS_ANISO and qvGPS_UB at 2030 and 2040, respectively the times of CI4 initiation in these two forecasts. Both predict CI2 that matches the 'truth' (Fig. 6.5a)

154

very well in terms of timing and location. But there are differences in the prediction of

CI4. In the subsequent discussion, because the forecast of qvETA differs significantly

from the 'truth' and from the other forecasts because of the presence of the mid- to

high-level nearly saturated moisture, we focus on comparing the forecasts with our

3DVAR moisture analyses with the 'truth'.
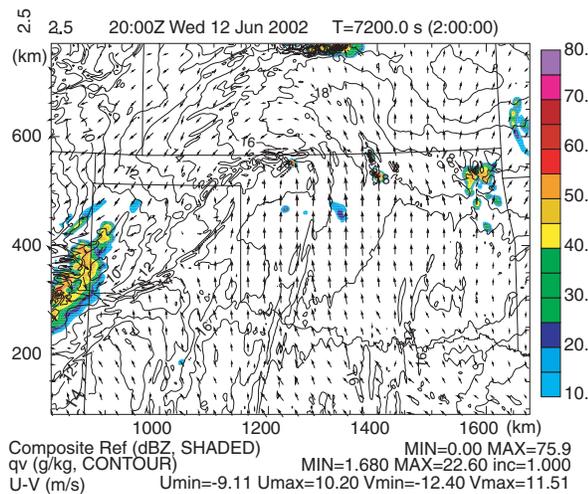
Fig. 6.8 The surface wind vector (m s^{-1}), specific humidity (g kg^{-1}, contour) and
composite reflectivity (dBZ, shaded) from qvETA at 2000 UTC.

Experiment qvGPS_ANSIO produces the earliest CI4 (Fig. 6.9a) at 2030 UTC

which is one hour earlier than the 'truth' (Fig. 6.5b). The CI4 in qvGPS_UB (Fig. 6.9b)

is 10 minutes later than that in qvGPS_ANISO. However, the first echo larger than 10

dBZ in qvGPS_ISO (Fig. 6.10c) occurs at around 2150 UTC which is 20 minutes later

than in the 'truth' (Fig. 6.5b). The initiation location is generally further south-

southwest if the initiation timing is earlier (as in qvGPS_ANISO and qvGPS_UB, Fig.

6.9) but further north-northeast when the initiation is late (as in qvGPS_ISO, Fig. 6.10c).

Because these three runs have exactly the same initial condition as the 'truth' except for
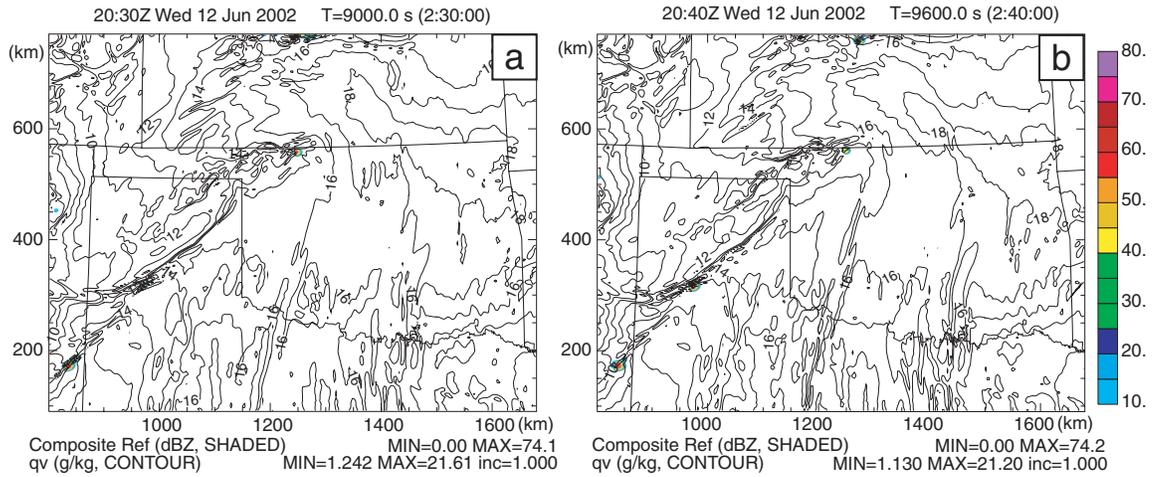
Fig. 6.9 Same as in Fig. 6.5 but from the experiments (a) qvGPS_ANISO at 2030 UTC, (b) qvGPS_UB at 2040 UTC.

the moisture variable, the differences can be attributed to the sensitivity of CI to the initial moisture state. To explain how these differences are produced, we plot in Fig. 6.11 the surface wind divergence and specific humidity within a zoomed-in domain centered at CI4 as marked by the thick black square in Fig. 6.1 and Fig. 6.2. The cloud water is also overlaid. It is shown in Fig. 6.11 that the wind convergence fields look the same among these four panels. The temperature fields are also almost identical (not shown). The specific humidity contours of 14.5, 14, 13.5, 13.5 g kg^{-1} are highlighted respectively in panels (a), (b), (c) and (d). It can be seen that the air is 1 g kg^{-1} more moist in qvGPS_ANISO (Fig. 6.11a) than in the 'truth' at the initiation location while the air at the same location is 0.5 g kg^{-1} more moist in qvGPS_UB (Fig. 6.11b). The more moist environment leads to lower LCL and LFC so it is easier for the air parcels in the cases of panels (a) and (b) to reach their LFC.
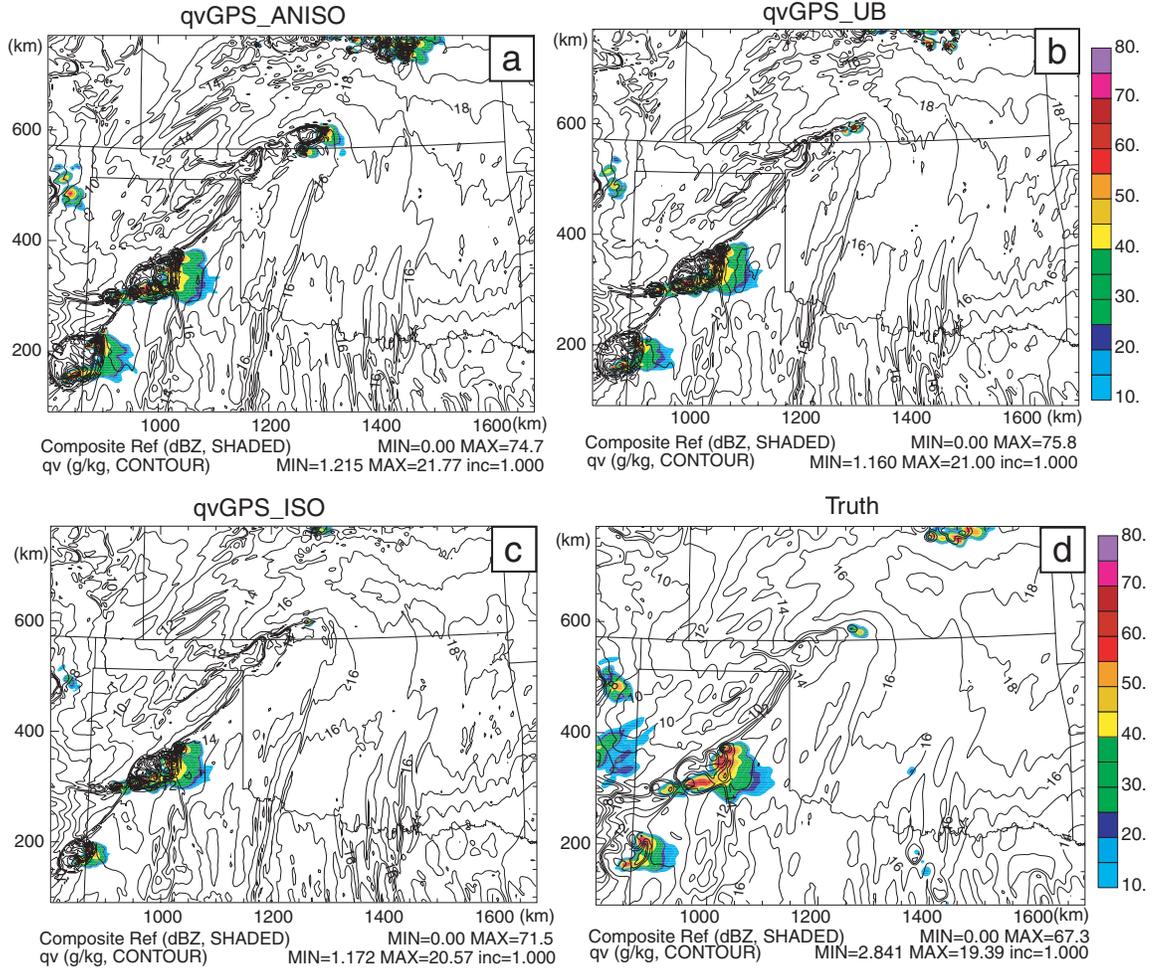
Fig. 6.10 The composite reflectivity and specific humidity at the surface from the experiments (a) qvGPS_ANISO, (b) qvGPS_UB, (c) qvGPS_ISO and (d) the 'truth' at 2150 UTC.

Fig. 6.11c shows that ISO has moisture values similar to those of 'truth' at the initiation location even though experiments ANISO and UB are supposed to provide more accurate moisture analyses than ISO. To understand this discrepancy, we plot the moisture field in the same zoomed-in domain at the analysis time 1800 UTC (Fig. 6.12). We find that the analyses of ANISO and UB are truly better than that of ISO overall. The 14 and 15 g kg^{-1} isohumes highlighted in Fig. 6.12 from ANISO (Fig. 6.12a) and UB (Fig. 6.12b) match those highlighted in the 'truth' (Fig. 6.12d) much better than

those in ISO (Fig. 6.12c). The problem is that some of the very fine-scale moisture variations in the 'truth' cannot be accurately analyzed, due to the still relative coarse data resolution compared to that of the truth grid. In the analysis, along the dryline there
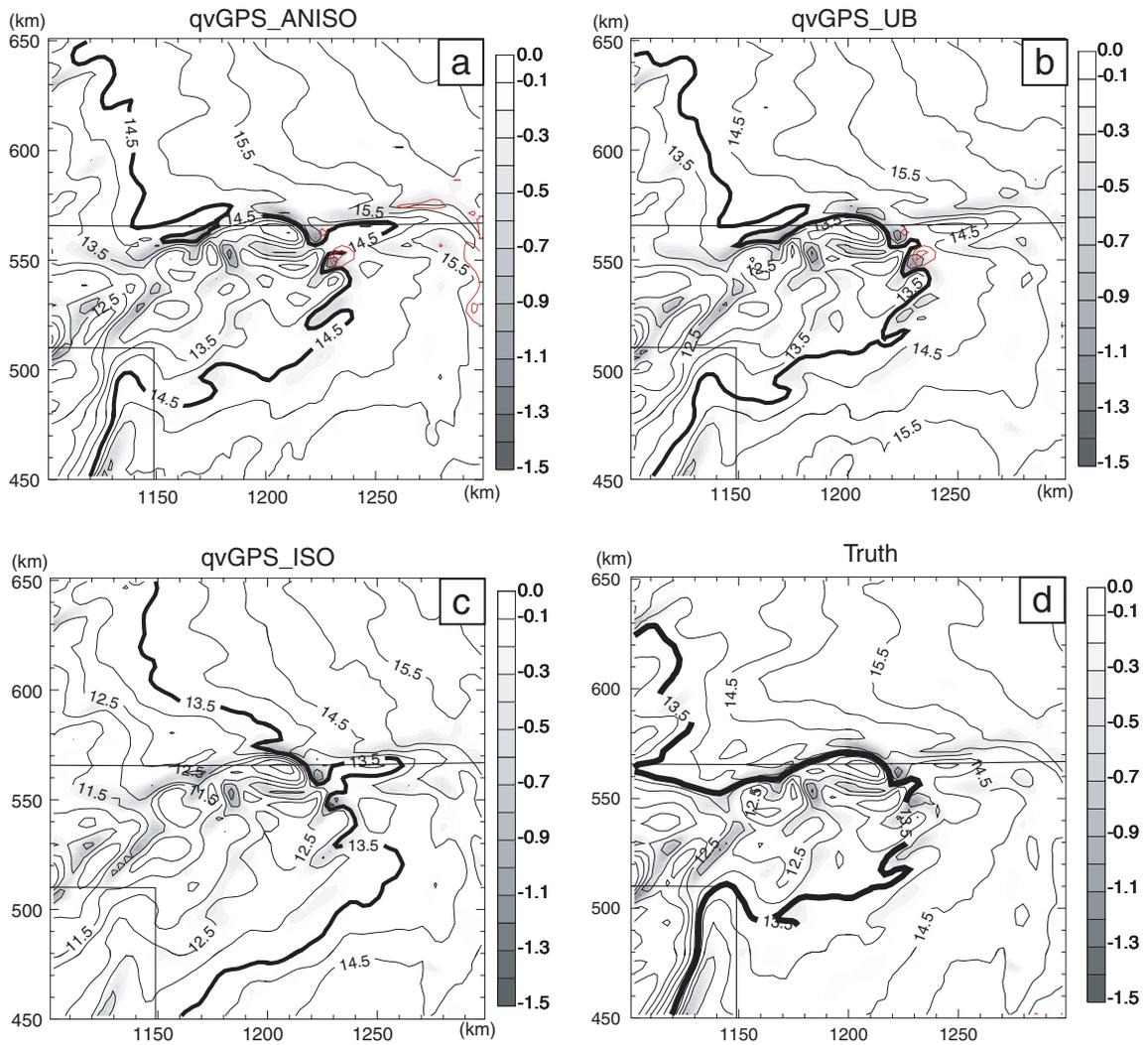
Fig. 6.11 The wind divergence (gray shaded) and specific humidity (contour in g kg^{-1}) at 1950 UTC at the surface within the zoomed-in region marked by square in Fig. 6.1 and Fig. 6.2. The red contours are the total water with 0.1 g kg^{-1} interval. (a) is from qvGPS_ANISO, (b) from qvGPS_UB, (c) from qvGPS_ISO and (d) from the 'truth'.
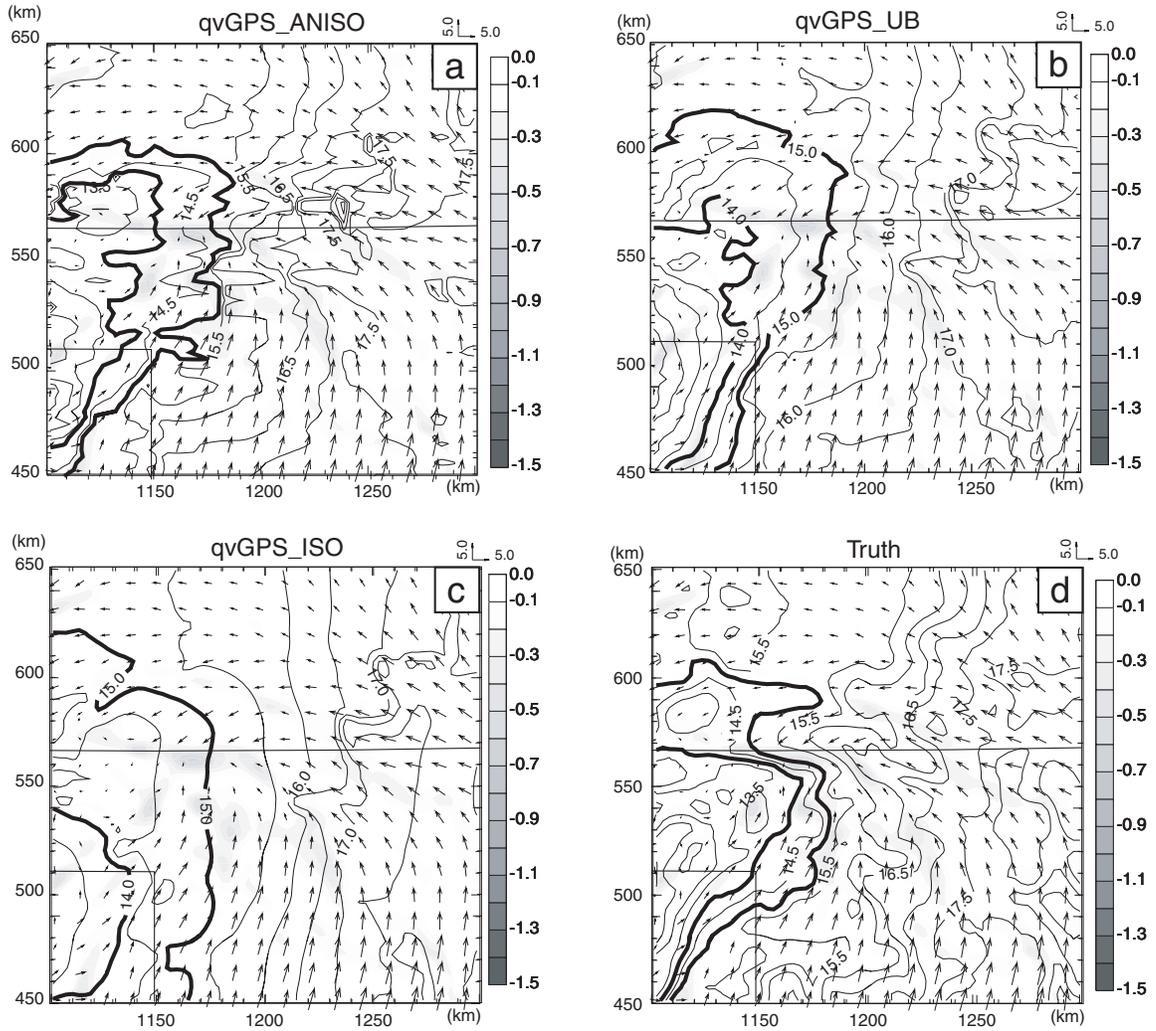
Fig. 6.12 The wind divergence (gray shaded) specific humidity (contour in g kg^{-1}) and wind vector (m s^{-1}) at 1800 UTC at the surface within the same domain as Fig. 6.11. (a) is from qvGPS_ANISO, (b) from qvGPS_UB, (c) from qvGPS_ISO and (d) from the 'truth'.

is no dry tongue to the south of the maximum wind convergence or moist tongue to the north of the convergence but both structures are found in the 'truth' (Fig. 6.12d). In the 'truth', the specific humidity contour of 14 g kg^{-1} extends more eastward than in either ANISO or UB. This more eastward extension results from the southwesterly winds blowing to the west of dryline. Similarly, the contour 15 of g kg^{-1} in the 'truth' extends

159

westward due to the southeasterly winds blowing to the east of dryline. In addition, there is a dry center right east of the Oklahoma panhandle. Thus, the southwesterly winds west of the dryline advect the drier air in 'truth' than in ANISO or UB. After almost 2 hours into the forecast, the environment near the convection initiation location becomes more moist as seen in Fig. 6.11. However, the ISO analysis is generally drier everywhere in the plotting domain, so the CI in the forecast of qvGPS_ISO is late.

Even though the direct reason that leads to the earlier CI is now understood, unfortunately, such fine-scale structures that are on the scale of about 10 km and that gradually create a more moist environment near the CI location, cannot be captured by the GPS *SWV* or surface moisture data. Moreover, no routine moisture measurement network exists in this area that can observe structures of such fine scales currently. Given the large sensitivity of convection initiation at CI4 location to the very fine-scale structures in the moisture field, it is generally difficult to predict the timing and location of such initiation with accuracies within 30 minutes and 30 km, respectively, which further points out the desire for higher resolution moisture measurements in the boundary layer. It has been suggested that a better understanding of convection initiation processes may require spatial resolution of 100 m both horizontally and vertically and temporal resolution of less than 10 min (Weckwerth et al. 1999). Very high-density surface GPS receiver networks may provide a partial solution, while recent work deriving low-level moisture from radar refractivity data has shown promises (Fabry 2004; Weckwerth et al. 2005). Because of their dependency on ground target, the refractivity data can, however, only be obtained within a radius of about 50 km of the radar while the spacings between operational WSR-88D radars are much larger.

For the CI2, all forecasts with our 3DVAR analyzed initial moisture fields have similar timing and location and all match the 'truth' well because, as pointed out earlier, this CI is strongly forced by mesoscale systems. Its updraft is strong with about 2.5 m s$^-$^{1} maximum vertical velocities when the first cloud appears. However, the maximum vertical velocity related to CI4 is about 1 m s^{-1} when the first condensation occurs. The air parcels within the CI2 region can reach their LCL irrespective of possible small errors their moisture content.

In addition to the differences in the CI4 timing and location among the forecasts, the quantitative precipitation amounts also differ even though their patterns are rather similar. Fig. 6.13 shows the hourly equitable threat scores (ETS) for composite reflectivity thresholds of 5, 15, 30 and 45 dBZ for the forecasts of qvGPS_ANISO, qvGPS_ISO qvGPS_UB, and qvETA. The method to calculate ETS can be found in Dawson and Xue (2006). This figure illustrates that for each threshold and throughout most of the forecast hours the forecasts with initial moist fields obtained from the 3DVAR analyses using GPS *SWV* and surface moisture data always have significantly higher ETS than the forecast initialized from Eta moisture analysis. Also apparent from this figure is the much higher scores for the forecasts initialized from the 3DVAR analyses using anisotropic background error covariances (qvGPS_ANISO and qvGPS_UB), indicating that the quantitative precipitation forecasts are improved when better moisture analyses are obtained using anisotropic recursive filters.
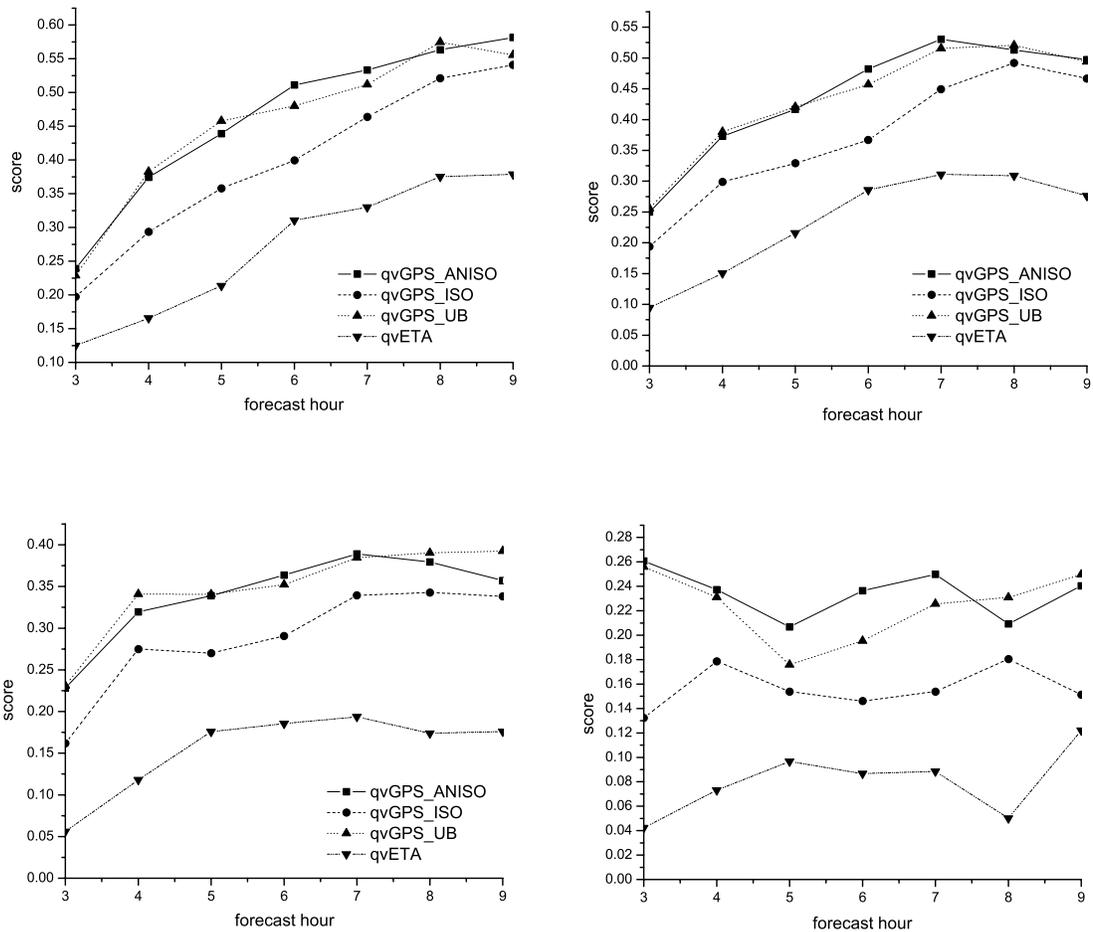
Fig. 6.13 The equitable threat scores for composite reflectivity thresholds of 5 (upper left), 15 (upper right), 30 (lower left) and 45 (lower right) dBZ for the forecasts of qvGPS_ANISO, qvGPS_ISO, qvGPS_UB, and qvETA.

6.4 Summary and discussion

In this chapter, we utilize the 3DVAR system with recursive filters developed in Chapter 4 to retrieve/analyze three-dimensional moisture fields using data from a hypothetical ground-based GPS receiver network and the surface-station moisture data, simulated from a 'truth' simulation obtained in Chapter 5 for the 12 June, 2002 IHOP

dryline convection initiation case. Three 3DVAR analyses are obtained, using, respectively isotropic background error covariance (ISO), anisotropic covariance based on the true error field (ANISO) and anisotropic covariance estimated from an iterative procedure (UB). We then use these analyzed fields to initialize the ARPS model on the 3 km resolution grid, to predict the convection initiation and precipitation for this case. The moisture analysis uses a background moisture field coming from the operational Eta model analysis. All the model variable fields except for the moisture field in the initial condition are kept the same as in the truth. Nine hour forecasts are performed. This design allows us to focus on the impact of the initial moisture field, and the effectiveness of our 3DVAR analysis procedure in capturing the small-scale moist structures in the 3-km truth simulations. The positive impacts of the GPS *SWV* data and the use of anisotropic recursive filters are revealed by verifying the forecasts with the 'truth'. The preliminary conclusions we obtained based on this set of experiments are summarized as follows:

1) The timing and location of convection initiation without strong low-level mesoscale forcing are very sensitive to the moisture initial condition while the initiation with prominent surface forcing is less sensitive to the fine-scale moisture structures because in this case strong surface forcing has the controlling effort.

2) GPS *SWV* data combined with surface moisture data at the receiver stations of a moderate resolution (the resolution is 60 km used in this study) can noticeably improve the analysis of moisture distribution. Most of nearly saturated water vapor in the Eta background is correctly removed in the analysis by the use of *SWV* data. In the forecast with the initial moisture from the analysis background (qvETA),

there is much rainfall near northeastern Oklahoma which strengthens the existing cold pool there, leading to more, stronger and earlier convection initiation. But such a process neither happens in the 'truth' nor in the three forecasts with analyzed moisture initial conditions. The precipitation evolution in these three forecasts is also much more similar to that in the 'truth' than qvETA is.

3) The flow-dependent background error covariance helps improve analysis dramatically as was found in Chapter 4. The precipitation forecast is improved suggested by the higher threat scores of composite reflectivity. The positive impact on the overall moisture analysis, however, did not lead to much positive influence on the CI. It is suggested that the very small-scale moisture structures on the scales of about 10 km has a lot of influence on the exact timing and location of the convection initiation, supported by the study of Xue and Martin (2006a; 2006b), and such structures cannot be accurately analyzed using the assumed receiver network of 60 km resolution. This limitation hindered our ability in achieving significant positive impact on the exact timing and location of convection initiation occurring in regions with weak mesoscale forcing.

In this study, only moisture field is involved in the 3DVAR analysis performed at a single time, so the influence of the GPS and surface moisture data is limited to the initial moisture field alone, i.e., the use of GPS data has no influence on other model variables. The 'truth' wind used in the initial condition for all the forecasts tends to enhance the moisture gradient pretty quickly during the forecast no matter if there is or not a well-defined dryline structure in the initial condition. Therefore, even though the dryline is very weak or missing in the moisture initial condition of the forecast qvETA,

the storm initiation near the intersection point of cold front and dryline is still predicted well. We believe this is the reason that GPS data have little influence on this convection initiation. The realistic situation, however, should be a weak dryline shown in the moisture field would be associated with the weak wind convergence so that the storm initiation related to this dryline would be late.

Chapter 7
Summary and Future Work

7.1 Summary

The results of this dissertation research are summarized in this section. First, in Chapter 3, a three-dimensional variational (3DVAR) analysis scheme is developed in the generalized terrain-following coordinate of ARPS for retrieving the three-dimensional moisture in the atmosphere from slant-path measurements of a hypothetical ground-based Global Positioning System (GPS) receiver network. It is assumed that the observed data are in the form of slant-path water vapor (*SWV*), which is the integrated water vapor along the slant path between the ground receiver and GPS satellite. The inclusion of a background term in the 3DVAR analysis overcomes the under-determinedness problem that would arise using observational data alone. An explicit Gaussian-type spatial filter is first used to model the background error covariances which can be anisotropic. Another addition compared to similar past work is the inclusion of a non-negative-water weak constraint in the cost function that acts to reduce the occurrence of negative water vapor in the upper troposphere.

A set of experiments is conducted to test our 3DVAR scheme using simulated data for a dryline case that occurred on 19, June during the 2002 International H_2O Project (IHOP_2002) field experiment. Results illustrate that this system is robust and can properly recover three-dimensional mesoscale moisture structures from GPS *SWV* data and surface moisture observations. The analysis captures major moisture features

associated with the dryline even when an isotropic spatial filter is used. The analysis is further improved by the use of flow-dependent background error covariances modeled using an anisotropic spatial filter. Sensitivity tests show that surface moisture observations are important for the analysis near the ground, and more so when flow-dependent background error covariances are not used. Vertical filtering is necessary for obtaining accurate analysis increments near the surface. The retrieved moisture field remains reasonably accurate when the observations contain errors of realistic magnitudes. The positive impact of flow-dependent background error covariances increases when the density of ground-based GPS receiver stations decreases.

In Chapter 4, anisotropic recursive filters are implemented within the 3DVAR framework proposed in Chapter 3 to significantly improve the computational efficiency in modeling flow-dependent background error covariance. The general formulation of the background error covariance is the same as used in Chapter 3 and can be based on an estimated error field as an extension to the idea of Riishøjgaard. In the anisotropic case, the background error pattern is constructed by applying at each point six recursive filters along six directions corresponding, in general, to a special configuration of oblique lines of the grid and is stretched or flattened in directions oblique to the alignment of the grid coordinates.

Similar analysis experiments to those in Chapter 3 are conducted to examine the effectiveness of the 3DVAR system with recursive filter in analyzing the GPS *SWV* and the corresponding surface station observations. It is shown that the analyses thus produced are generally comparable to or better than those obtained using corresponding explicit filters. In the case that the background error covariance is isotropic, the

recursive filters perform much better. The reason is believed to be that the recursive filters guarantee the positive definite property of the background error covariance while the truncated explicit Gaussian filters do not.

The impact of flow-dependent background errors modeled using the anisotropic recursive filters is also examined. The use of anisotropic filters improves the analysis. The analysis system is also found to be effective in the presence of typical observational errors. These conclusions are consistent with those of Chapter 3. Additionally, the sensitivity of isotropic and anisotropic recursive-filter analyses to the spatial de-correlation scales of background error covariance is also examined systematically. This examination is facilitated by the much lower computational cost of the recursive filters. Because of their much lower computational cost, they are much more suitable for real time numerical weather analysis implementation.

In Chapter 5, the 12-13 June 2002 convection initiation case from the 2002 International H_2O Project (IHOP_2002) field experiment over the Central Great Plains of the United States is simulated numerically with the Advanced Regional Prediction System (ARPS) at a 3 km horizontal resolution. The case involves a developing mesoscale cyclone, a dryline extending from the low center southwestward with a cold front closely behind which intercepts the middle section of the dryline, and an outflow boundary stretching eastwards from the low center resulting from earlier mesoscale convection. Convection initiation occurred in the afternoon at several locations along and near the dryline or near the outflow boundary but was not captured by the most intensive deployment of observation instruments during the field experiment, which focused instead on the dryline-outflow boundary intersection point.

Standard and special observations collected during the field experiment are assimilated into the ARPS at hourly intervals in a six-hour pre-forecast period in the control experiment. This experiment captured the initiation of 4 groups of convective cells rather well, with timing errors ranging between 10 minutes and 100 minutes and location errors ranging between 5 km and 60 km. The general processes of convection initiation are discussed. Interestingly, a secondary initiation of cells due to the collision between the main outflow boundary and the gust fronts developing out of model-predicted convection earlier is also captured accurately about seven hours into the prediction verified against low level S-pol radar reflectivity. The organization of cells into a squall line after seven hours is reproduced less well.

A set of sensitivity experiments are performed in which the impact of assimilating non-standard data gathered by IHOP_2002, and the length and interval of the data assimilation are examined. Overall, the control experiment that assimilated most data produced the best forecast although some of the other experiments did better in some aspects, including the timing and location of the initiation of some of the cell groups. Possible reasons are suggested. The lateral boundary location is also found to have a significant impact on the initiation and subsequent evolution of convection, by affecting the interior flow response and/or feeding in more accurate observation information through the boundary, as available analyses from a mesoscale operational model were used as the boundary condition. Another experiment examines the impact of the vertical correlation scale in the analysis scheme on the cold pool analysis and the subsequent forecast.

In Chapter 6, using the best simulation obtained in Chapter 5 on the 3 km grid for the 12 June, 2002 case as the 'truth', a hypothetical ground-based GPS receiver network is set up to simulate the *SWV* and surface station data. The 3DVAR system with spatial recursive filters developed in Chapter 4 is utilized to analyze the three-dimensional water vapor field. Three analysis experiments are conducted using, respectively, the isotropic background error covariance, and the anisotropic covariances based on the true background error field or estimated from an iterative procedure. The three analyzed moisture fields are then used to initialize ARPS model on the 3 km grid to predict the convection initiation and precipitation for this case. Meanwhile the moisture analysis background, generated by interpolating the operational Eta analysis, is also used as the initial condition for one of the forecasts. The analysis results are compared to the background and verified against the 'truth' while the forecasts are compared to the 'truth'. Preliminary results demonstrate that the use of the *SWV* data together with the surface station moisture data improves the moisture analysis and hence improves the storm initiation prediction in terms of the timing and location compared to the 'truth'. The use of an anisotropic background error covariance leads to better quantitative precipitation forecast as indicated by the higher equitable threat scores for the calculated composite reflectivity. It does not improve the exact timing and location of the CI that occurred in the northwestern Oklahoma east of the dryline and south of the outflow boundary where significant mesoscale forcing was absent, compared to those when the model is initialized with the moisture field using an isotropic background error covariance. The reason is the prediction of the exact timing and location of CI with weak mesoscale forcing is highly sensitive to the very fine-scale

structures in the low level moisture field, the structures that are of about 10 km horizontal scales which can not be accurately derived from our GPS receiver network with the assumed 60 km resolution.

7.2 Future work

Subsequent work can be done is to further improve the forecasts of the 12 June, 2002 case. The main problem with the current 3 km CNTL forecast of the June 12, 2002 case is that the MCS outflow in the eastern part of OK and KS is not represented well during the forecast. This portion of the outflow is quickly washed out in our forecast. The wind there loses its easterly component quickly so that the wind shear along the outflow boundary is missing within the northeastern OK. The maintenance of this outflow is believed to be responsible for the development of convective cells near northeast OK and for the subsequent organization of the squall line in the region. In the real world, there exists precipitation at the initial time of the forecast which propagated from the northwest of this location. The cool surface air associated with this rainfall has an easterly wind component behind the outflow boundary and plays an important role in slowing down the eastward propagation of the storms that initially formed in southeastern KS. In the CNTL simulation, in the northeastern OK region, a westerly wind component developed instead, which then pushed the system eastward so that the squall line in Fig. 5.6d is located too far east. Further, it is possible that the absence of the easterly component in the MCS outflow region leads to a weaker vertical wind shear there and associated shear vorticity. This effect partly accounts for the poorer evolution of the squall line system in the last 2-hour forecast. Thus, the cloud analysis package

available in the ADAS may be employed to improve the representation of the existing MCS precipitation and the associated cold pool. In addition, we have completed a 1 km simulation of this case, nested inside the 3 km CNTL experiment. This higher resolution simulation provides more realistic details with respect to the convection initiation processes, and detailed analysis are being performed to understand the processes and the results will be reported in a future journal article as a followup to Liu and Xue (Liu and Xue 2007).

Currently, the algorithms we developed in this dissertation using anisotropic recursive filters with flow-dependent background error are being implemented inside the ARPS 3DVAR system (Gao et al. 2003) which simultaneous analyze all model state variables. The next step is for the system to analyze the GPS slant-path total delay which is also the function of temperature and pressure. As a result, the slant-path will also impact the temperature and pressure field. Furthermore, more systematic experiments can be undertaken that can further examine the impact of GPS data when assimilated through intermitted assimilation cycles, as we did with conventional data in Chapter 5. Additional experiments can also be performed to investigate the spatial resolution needed of the receiver network in order to capture the fine-scale moisture structures important for pinpointing the exact timing and location of the convection initiation. Experiments can be performed to examine the effect of irregularly spaced observation station distribution on the analysis. A realistic distribution of ground-based GPS receiver stations can be simulated in these experiments by using the sites based on the current set of stations plus additional sites selected from the current National Weather Service (NWS) surface observation locations. The iterative procedure we

developed for estimating the background error field that is in turn used to model the flow-dependent error covariance for the moisture field can be extended to all analysis variables within the framework of ARPS 3DVAR and the impact of such a generalized procedure on the analysis and forecasting should be assessed. These can be topics for continued OSSE studies that are beyond the scope of this dissertation.

In addition, in the OSSEs performed in Chapter 6, the parameter L_f used in Eq. (4.5), representing the decorrelation scale of the moisture background error, is specified as 3.0 g kg^{-1} in terms of specific humidity. This value was found to work well for the 12 June, 2002 case. Even though the sensitivity experiments in Section 4.5.1 show that the analysis result is not very sensitive to this parameter for the dryline case used in Chapter 4, for cases where the mositure gradident is much weaker, a smaller value may be work better to obtain a good analysis. An examination of the optimal value of L_f and its possible dependency on the weather regime, season and/or geographical region will be a valuable topic in future studies.

The ultimate test on the GPS *SWV* data impact is with the use of real data. During IHOP_2002 (Weckwerth et al. 2004), data from several GPS networks were collected over the Southern Great Plains (SGP). The networks include the continuously operating NOAA/FSL GPS network and the UCAR Suominet (Ware et al. 2000). In addition, 7 special GPS stations were deployed and operated during the period by Centre National de la Recherche Scientifique (CNRS), France and another GPS station was deployed by the Goddard Space Flight Center (GSFC) in the Oklahoma panhandle.
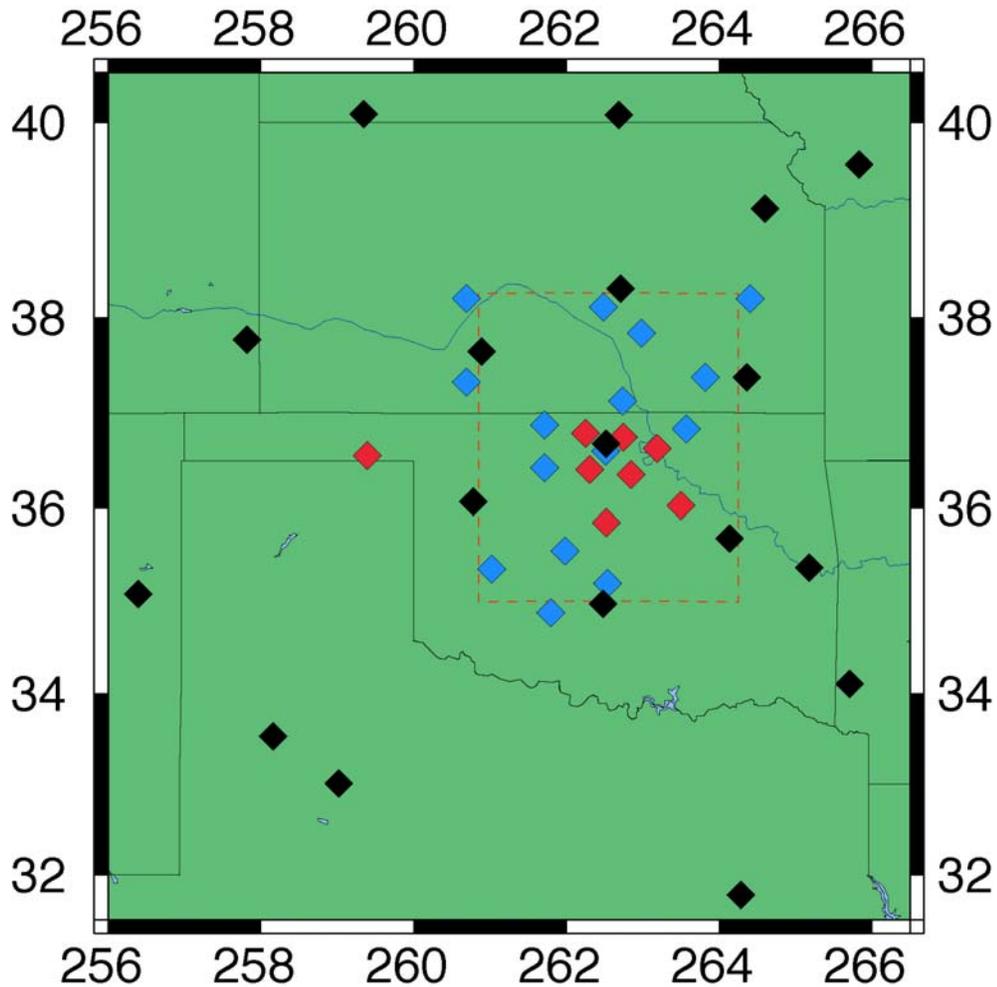
Fig. 7.1 GPS stations in the Southern Great Plains region during the IHOP_2002 experiment (from John Braun's Ph. D dissertation, 2004).

Purdue University operated a mobile GPS from 1 June to 14 June. Thus, there were more than 60 GPS stations in the IHOP domain. A map of most of these stations operating during the field experiment is shown in Fig. 7.1 (Braun 2004). The black diamonds are for the NOAA/FSL stations, the blue diamonds for the Suominet stations and the red diamonds for the additional stations from CNRS and GSFC. *SWV* data from these stations were collected during IHOP_2002. Given the availability of *SWV* observations for the 12 June, 2002 case, real data experiments may be performed to

examine the impact of actual data, at the available resolutions, on the convective storm forecast. Different resolutions and starting times relative to the storm initiation time may be examined to gain a more complete understanding on the impact.

References

Atlas, R., 1997: Atmospheric observations and experiments to assess their usefulness in data assimilation. *J. Meteor. Soc. Japan*, **75,** 111-130.

Bengtsson, L., G. Robinson, R. Anthes, K. Aonashi, A. Dodson, G. Elgered, G. Gendt, R. Gurney, M. Jietai, C. Mitchell, M. Mlaki, A. Rhodin, P. Silvestrin, R. Ware, R. Watson, and W. Wergen, 2003: The use of GPS measurements for water vapor determination. *Bull. Amer. Meteor. Soc.*, **84,** 1249-1258.

Benjamin, S. G. and N. L. Seaman, 1985: A simple scheme for improved objective analysis in curved flow. *Mon. Wea Rev.*, **113,** 1184-1198.

Benjamin, S. G., K. A. Brewster, R. L. Brummer, B. F. Jewett, T. W. Schlatter, T. L. Smith, and P. A. Stamus, 1991: An isentropic three-hourly data assimilation system using ACARS aircraft observations. *Mon. Wea. Rev.*, **119,** 888-906.

Benjamin, S. G., D. Devenyi, S. S. Weygandt, K. J. Brundage, J. M. Brown, G. A. Grell, D. Kim, B. E. Schwartz, T. G. Smirnova, T. L. Smith, and G. S. Manikin, 2004: An hourly assimilation-forecast cycle: The RUC. *Mon. Wea. Rev.*, **132,** 495-518.

Bevis, M., S. Businger, T. A. Herring, C. Rocken, R. A. Anthes, and R. H. Ware, 1992: GPS meteorology: Remote sensing of atmospheric water vapor using the global positioning system. *J. Geophys. Res.*, **97,** 15 787-15 801.

Bevis, M., S. Businger, T. A. Herring, R. A. Anthes, C. Rocken, R. H. Ware, and S. Chiswell, 1994: GPS meteorology: Mapping zenith wet delays onto precipitable water. *J. Appl. Meteor.*, **33,** 379-386.

Bouttier F. and P. Courtier, 1999: Data assimilation concepts and methods. ECMWF
Meteorological Training Course Lecture Series, 58pp.

Bratseth, A. M., 1986: Statistical interpolation by means of successive corrections.
Tellus, **38A,** 439-447.

Braun, J., C. Rocken, and R. Ware, 2001: Validation of line-of-sight water vapor
measurements with GPS. *Radio Sci.*, **36,** 459-472.

Braun, J., 2004: Remote sensing of atmospheric water vapor with the Global
Positioning System, Ph. D. thesis, Department of Aerospace Engineering
Sciences, University of Colorado, 125pp.

Brewster, K., 1996: Application of a Bratseth analysis scheme including Doppler radar
data. *Preprints, 15th Conf. Wea. Anal. Forecasting*, Norfolk, VA, Amer. Meteor.
Soc., 92-95.

Brewster, K., 2002: Recent advances in the diabatic initialization of a non-hydrostatic
numerical model. *Preprints, 15th Conf on Numerical Weather Prediction and
21st Conf on Severe Local Storms*, San Antonio, TX, Amer. Meteor. Soc., J6.3.

Brock, F. V. and S. Fredrickson, 1993: Oklahoma mesonet data quality assurance.
Extended Abstracts. *Eighth Symp. on Meteorological Observations and
Instrumentation*, Anaheim**,** CA.

Brock, F. V., K. C. Crawford, R. L. Elliott, G. W. Cuperus, S. J. Stadler, H. L. Johnson,
and M.D. Eilts, 1995: The Oklahoma mesonet: A technical overview. *J. Atmos.
Oceanic Tech.*, **12,** 5-19.

Buehner, M., 2005: Ensemble-derived stationary and flow-dependent background-error covariances: Evaluation in a quasi-operational NWP setting. *Quart. J. Roy. Meteor. Soc.*, **131,** 1013-1043.

Businger, S., S. R. Chiswell, M. Bevis, J. Duan, R. A. Anthes, C. Rocken, R. H. Ware, M. Exner, T. VanHove, and F. S. Solheim, 1996: The promise of GPS in atmospheric monitoring. *Bull. Amer. Meteor. Soc.*, **77,** 5-18.

Chou, M.-D., 1990: Parameterization for the absorption of solar radiation by O_2 and CO_2 with application to climate studies. *J. Climate*, **3,** 209-217.

Chou, M.-D., 1992: A solar radiation model for use in climate studies. *J. Atmos. Sci.*, **49,** 762-772.

Chou, M.-D. and M. J. Suarez, 1994: An efficient thermal infrared radiation parameterization for use in general circulation models. NASA Tech. Memo. 104606, 85 pp.

Courtier, P., J.-N. Thépaut, and A. Hollingsworth, 1994: A strategy for operational implementation of 4D-Var, using an incremental approach. *Quart. J. Roy. Meteor. Soc.*, **120,** 1367-1387.

Courtier, P., 1997: Variational methods. *J. Meteor. Soc. Japan*, **75,** 211-218.

Crook, N. A., 1996: Sensitivity of moist convection forced by boundary layer processes to low-level thermodynamic fields. *Mon. Wea. Rev.*, **124,** 1767-1785.

Cucurull, L., F. Vandenberghe, D. Barker, E. Vilaclara, and A. Rius, 2004: Three-dimensional variational data assimilation of ground-based GPS ZTD and meteorological observations during the 14 December 2001 storm event over the western Mediterranean Sea. *Mon. Wea. Rev.*, **132,** 749-763.

Daley, R., 1991: *Atmospheric Data Analysis*. Cambridge University Press, 457 pp.

Dantzig, G. B., 1963: *Linear Programming and Extensions*. Princeton University Press, 648 pp.

Davis, J. L., T. A. Herring, I. I. Shapiro, A. E. Rogers, and G. Elgered, 1985: Geodesy by radio interferometry: Effects of atmospheric modeling errors on estimates of baseline length. *Radio Sci.*, **20,** 1593-1607.

De Pondeca, M. S. F. V. and X. Zou, 2001a: Moisture retrievals from simulated zenith delay "observations" and their impact on short-range precipitation forecasts. *Tellus*, **53A,** 192-214.

De Pondeca, M. S. F. V. and X. Zou, 2001b: A case study of the variational assimilation of GPS zenith delay observations into a mesoscale model. *J. Appl. Meteor.*, **40,** 1559-1576.

Duan, J., M. Bevis, P. Fang, Y. Bock, S. Chiswell, S. Businger, C. Rocken, F. Solheim, T. van Hove, R. Ware, S. McClusky, T. A. Herring, and R. W. King, 1996: GPS meteorology: direct estimation of the absolute value of precipitable water. *J. Appl. Meteor.*, **35,** 830-838.

Duchon, C. E., 1979: Lanczos filtering in one and two dimensions. *J. Appl. Meteor.*, **18,** 1016-1022.

Emanuel, K., D. Raymond, A. Betts, L. Bosart, C. Bretherton, K. Droegemeier, B. Farrell, J. M. Fritsch, R. Houze, M. LeMone, D. Lilly, R. Rotunno, M. Shapiro, R. Smith, and T. A, 1995: Report of the first prospectus development team of the U.S. weather research program to NOAA and the NSF. *Bull. Amer. Meteor. Soc.*, **76,** 1194-1208.

Evensen, G., 1994: Sequential data assimilation with a nonlinear quasi-geostrophic model using Monte Carlo methods to forecast error statistics. *J. Geophys. Res.*, **99(C5),** 10 143-10 162.

Fabry, F., 2006: The spatial variation of moisture in the boundary layer and its effect on convection initiation: Project-long characterization. *Mon. Wea. Rev.*, **134,** 79-91.

Falvey, M. and J. Beavan, 2002: The impact of GPS precipitable water assimilation on mesoscale model retrievals of orographic rainfall during SALPEX'96. *Mon. Wea. Rev.*, **130,** 2874-2888.

Fritsch, J. M. and R. E. Carbone, 2004: Improving quantitative precipitation forecasts in the warm season: A USWRP research and development strategy. *Bull. Amer. Meteor. Soc.*, **85,** 955-965.

Gao, J.-D., M. Xue, K. Brewster, and K. K. Droegemeier, 2003: A 3DVAR method for Doppler radar wind assimilation with recursive filter. *31st Conf. Radar Meteor.*, Seatle, WA, Amer. Meteor. Soc.

Gao, J., M. Xue, K. Brewster, and K. K. Droegemeier, 2004: A three-dimensional variational data analysis method with recursive filter for Doppler radars. *J. Atmos. Oceanic Technol.*, **21,** 457-469.

Gaspari, G. and S. E. Cohn, 1999: Construction of correlation functions in two and three dimensions. *Quart. J. Roy. Meteor. Soc.*, **125,** 723-757.

Guo, Y.-R., Y.-H. Kuo, J. Dudhia, D. Parsons, and C. Rocken, 2000: Four-dimensional variational data assimilation of heterogeneous mesoscale observations for a strong convective case. *Mon. Wea. Rev.*, **128,** 619-643.

Ha, S.-Y., Y.-H. Kuo, Y.-R. Guo, and G.-H. Lim, 2003: Variational assimilation of
slant-path wet delay measurements from a hypothetical ground-based GPS
network. Part I: Comparison with precipitable water assimilation. *Mon. Wea.
Rev.*, **131,** 2635-2655.

Harris, B. A. and G. Kelly, 2001: A satellite radiance-bias correction scheme for data
assimilation. *Quart. J. Roy. Meteor. Soc.*, **127,** 1453-1468.

Hayden, C. M. and J. Purser, 1995: Recursive filter objective analysis of meteorological
fields: Applications to NESDIS operational processing. *J. Appl. Meteor.*, **34,** 3-
15.

Hollingsworth, A. and P. Lonnberg, 1986: The statistical structure of short-range
forecast errors as determined from radiosonde data. Part I: The wind field. *Tellus*,
38A, 111-136.

Horn, R. A. and C. R. Johnson, 1985: *Matrix Analysis*. Cambridge University Press,
561 pp.

Hu, M., M. Xue, J. Gao, and K. Brewster, 2006: 3DVAR and cloud analysis with WSR-
88D level-II data for the prediction of Fort Worth tornadic thunderstorms. Part II:
Impact of radial velocity analysis via 3DVAR. *Mon. Wea. Rev.*, **134,** 699-721.

Hu, M. and M. Xue, 2007: Impact of configurations of rapid intermittent assimilation of
WSR-88D radar data for the 8 May 2003 Oklahoma City tornadic thunderstorm
case. *Mon. Wea. Rev.*, **135,** 507–525.

Huang, X.-Y., 2000: Variational analysis using spatial filters. *Mon. Wea. Rev.*, **128,**
2588-2600.

Ide, K., P. Courtier, M. Ghil, and A. Lorenc, 1997: Unified notation for data
assimilation: Operational, sequential and variational. *J. Meteor. Soc. Japan*, **75,**
181-189.

Kalnay, E., 2002: *Atmospheric Modeling, Data Assimilation, and Predictability*.
Cambridge University Press, 341 pp.

Koch, S. E., A. Aksakal, and J. T. McQueen, 1997: The influence of mesoscale
humidity and evapotranspiration fields on a model forecast of a cold-frontal
squall line. *Mon. Wea. Rev.*, **125,** 384-409.

Kuo, Y.-H., Y.-R. Guo, and E. R. Westerwater, 1993: Assimilation of precipitable water
measurements into a mesoscale numerical model. *Mon. Wea. Rev.*, **121,** 1215-
1238.

Kuo, Y.-H., X. Zou, and Y. R. Guo, 1996: Variational assimilation of precipitable water
using a nonhydrostatic mesoscale adjoint model. Part I: Moisture retrieval and
sensitivity experiments. *Mon. Wea. Rev.*, **124,** 122-147.

Lee, B. D., R. D. Farley, and M. R. Hjelmfelt, 1991: A numerical case study of
convection initiation along colliding convergence boundaries in northeast
Colorado. *J. Atmos. Sci.*, **48,** 2350-2366.

Lewis, J. M., S. Lakshmivarahan, and S. Dhall, 2006: *Dynamic Data Assimilation: A
Least Squares Approach*. Cambridge university press, 654 pp.

Lin, Y.-L., R. D. Farley, and H. D. Orville, 1983: Bulk parameterization of the snow
field in a cloud model. *J. Climate Appl. Meteor.*, **22,** 1065-1092.

Liu, H. and M. Xue, 2006: Retrieval of moisture from slant-path water vapor
observations of a hypothetical GPS network using a three-dimensional

variational scheme with anisotropic background error. *Mon. Wea. Rev.*, **134,** 933–949.

Liu, H., M. Xue, R. J. Purser, and D. F. Parrish, 2007: Retrieval of moisture from GPS slant-path water vapor observations using 3DVAR with anisotropic recursive filters. *Mon. Wea. Rev.*, **135,** 1506-1521.

Liu, H. and M. Xue, 2007: Prediction of convection initiation and storm evolution on 12 June 2002 during IHOP_2002. Part I: Control simulation and sensitivity experiments. *Mon. Wea. Rev.*, Conditionally accepted.

Lord, S. J., E. Kalnay, R. Daley, G. D. Emmitt, and R. Atlas, 1997: Using OSSEs in the design of the future generation of integrated observing systems. *Preprint volume, 1st Symposium on Integrated Observation Systems*, Long Beach, CA, Amer. Meteor. Soc., 45-47.

Lorenc, A. C., 1981: A global three-dimensional multivariate statistical interpolation scheme. *Mon. Wea. Rev.*, **109,** 701-721.

Lorenc, A. C., 1992: Iterative analysis using covariance functions and filters. *Quart. J. Roy. Met. Soc.*, **118,** 569-591.

MacDonald, A. E., Y. Xie, and R. H. Ware, 2002: Diagnosis of three-dimensional water vapor using a GPS network. *Mon. Wea. Rev.*, **130,** 386-397.

Markowski, P., C. Hannon, and E. Rasmussen, 2006: Observations of convection initiation "failure" from the 12 June 2002 IHOP deployment. *Mon. Wea. Rev.*, **134,** 375-405.

Niell, A. E., 1996: Global mapping functions for the atmosphere delay at radio wavelengths. *Journal of Geophysical Research*, **101(B1),** 3227-3246.

Otte, T. L., N. L. Seaman, and D. R. Stauffer, 2001: A heuristic study on the importance of anisotropic error distributions in data assimilation. *Mon. Wea. Rev.*, **129,** 766.

Park, S. K. and K. K. Droegemeier, 1999: Sensitivity analysis of a moist 1D Eulerian cloud model using automatic differentiation. *Mon. Wea. Rev.*, **127,** 2180-2196.

Park, S. K. and K. K. Droegemeier, 2000: Sensitivity analysis of a 3D convective storm: Implications for variational data assimilation and forecast error. *Mon. Wea. Rev.*, **128,** 140-159.

Parrish, D. F. and J. C. Derber, 1992: The National Meteorological Center's spectral statistical-interpolation analysis system. *Mon. Wea. Rev.*, **120,** 1747-1763.

Parrish, D. F., J. C. Derber, J. Purser, W. Wu, and Z. Pu, 1997: The NMC global analysis system: Recent improvements and future plans. *J. Meteor. Soc. Japan*, **75,** 359-365.

Parsons, D. B., M. A. Shapiro, and E. Miller, 2000: The mesoscale structure of a nocturnal dryline and of a frontal-dryline merger. *Mon. Wea. Rev.*, **128,** 3824.

Purser, R. J., W.-S. Wu, D. F. Parrish, and N. M. Roberts, 2003a: Numerical aspects of the application of recursive filters to variational statistical analysis. Part I: Spatially homogeneous and isotropic Gaussian covariances. *Mon. Wea. Rev.*, **131,** 1524-1535.

Purser, R. J., W.-S. Wu, D. F. Parrish, and N. M. Roberts, 2003b: Numerical aspects of the application of recursive filters to variational statistical analysis. Part II: Spatially inhomogeneous and anisotropic general covariances. *Mon. Wea. Rev.*, **131,** 1536-1548.

Purser, R. J., 2005: A geometrical approach to the synthesis of smooth anisotropic

    covariance operators for data assimilation. NOAA/NCEP Office Note 447

    (Available from NCEP, 5200 Auth Road, Camp Springs, MD 20746-4304), 60

    pp.

Riishøjgaard, L. P., 1998: A direct way of specifying flow-dependent background error

    correlations for meteorological analysis systems. *Tellus*, **50A,** 42-57.

Rocken, C., R. H. Ware, T. van Hove, F. Solheim, C. Alber, J. Johnson, M. Bevis, and

    S. Businger, 1993: Sensing atmospheric water vapor with global positioning

    system. *Geophys. Res. Lett.*, **20,** 2631-2634.

Rocken, C., T. V. Hove, J. Johnson, F. Solheim, R. Ware, M. Bevis, S. Chiswell, and S.

    Businger, 1995: GPS/STORM-GPS sensing of atmospheric water vapor for

    meteorology. *J. Atmos. Oceanic Technol.*, **12,** 468-478.

Stano, G., 2003: A case study of convective initiation on 24 may 2002 during the IHOP

    field experiment, M.S. Thesis, School of Meteorology, University of Oklahoma,

    106pp.

Stensrud, D. J. and J. M. Fritsch, 1994: Mesoscale convective systems in weakly forced

    large-scale environment. Part II: Generation of a mesoscale initial condition.

    Mon. Wea. Rev., **122,** 2084-2104.

Stensrud, D. J., G. S. Manikin, E. Rogers, and K. E. Mitchell, 1999: Importance of cold

    pools to NCEP mesoscale Eta model forecasts. *Wea. Forecasting*, **14,** 650-670.

Sun, W.-Y. and C.-Z. Chang, 1986: Diffusion model for a convective layer. Part I:

    Numerical simulation of convective boundary layer. *J. Climate Appl. Meteor.*,

    25, 1445-1453.

Ware, R. H., D. W. Fulker, S. A. Stein, D. N. Anderson, S. K. Avery, R. D. Clark, K. K. Droegemeier, J. P. Kuettner, J. B. Minster, and S. Sorooshian, 2000: SuomiNet: A real-time national GPS network for atmospheric research and education. *Bull. Amer. Meteor. Soc.*, **81,** 677-694.

Warner, T. T., R. A. Peterson, and R. E. Treadon, 1997: A tutorial on lateral boundary conditions as a basic and potentially serious limitation to regional numerical weather prediction. *Bull. Amer. Meteor. Soc.*, **78,** 2599–2617.

Weckwerth, T. M., R. M. Wakimoto, R. M. Hardesty, J. W. Wilson, and R. M. Banta, 1999: NCAR-NOAA lower-tropospheric water vapor workshop. *Bull. Amer. Meteor. Soc.*, **80,** 2339-2357.

Weckwerth, T. M., 2000: The effect of small-scale moisture variability on thunderstorm initiation. *Mon. Wea. Rev.*, **128,** 4017-4030.

Weckwerth, T. M., D. B. Parsons, S. E. Koch, J. A. Moore, M. A. LeMone, B. B. Demoz, C. Flamant, B. Geerts, J. Wang, and W. F. Feltz, 2004: An overview of the International H2O Project (IHOP_2002) and some preliminary highlights. *Bull. Amer. Meteor. Soc.*, **85,** 253-277.

Weckwerth, T. M., H. V. Murphey, C. Flamant, C. R. Pettet, S. Bastin, and R. Wakimoto, 2005: Convection initiation on 12 June 2002 during IHOP_2002. . *11th Conf. Mesoscale Processes*, Albuquerque, NM, Ameri. Meteoro. Soc.

Weckwerth, T. M. and D. B. Parsons, 2006: A review of convection initiation and motivation for IHOP_2002. *Mon. Wea. Rev.*, **134,** 5-22.

Wilson, J. W. and R. D. Roberts, 2006: Summary of convective storm initiation and evolution during IHOP: Observational and modeling perspective. *Mon. Wea. Rev.*, **134,** 23-47.

Wolfe, D. E. and S. I. Gutman, 2000: Developing an operational, surface-based, GPS, water vapor observing system for NOAA: Network design and results. *J. Atmos. Oceanic Technol.*, **17,** 426-440.

Wu, W.-S., R. J. Purser, and D. F. Parrish, 2002: Three-dimensional variational analysis with spatially inhomogeneous covariances. *Mon. Wea. Rev.*, **130,** 2905-2916.

Xue, M., J. Zong, and K. K. Droegemeier, 1996: Parameterization of PBL turbulence in a multi-scale non-hydrostatic model. *Preprint, 11th AMS Conf. Num. Wea. Pred.*, Norfolk, VA, Amer. Metero. Soc., 363-365.

Xue, M., K. K. Droegemeier, and V. Wong, 2000: The Advanced Regional Prediction System (ARPS) - A multiscale nonhydrostatic atmospheric simulation and prediction tool. Part I: Model dynamics and verification. *Meteor. Atmos. Physics*, **75,** 161-193.

Xue, M., K. K. Droegemeier, V. Wong, A. Shapiro, K. Brewster, F. Carr, D. Weber, Y. Liu, and D.-H. Wang, 2001: The Advanced Regional Prediction System (ARPS) - A multiscale nonhydrostatic atmospheric simulation and prediction tool. Part II: Model physics and applications. *Meteor. Atmos. Phy.*, **76,** 143-165.

Xue, M., K. Brewster, D. Weber, K. W. Thomas, F. Kong, and E. Kemp, 2002: Realtime storm-scale forecast support for IHOP 2002 at CAPS. *Preprint, 15th Conf. Num. Wea. Pred. and 19th Conf. Wea. Anal. Forecasting*, San Antonio, TX, Amer. Meteor. Soc., 124-126.

Xue, M., D.-H. Wang, J.-D. Gao, K. Brewster, and K. K. Droegemeier, 2003: The Advanced Regional Prediction System (ARPS), storm-scale numerical weather prediction and data assimilation. *Meteor. Atmos. Physics*, **82,** 139-170.

Xue, M. and W. J. Martin, 2006a: A high-resolution modeling study of the 24 May 2002 case during IHOP. Part I: Numerical simulation and general evolution of the dryline and convection. *Mon. Wea. Rev.*, **134,** 149–171.

Xue, M. and W. J. Martin, 2006b: A high-resolution modeling study of the 24 May 2002 case during IHOP. Part II: Horizontal convective rolls and convective initiation. *Mon. Wea. Rev.*, **134,** 172–191.

Zhang, J., K. Howard, and J. J. Gourley, 2005: Constructing three-dimensional multiple-radar reflectivity mosaics: Examples of convective storms and stratiform rain echoes. *J. Atmos. Oceanic Technol.*, **22,** 30-42.

Ziegler, C. L. and E. N. Rasmussen, 1998: The initiation of moist convection at the dryline: forecasting issues from a case study perspective. *Wea. Forecast.*, **13,** 1106-1131.